Title

THE MECHANICAL PROPERTIES AND MICROSTRUCTURAL RELATIONSHIPS IN IRON-MANGANESE-CHROMIUM ALLOYS

Author

Thompson, L.D.

Publication Date

1977

LBL-6234
c.1

THE MECHANICAL PROPERTIES AND MICROSTRUCTURAL RELATIONSHIPS IN IRON-MANGANESE-CHROMIUM ALLOYS

Larry Dean Thompson
(M. S. thesis)

January 1977

Prepared for the U. S. Energy Research and Development Administration under Contract W-7405-ENG-48

LAWRENCE BERKELEY LABORATORY
UNIVERSITY OF CALIFORNIA • BERKELEY •

Table of Contents

ABSTRACT vii

I. INTRODUCTION 1

II. EXPERIMENTAL PROCEDURE 7

  A. Material Preparation 7

  B. Chemical Analysis 8

  C. Heat Treatment 8

  D. Mechanical Testing 9

    1. Tensile Testing 9

    2. Charpy V-notch Impact Testing 9

    3. Hardness Testing 10

  E. Thermodilatometric Analysis 10

  F. X-Ray Analysis 11

  G. Microscopy 13

    1. Optical Microscopy 13

    2. Scanning Electron Microscopy 14

  H. EDAX Analyses 15

III. EXPERIMENTAL RESULTS 16

  A. Mechanical Properties 16

    1. Tensile Properties 16

    2. Charpy V-notch Impact Properties 22

  B. Microscopy 25

    1. Optical Microscopy 25

    2. Scanning Electron Fractography 29

IV. DISCUSSION 32
  A. Microstructural Evaluation 33
    1. 14Mn Alloys 33
    2. 16Mn Alloys 35
    3. 18Mn Alloys 37
    4. 20Mn Alloys 38
  B. Sigma Phase 39
  C. Mechanical Property Evaluation 41
    1. 14Mn Alloys 43
    2. 16Mn Alloys 44
    3. 18Mn Alloys 46
    4. 20Mn Alloys 49
  D. Fracture Properties 51
    1. 14Mn Alloys 52
    2. 16Mn Alloys 53
    3. 18Mn Alloys 54
    4. 20Mn Alloys 55
  E. Effects of Manganese 56
  F. Effects of Chromium 59
  G. Effects of Temperature 61
  H. Corrosion Behavior 62
V. CONCLUSIONS 64
APPENDIX 65
REFERENCES 68
ACKNOWLEDGEMENTS 72
TABLES 73

FIGURE CAPTIONS 82

FIGURES 90

THE MECHANICAL PROPERTIES AND MICROSTRUCTURAL RELATIONSHIPS IN IRON-MANGANESE-CHROMIUM ALLOYS

Larry Dean Thompson

Materials and Molecular Research Division, Lawrence Berkeley Laboratory
and Department of Materials Science and Engineering,
University of California, Berkeley, California 94720

ABSTRACT

The relationships between microstructure and mechanical properties have been studied for a series of Fe-Mn-Cr alloys. A combination of optical and scanning electron microscopy, EDAX analysis, and X-ray diffractometry was used to characterize the microstructures. Tensile testing and Charpy V-notch impact testing were utilized to study the mechanical properties.

Triplex structures of gamma (fcc), alpha (bcc), and epsilon (hcp) were obtained in air-cool and quench-and-refrigeration heat treatments. Increasing volume fractions of metastable austenite and epsilon-martensite phases, which transform during testing, were found to have beneficial effects on the toughness and ductility properties; without significant losses in strength properties. A chromium concentration of 13% led to a better combination of strength and ductility than a concentration of 18%.

The mechanical properties and preliminary corrosion results for the air-cooled 18Mn-13Cr and 16Mn-13Cr alloys are comparable to those of AISI 300 series austenitic stainless steels. These alloys show promise,

therefore, as base systems for replacement austenitic stainless alloys. In addition, the 18Mn-13Cr air-cooled alloy exhibits excellent cryogenic properties, i.e., a yield strength of 360 MPa (53 ksi), an ultimate strength of 1110 MPa (161 ksi), an elongation of 60%, and a reduction in area of 71% at -196°C.

I. INTRODUCTION

The natural resource base has become increasingly important on both an economical and a political level. A great deal of research has been directed toward the more intelligent utilization of materials resources through conservation efforts and alloy design. It is possible to modify existing alloys to improve specific mechanical and/or physical properties in addition to designing new alloys either for a specific application or to replace existing alloys. The replacement of many commercial alloys will be more and more a necessity rather than a curiosity in the future and it will be the responsibility of the materials scientists to design alloys which are more suitable to a wide range of applications.

Until recently, alloy design has taken place predominantly via empirically-oriented techniques. Modern day scientific knowledge accompanied by the advent of highly sophisticated research equipment has enabled materials scientists to study the behavior of materials on an extremely fine scale. With these tools the engineer can attain a more complete understanding of the factors controlling the properties of materials, and can predict the behavior of a specific material from first principles.[1] This basic knowledge, when accompanied by the vast amount of empirical information already found in the literature of materials, will aid in the upcoming "materials shortage crunch". A thorough utilization of basic principles of materials science not only reduces research and materials testing costs, but also reduces the time and energy spent upon fruitless endeavors.

A family of steels known as stainless steels was empirically developed decades ago to withstand the corrosive environments often encountered in engineering applications.[2] A subclass of these stainless steels is the austenitic stainless steels, so named because their primary constituent phase is austenite, the face-centered-cubic structure of iron. In general, the austenitic stainless steels contain a large proportion of alloying elements, the principle alloying elements being nickel and chromium. These Fe-Ni-Cr austenitic stainless steels have been very important technologically as a direct results of their versatility.[3] As well as being corrosion resistant, they are weldable, fabricable, and pleasing in appearance.

Although the austenitic stainless steels are very well suited for most applications, one must realize the tremendous technological advantages in designing alloys with similar mechanical properties and corrosion resistance but with different chemical compositions. In addition, there are indeed severe limitations to the applications of austenitic stainless steels when employed under certain conditions.

An example of the materials limitations of austenitic stainless steels is the grain boundary attack experienced in certain chemical environments.[4] This grain boundary attack is a result of the "sensitization reactions" which occur along the grain boundaries. Complex chromium carbides are precipitated at the grain boundaries, which tends to deplete the grain boundary region of chromium, thus enabling corrosive attack along the grain boundaries. An austenitic stainless steel in this condition is said to be "sensitized".[5] Another limitation is the susceptibility of nickel containing alloys to sulfidation reactions. This is a severe limitation upon the viability of austenitic stainless steels for use in coal gasification systems, where quite high sulfur concentrations are usual.[6]

Finally, one must not overlook the political ramifications of nickel, the availability of which has been an important factor in the past. During World War II, investigations were made into the feasibility of replacing nickel either partially or completely with the austenitizing elements, manganese, carbon, and/or nitrogen.[7] It was hoped that the austenitizing effect of the nickel could be attained in such alloys. With the end of the war came a decrease in the interest of further research in this area. It is only recently that a very real materials availability problem has reignited interest in this area.

A great deal of attention at this laboratory has been focused on the development of TRIP steels.[8,9] TRIP is an acronym for TRansformation Induced Plasticity. The incentive in the development of these steels lay in the need for alloys with a combination of strength and ductility (two properties which are typically divergent)[10] beyond those in commercially available alloys. It was found that the experimental TRIP steels could be processed such that yield strengths ranged from 200,000 to 300,000 psi with corresponding elongations of 25 to 40%.[8]

These extraordinary combinations of strength and ductility were found to be a direct result of stress- and strain-induced phase transformations which inherently took place upon deformation. The mechanically induced phase transformation from metastable austenite (fcc) to a more stable martensitic phase (usually bcc or bct) was found to delay necking in a tensile test, thus allowing for greater uniform elongations.[8] The metastable austenite transforms in response to the applied load and/or plastic strains induced by the applied load. Adjacent volumes of austenite then assume the applied load, and transform to martensite. The martensite itself deforms producing additional elongation of the specimen.[9]

It was later shown that the mechanical properties of metastable austenitic alloys were dependent upon the nature of the strain-induced transformations which took place. The martensite formed during plastic straining increases the rate of strain hardening, thereby preventing necking and subsequent failure. The effect of increasing the strain hardening rate in addition to the delayed necking response results in an overall increase of both tensile strength and elongation.[9]

Although very important technologically and academically, the commercial utility of TRIP steels has been severely limited as a result of the complicated thermomechanical processing that is required in their fabrication. The processing involves an austenitization treatment, a warm rolling deformation treatment, and a refrigeration to liquid nitrogen temperature. A more detailed description of this treatment is given by Parker, et al.[8] Other limitations of these steels is their high cost (arising from expensive alloying needs) and their poor welding characteristics, since it is impossible to thermo-mechanically treat the weld in the manner required to duplicate the mechanical properties of the matrix material.

It would be advantageous, therefore, to investigate materials systems in which mechanically-induced phase transformations occur and in which the thermomechanical processing is not required. Such a system is the iron-manganese binary system. The mechanical properties and phase transformation behavior of iron-manganese alloys have been extensively investigated.[12-21] The most recent study of the Fe-Mn binary system was at this laboratory,[20] where manganese concentrations of 16 wt% and 20 wt% (unless otherwise noted, all compositions are in wt%) were found to yield excellent combinations of strength and ductility in addition to promising cryogenic behavior. Figures 1 and 2 illustrate the strength and ductility properties, respectively, as a function of manganese concentration in the Fe-Mn binary alloys.[20]

The transformation characteristics are extremely interesting in the iron-manganese system. Manganese lowers the stacking fault energy of the austenite and at concentrations above 10%, an epsilon (hcp) martensite phase forms.[19] The epsilon phase is metastable and can subsequentially transform to the stable alpha (bcc) phase. This system is "ideal", therefore, because an overlapping of the effects of two mechanically-induced phase transitions is possible. Also, manganese acts as an austenitizing element in a similar manner as does nickel, as shown in Fig. 3. In addition, it has been reported that the hexagonal epsilon martensitic phase is more resistant to hydrogen embrittlement than the bcc and bct martensitic phases.[9]

At this stage it is possible to design a series of experimental alloys utilizing a combination of materials science knowledge and empirically-determined behavior. The development of systems that do not undergo a degradation in properties as a result of sensitization reactions limits the investigation to alloys which do not contain carbon.

It is well known that additions of about 12% chromium are necessary to achieve good corrosion resistance.[2,5,22] Standard "18-8 austenitic stainless steels" contain 18% chromium. To ensure good corrosion resistance and a smaller effect from fluctuations in alloy chemistry, a 13% addition of chromium is often made to stainless alloys.

The base compositions for this study are 14%, 16%, 18%, and 20% manganese. To each variant in manganese concentration, a 13% and 18% addition of chromium was made. These alloys were gettered with 0.10% aluminum and 0.15% titanium to reduce the effects of the interstitial elements, oxygen, nitrogen, and carbon. By forming compounds with the interstitials the aluminum and titanium immobilize the interstitials and their effects are minimal.

The variations in composition affect the stability of the austenite, thus, directly affecting the phase transformations. The controlling of the austenite stability by composition results in a wide variety of useful combinations of engineering properties in these experimental alloys.

II. EXPERIMENTAL PROCEDURE

A. Material Preparation

The experimental alloys for this investigation were prepared from high purity (0.999+) iron, manganese, chromium, titanium, and aluminum. The alloys were melted in magnesia crucibles using a 100 kW Temescal vacuum furnace. The induction melting was performed under a vacuum of 10^{-3} mm Hg, followed by an argon backfill, which was maintained at approximately 0.2 atmospheres.

The alloys were then cast in three-inch-diameter cylindrical copper chill molds and furnace-cooled to room temperature. Twenty-pound ingots were thus obtained.

The ingots were wrapped in a fiberglass matte material (Fiberfax) and homogenized at 1200°C for 24 hours, under an argon atmosphere. Following homogenization, the ingots were furnace-cooled.

The ingots were then reheated to 1200°C, upset and cross-forged to bars, $2\frac{3}{4}$ inches wide by $\frac{5}{8}$ inches thick, and air-cooled to room temperature. The forged bars were cut into 3-inch sections and the desired heat treatments were carried out on these sections.

Material was taken from these heat-treated sections for the preparation of Charpy V-notch and round tensile specimens to determine the transverse mechanical properties. All machining was carried out with the utilization of a liquid cooling medium directed upon the machined surface to prevent overheating of the specimen and subsequent degradation of the machined surface properties.

Alloy designations and chemical compositions are presented in Table I.

B. Chemical Analysis

Chemical analyses were made by Anamet Laboratories, Berkeley, California, by means of atomic absorption spectroscopy. Manganese and chromium concentrations were found to be vary only slightly from the desired composition. Aluminum and titanium levels were found to be very low which leads to the assumption that the aluminum and titanium were tied up in the form of carbides, nitrides, and oxides. This assumption was substantiated by X-ray diffraction in a scanning electron microscope.

C. Heat Treatment

The as-forged ingots were cut into 3-inch sections. These sections were heat-treated by one of the heat treatment schemes listed in Table II.

Heat treatment scheme A involves only an air cool from an annealing temperature of 900°C and is therefore the most feasible heat treatment from a commercial or industrial standpoint. Heat treatment scheme B involves an ice-brine quench (10% salt solution, ≈ -10°C) followed by refrigeration in liquid nitrogen (-196°C). The heat treatments used for the various alloys are given in Table III.

D. Mechanical Testing

1. Tensile Testing

The tensile properties of the experimental alloys were determined using an 11,000 pound capacity Instron Tensile Testing Machine. All tensile testing was performed on round tensile specimens with a 1-inch gage length and a quarter-inch gage diameter (see Fig. 4b), in accordance with ASTM E8-69 tensile testing standards. The tensile properties were determined using an Instron Crosshead speed of 0.1 cm/min corresponding to a strain rate of 0.0394/minute.

Due to the absence of sharp yield points it was necessary to take a 0.2% offset yield strength and it is these values which are reported. The elongations were measured using a traveling microscope along a gage length line drawn on the specimens with layout dye. The strain-hardening exponents were calculated using the true tensile strain at necking. The energies absorbed in tensile testing were measured by relating the areas under the load-extension curves to the corresponding amounts of energy per unit area.

Tensile tests were performed at room temperature, and in many cases, at -78°C (dry ice plus methyl alcohol) and at -196°C (liquid nitrogen). The low temperature tests were carried out utilizing a cryogenic environmental cell. The tensile properties are given in Table IV.

2. Charpy V-notch Impact Testing

The Charpy V-notch impact tests were made on a 223 ft-lb capacity pendulum-type testing machine in accordance with ASTM E-23-72 testing standards. Standard Charpy V-notch impact specimens were used, the specifications of which are given in Fig. 4a.

The impact energies were determined over the range of temperatures from room temperature to liquid nitrogen temperature (23°C → -196°C). Testing temperatures were obtained by the mixture of the liquids given below:

-196°C (liquid nitrogen)
-140°C (liquid nitrogen + isopentane)
-78°C (dry ice + methyl alcohol)
-30°C (dry ice + methyl alcohol)
23°C (room temperature)

The specimens were immersed in the bath at the appropriate temperature prior to testing. Following testing, the broken specimens were cleaned and blown dry with air and placed in dessicators to preserve the quality of the fracture surfaces.

3. Hardness Testing

The hardness testing was performed on a Wilson Rockwell Hardness Tester in accordance with ASTM E-18-67 testing standards. A minimum of five hardness impressions were made on the Charpy V-notch specimens and the averaged results and heat treatments are given in Table III. The Rockwell "C" scale (150 kg major load and a diamond Braile indentor) was used in all cases.

E. Thermodilatometric Analysis

Thermodilatometric tests were made in order to study the thermally-induced phase transformation behavior upon heating and cooling. A cylindrical specimen with specifications given in Fig. 4c, was used in each case. All tests were performed on a Theta Dilatometer.

A platinum-platinum/10% rhodium thermocouple was spot welded to the specimen, and specimen length versus temperature was recorded using an x-y recorder. A heating rate of 6 °C/sec and a cooling rate of 37 °C/sec were used. This cooling rate corresponds to a fast quench and the specimen was cooled by directing a jet of helium gas through it.

The tests were conducted in the temperature range of 1100°C to 23°C (room temperature). The heating was done under vacuum (10^{-5} torr) and the cooling, of course, involved the jet of helium gas.

F. X-Ray Analysis

The quantitative analyses of the volume percentages and types of phases present were determined using a Picker X-Ray Diffractometer. The X-ray beam was produced from a copper source at 40 kV and 14 ma, with a LiF monochromator. The wavelength of the radiation thus produced was the copper Kα wavelength of 1.542 Å. The volume percentages of phases present were estimated by a well-known direct comparison technique,[36] whereby the integrated diffraction intensities of the (200) and (211) alpha peaks, the (220) and (311) gamma peaks, and the (01·2) epsilon peak are compared. In some cases the intensities of the (110) alpha peak, (111) gamma peak, and (11·0) epsilon peak were compared; this was done for some of the post tensile testing specimens where the exposed area was too small to give clean registered intensities for the higher order peaks.

Samples were carefully prepared using the same method used for otpical microscopy (to be given later), omitting the etching step. The samples were scanned between $2\theta = 40°$ and $2\theta = 100°$ at a scanning rate of 2°/minute and a full-range intensity of 100 or 200 counts per second. The X-ray intensities for the specific peaks were obtained by determining the areas under the peaks on the intensity versus scanning degree chart generated by the diffractometer. These areas were determined utilizing a Dietzgen Compensating Optical Reading Polar Planimeter.

The mathematical details are given by Cullity,[36] but the equations used in this investigation are given below:

$$V_\varepsilon = \frac{I_\varepsilon}{I_\varepsilon + \left(\frac{R_\varepsilon}{R_\alpha}\right) I_\alpha + \left(\frac{R_\varepsilon}{R_\gamma}\right) I_\gamma}$$

$$V_\alpha = \frac{I_\alpha}{I_\alpha + \left(\frac{R_\alpha}{R_\varepsilon}\right) I_\varepsilon + \left(\frac{R_\alpha}{R_\gamma}\right) I_\gamma}$$

$$V_\gamma = 1-(V_\alpha + V_\varepsilon)$$

where,

V_ε = volume fraction of epsilon phase

V_α = volume fraction of alpha phase

V_γ = volume fraction of gamma phase

I_ε = integrated diffraction intensity for a specific epsilon peak

I_α = integrated diffraction intensity for a specific alpha peak

I_γ = integrated diffraction intensity for a specific gamma peak and

$$R = \left(\frac{1}{V^2}\right) f^2 P L e^{-2M}.$$

where

V = volume of unit cell

f = structure factor

P = multiplicity

L = Lorentz polarization factor

e^{-2M} = temperature factor

It should be noted that the X-ray results should be used only for a qualitative interpretation of phase stabilities and transformation behavior, as some preferred orientation was observed in some cases. In all cases, cross sections of Charpy bars were examined to determine the phases present prior to tensile testing. Cross sections of broken tensile specimens were examined to determine the phases present after a tensile test at room temperature and liquid nitrogen temperature.

G. Microscopy

1. Optical Microscopy

Optical microscopy specimens were taken from Charpy specimens. Cross-sectioned faces of Charpy bars were mounted, polished, electropolished, etched, observed, and photographed.

The specimens were mounted in Bakelite mounting resin, which seemed to secure the specimens more tightly than the cold-mounting resin. Specimens were then wet-ground on a 240 grit belt sander and polished on 0, 00, 000, and 0000 polishing sandpapers using kerosene as a lubricant. Between successive papers the specimens were ultrasonically cleaned to ensure that large particles from the previous steps did not remain embedded on the surface.

Following the papers, the specimens were polished using a 1μ alumina polishing paste on a canvas wheel. The specimens were then polished with 0.05μ alumina in an automatic vibrating polishing machine (Syntron) for approximately 10 minutes.

The specimens were then electropolished using a chromic-acetic solution (75 grams chromic trioxide, 400 ml acetic acid, 20 ml distilled water). The electropolishing was performed at 10°C until all surface scratches were removed. At this point polishing on the 1μ wheel was repeated and then electropolishing was repeated. It was found that two or three cycles were necessary to give acceptable results.

The specimens were then etched using a mixed acids-reagent (5 parts nitric acid, 11 parts hydrochloric acid, 11 parts distilled water). Optical photographs were taken at magnifications of 100, 200, 500, 1000, or 1500 X on a Zeiss metallograph, using a cesium-iodide light source and polarized light to improve contrast.

2. Scanning Electron Microscopy

Jelco ISM-U3 and AMR 1000 scanning electron microscopes were used to examine the fracture surfaces of selected Charpy V-notch impact specimens. The instrument was operated at 25 or 20 kV.

Fractographs were taken at magnifications of 200, 300, 1000, and 3000X. 1000X and 200 and/or 300X fractographs were taken for each specimen while a 3000X fractograph was taken only to reveal specific details in particular cases.

H. EDAX Analyses

It was possible to determine the approximate compositions of the phases present in the alloys by using a model 711 EDAX (Energy Dispersive Analysis of X-Rays) X-Ray detector and analyzer and a Nova 2 computer unit. These units were attached to the ASR 1000 scanning electron microscope. By limiting the partial field size and by the use of Frame B computer program for quantitative analysis (developed by the national Bureau of Standards) reasonable approximate compositions were obtained; this computer program contains no "standards", therefore it is important to note that the compositions thus determined could be in error by as much as ± 10%.[23] However, to give an indication of the relative segregation of atomic species to the individual phases, the technique is quite sufficient.

III. EXPERIMENTAL RESULTS

A. Mechanical Properties

1. Tensile Properties

a. 14Mn alloys. Table IV lists the tensile properties of the experimental alloys. The 14Mn alloys were heat treated in accordance with Heat Treatment Scheme B in Table II. Following a quench in ice brine solution, the testing blanks were refrigerated at -196°C for approximately twenty minutes and then allowed to warm to room temperature in air. Tensile properties were evaluated at room temperature, dry ice temperature (-78°C), and liquid nitrogen temperature (-196°C).

In addition to 0.2% offset yield strength, ultimate tensile strength, reduction in area, and elongation data over this range of temperature, strain hardening exponents and the energy absorption during tensile testing were also determined. The strain hardening exponents were calculated from the true strain at the point of necking and gave an indication of the relative uniform elongations as a function of chemical composition and testing conditions. The energy absorbed was calculated from the areas under the load-deflection curves and indicate the relative amounts of energy which were absorbed during the tensile testing. Figures 5-8 show the variation of tensile properties with testing temperature.

Figure 5 shows the variation in yield and ultimate strengths with temperature. While there is only a slight difference in behavior of the yield strengths between the 13Cr and 18Cr alloys, i.e., a gradual increase in yield strength with decreasing temperature, there is a marked difference in the behavior of the ultimate tensile strengths. From an initial UTS/YS ratio of 2.19 at room temperature, the 13Cr alloy showed a ratio of 2.59 at -196°C. The ratios for the 18Cr alloy were 1.87 and 1.60, respectively.

The temperature dependence of the reduction in area and elongation are given in Fig. 6. Again, noteworthy is the relative behavior of the 13Cr and 18Cr alloys. Only mild variations with temperature were found for the 13Cr alloy, while a rapid loss of ductility was found for the 18Cr alloy below -78°C.

Figure 7 gives the strain hardening exponent as a function of temperature. For the 13Cr alloy a maximum n was found at -78°C, corresponding to a true strain at necking of 18%. For the 18Cr alloy, little change was found for the strain hardening exponent from the room temperature value of 0.130 until the temperature was lowered beyond -78°C, where again a rapid decrease in uniform elongation was observed.

Figure 8 is a graph of the energy absorbed in tensile testing versus temperature. The 13Cr alloy absorbed 292 joules (215 ft-lb) of energy at -196°C, as compared to 141 joules (104 ft-lb) at room temperature. The 18Cr alloys absorbed much less energy, 115 joules (85 ft-lb) at room temperature and 24 joules (18 ft-lb) at -196°C.

b. 16Mn alloys. The 16Mn alloys were heat-treated by both heat treatment schemes. The tensile properties were determined as a function of temperature for only the air-cooled treatment. The tensile properties versus temperature for the air-cooled 16Mn alloys are shown in Figs. 9-12.

The strength properties given in Fig. 9 reveal a virtual temperature independence of the yield strengths while the ultimate strengths increased gradually as the temperature is decreased. Initial (UTS/YS) ratios of 2.23 at room temperature, with a ratio of 3.54 at -196°C were observed for the 13Cr alloys. The ratios were 1.69 and 1.84, respectively for the 18Cr alloys. In addition, from Table IV, the air-cooled values of UTS and YS at room temperature are approximately 20% lower than the corresponding values following the quench heat treatment.

Figure 10 shows the temperature dependence of the ductility properties. Noteworthy is the behavior of the 13Cr alloy. There is a decrease of 13% (from 80% to 67%) in the reduction in area while the elongation increases from 43% to 53% over the temperature range of 23°C to -196°C. The 18Cr alloys showed behavior similar to that found in the 14Mn-18Cr alloy, i.e., at temperatures below -78°C, there is a rapid drop in ductility. The room temperature ductility properties (Table IV) are greatly enhanced by air cooling for the 18Cr alloys, while little change was found for the 18Cr alloys.

Figure 11 gives the strain hardening exponent versus temperature for the 16Mn alloys. For the 13Cr alloy, an increase in uniform elongations was found at -196°C compared to those values at room temperature. True strains at necking of 26% were observed at -196°C. Below -78°C, the 18Cr alloy was found to behave characteristically in that a rapid decrease in uniform elongation (and as noted above total elongation) was found with decreasing temperature. Again, the air-cooled treatment (Table IV) proved to enhance uniform elongation in the 13Cr alloy, while only small changes were observed for the 18Cr alloy.

Figure 12 shows the energy absorbed in tensile testing versus temperature for the 16Mn alloys. The increased strain hardening at -196°C again is reflected by a 67% increase in energy absorbed for the 13Cr alloy. The loss of ductility below -78°C is reflected by the behavior of the 18Cr alloy where a rapid decrease in energy absorption accompanies a decrease in temperature. Again, the air-cooled treatment enhanced greatly the room temperature energy absorption capabilities in the 13Cr alloy while little change was found for the 18Cr alloy.

c. <u>18Mn alloys</u>. The tensile data for the 18Mn alloys is presented in Figs. 13-16. The 18Mn-13Cr alloy was heat treated using both the quench and air-cooled heat treatment schemes. The 18Mn-18Cr alloy was heat-treated using the quench and liquid-nitrogen refrigeration heat treatment only. The tensile properties and their variance with temperature were determined in each case.

Figure 13 illustrates the strength properties for the 18Mn alloys. For either the A or B heat treatment schemes, little variation in yield strength was found for the 13Cr alloys, while the yield strength for the 18Cr alloys increased with decreasing temperature. At room temperature, the ultimate-to-yield strength ratios are 2.1 and 1.38 for the 13Cr and 18Cr alloys, respectively. At -196°C, the ratios have changed to 3.76 and 1.50, showing a marked increase in strain hardening in the 13Cr alloys, with decreasing temperature.

Figure 14 gives the ductility properties versus temperature for the 18Mn alloys. The important feature to notice is that for the 13Cr alloy the elongations are 50% or greater from room temperature to -196°C. The reductions in area decrease slightly with decreasing temperature. This is in sharp contrast to the behavior of the 18Cr alloys. Below -78°C, the 18Cr alloys undergo a marked tendency to behave in a more brittle manner as temperature is decreased.

Figure 15 shows the temperature dependence of the strain hardening exponents. For the 18Cr alloys, n decreased rapidly below -78°C to a value of 0.1 at -196°C. The 13Cr alloys, on the other hand, remain ductile at -196°C and the 18Mn-13Cr(A) alloy has an n value of 0.36 at -196°C, corresponding to a true uniform elongation (true strain at necking) of 36%.

The energy absorption during tensile testing is summarized in Fig. 16. The ductile behavior of the 13Cr alloys led to increased energy absorption as temperature was decreased to -196°C. The energy absorption ability of the 18Cr alloy decreased rapidly with decreasing temperature below -78°C. To contrast, alloy 18Mn-13Cr(A) absorbed 366 joules (270 ft-lb) at -196°C, while 18Mn-18Cr(B) absorbed only 77 joules (57 ft-lb) at the same temperature.

d. <u>20Mn alloys</u>. The 20Mn alloys were heat-treated in accordance to both heat treatment schemes. Very important microstructural variations were found to separate the mechanical properties of these alloys markedly from the mechanical properties of the earlier alloys.

The tensile properties of the 20Mn-18Cr(A) or (B) alloys were determined for room temperature only. The alloy behaved in a very brittle manner as seen from the data in Table IV. The technological importance of such a material is greatly decreased by this tendency toward brittle behavior. The specific microstructural features responsible for the embrittlement will be discussed later.

The 20Mn-13Cr alloy was not as severely embrittled and the tensile properties reflect this trend. Figures 17-20 show the temperature dependence of the mechanical properties. From Fig. 17, the yield strength increases with decreasing temperature below -78°C, while the ultimate tensile strength increases gradually with decreasing temperature. This behavior leads to UTS/YS ratios of 1.5 and 2.1 at 23°C and -196°C, respectively.

Figure 18 shows an interesting feature of the ductility properties of the 20Mn-13Cr alloys. Although the reduction in area drops off rapidly with decreasing temperature below -78°C, the elongation remains relatively constant at about 35%. Figure 19 shows that the strain hardening exponent increases with decreasing temperature, i.e., higher uniform elongations were attained at lower temperatures.

Figure 20 summarizes the energy absorption data for the 13Cr alloy. Again, the energy absorbed increases linearly with decreasing temperature at a rate of 0.78 joule/°C. The energy absorbed at lower temperatures almost reaches the values attained for the 18Mn-13Cr alloy (359 joules as compared to 366 joules at -196°C).

2. Charpy V-notch Impact Properties

A summary of the Charpy V-notch impact properties is given in Table V. The Charpy V-notch impact energy versus temperature curves for the experimental alloys are given in Figs. 21 and 22. The Charpy impact energies were determined utilizing five temperatures over the temperature range of -196°C to 23°C. The scatter bands have been omitted in Figs. 21 and 22 to promote clarity in presentation. Typical scatter bands were found to be no greater than 10 ft-lb, and in the cases where greater scatter was observed, additional tests were made to assure an accurate average. Two tests or more were made at each temperature and the results averaged.

The most straightforward way to consider these results will be to methodically treat the alloys in a manner similar to that used for treating the tensile properties. It is important to note that the ductile-brittle transition temperature (DBTT) is defined as that temperature where the energy absorbed is equal to one-half of the value found at room temperature (this corresponds to the upper shelf energy in virtually all cases).

Figure 21 presents the Charpy V-notch impact energy versus testing temperature, for the 14Mn and 16Mn alloys. The 14 Mn alloys were given the B heat treatment. Quite a drastic difference is found between the behavior of the 13Cr and 18Cr alloys, and as will be seen, this trend of behavior is found throughout the remaining alloy compositions. The 14Mn-13Cr(B) curve shows a gradual decrease in impact energy with decreasing temperature from an initial value of 176 joules (130 ft-lb) at room temperature to 75 joules (56 ft-lb) at -196°C. The ductile-brittle transition temperature was found to be -173°C. There was no definite transition in impact behavior; only a gradual decrease in impact energy is found in general for the 13Cr alloys.

In contrast, the curve for the 14Mn-18Cr(B) alloy is completely different in form. From a room temperature impact energy value of 156 joules (115 ft-lb), there is a sharp decrease in energy absorption with decreasing temperature. The DBTT was found to be -15°C with a lower shelf-energy of 5 joules (4 ft-lb). Thus, there is a marked difference in behavior as the temperature is varied, and this behavior will be seen to persist in the 18Cr alloys.

The curves for the 16Mn alloys are also shown in Fig. 21. The 16Mn alloys were heat-treated in accordance to schemes A and B, and the specific impact behavior was dependent upon the heat treatment.

In the air-cooled treatment, the alloys exhibited transition curves which were similar in form to those for the quenched case with impact energies about 40%-50% higher than the corresponding value for the quenched case. No sharp transitions in behavior were found for the 16Mn-13Cr alloys. In the air-cooled treatment, the 16Mn-13Cr alloy exhibited a room temperature impact energy of 190 joules (140 ft-lb). The DBTT was found to be $\approx$ -220°C by extrapolating the experimental curve. This alloy absorbed 115 joules (85 ft-lb) at -196°C. Alloy 16Mn-13Cr(B) was found to have an upper shelf of 119 joules (88 ft-lb) with a DBTT of -148°C, while the energy absorbed at -196°C was 19 joules (14 ft-lb).

For the 16Mn-18Cr alloys the primary difference in heat treatments was in the upper shelf energies, 201 joules (148 ft-lb) for air-cooled versus 146 joules (108 ft-lb) for the quenched treatment. DBTTs for the two cases were -40°C and -56°C, respectively, and the lower shelf energies were quite similar, i.e., 11 joules (8 ft-lb) and 5 joules (4 ft-lb). Material behavior was again very temperature-dependent as in the 14Mn-18Cr case.

For the 16Mn alloys, there is a sharp contrast in behavior of the 13Cr alloys and 18Cr alloys, with the 13Cr alloys less temperature-dependent. However, it is interesting to note that in both cases (A and B heat treatments) the upper shelf energies for the 18Cr alloys is greater than that of the corresponding 13Cr alloys.

Figure 22 gives the transition temperature curves of the 18Mn alloys. The 13Cr alloy was given both heat treatments, while the 18Cr alloy was given only heat treatment B. The similarity in the curves for the 18Mn-13Cr alloys is remarkable and worthy of serious consideration. The upper shelf energies for these alloys was found to be 228 joules (168 ft-lb). The curves were again extrapolated to find the approximate DBTTs since at -196°C the air-cooled and quenched alloys absorbed 165 joules (122 ft-lb), and 152 joules (112 ft-lb), respectively. The DBTTs were found to be -245°C for the air-cooled treatment and -230°C for the quenched treatment. The similarity in the two curves would be expected if the alloys had similar volume percentages of phases initially present, and, as will be discussed later, this was indeed the situation.

The 18Mn-18Cr(B) alloy had an upper shelf energy of 176 joules (130 ft-lb) and a lower shelf energy of 5 joules (4 ft-lb). The DBTT was determined to be -48°C. Again the 18Cr alloy curve was similar in form to that of the 14Mn and 16Mn alloys. The impact properties were, of course, very temperature-dependent.

In consideration of the 20Mn alloys, the effects of an important microstructural variation are readily observed, and will be discussed later. Neither alloy, regardless of heat treatment, revealed any temperature dependence of impact properties. The 20Mn-18Cr alloy absorbed 5 joules (4 ft-lb) over the entire temperature range, thus behaving in a manner that could have been predicted from the tensile properties. Little energy was absorbed in this case indicating that fracture occurred in a very brittle manner. The 20Mn-13Cr alloys absorbed approximately 40 joules (30 ft-lb) regardless of heat treatment, and in this case, this brittle behavior would not have been predicted from the tensile properties.

B. Microscopy

1. Optical Microscopy

Optical microscopy was performed on cross-sections of Charpy V-notch specimens. In most cases high (1000X-1500X) and low (50X-500X) magnification optical micrographs were taken. The higher magnification photographs show more detail and specific features of the microstructure in those cases where pertinent information could be obtained.

a. 14Mn alloys. The optical micrographs of the 14Mn alloys are presented in Fig. 23. The 14Mn alloys were given the ice-brine quench, liquid-nitrogen refrigeration heat treatment. Figures 23a and 23b show the microstructure of the 14Mn-13Cr alloys. At the higher magnification of Fig. 23b, one notes the presence of "stringer"-like transformation products in addition to a generally complicated microstructure.

Figures 23c and 23d show the microstructures of the 14Mn-18Cr alloys. Immediately, one notices the contrast in phase transformation behavior caused by the increase in chromium concentration. The low magnification photograph of Fig. 23c reveals the coarser microstructure associated with the 18Cr alloy.

Figure 23d reveals no "stringer" phases in the 18Cr alloy. This is an interesting observation and will be discussed in more detail later. In general Fig. 23d shows a microstructure which appears to be a matrix phase with other phases and transformation products contained in "islands" which may be seen to lie along specific crystallographic orientations of the matrix.

b. 16Mn alloys. The optical micrographs of the 16Mn alloys are shown in Figs. 24 and 25. The 16Mn alloys were heat treated using both the air-cooled and the quench heat treatments. The microstructures of the 16Mn-13Cr quenched alloy are shown in Figs. 24a and 24b. As one again readily notes, the microstructures are quite complex. The microstructures of the 16Mn-13Cr air-cooled alloy are shown in Figs. 24c and 24d. Contrast conditions were varied between Figs. 24c and 24d, which show that the microstructure of the quenched 16Mn-13Cr alloy is finer than that of the air-cooled alloy. The transformations lead to microstructures that are nevertheless complex in both cases.

The microstructures of the 16Mn-18Cr alloys are shown in Fig. 25. Figure 25a shows the microstructure for the quench heat treatment, while Figs. 25b, 25c, and 25c reveal the microstructure for the air-cooled treatment. In all instances, it is obvious that the morphology is similar to that found for the 14Mn-18Cr alloy (Figs. 23c & 23d). There is a matrix phase with islands of other phases. Figure 25d illustrates the crystallographically-dependent nature of the microstructure. One readily notices changes in orientation across a grain boundary of the matrix phase.

c. 18Mn alloys. The optical micrographs of the 18Mn alloys are shown in Fig. 26. The 18Mn-13Cr alloy was heat-treated by both heat treatment schemes while the 18Mn-18Cr alloy was given only the quench treatment.

Figures 26a and 26b give the microstructures of the 18Mn-13Cr alloy in the as-quenched and air-cooled conditions, respectively. The 18Mn-13Cr quenched alloy appears to have a somewhat less complex microstructure than the air-cooled alloy. Again, transformation products are seen to form on specific habit planes in either case. Figures 26c and 26d reveal the microstructure of the quenched 18Mn-18Cr alloy. While Fig. 26c reveals an area of the microstructure where the microstructural features appear to be quite isotropic, Fig. 26d shows the highly anisotropic features within a single grain and across a grain boundary.

d. 20Mn alloys. The optical micrographs of the 20Mn alloys are shown in Figs. 27 and 28. Both the 13Cr and 18Cr alloys were heat treated utilizing the quenched and air-cooled variations of the heat treatment.

Figures 27a and 27b reveal the microstructures of the 18Mn-13Cr alloy in the quenched and air-cooled conditions, respectively. The striking microstructural feature is the presence of a "dark" stringer-like phase. In reality the stringer-phase has been etched away in these cases. With a lighter etch, the alloy can be prepared to show the stringer phase clearly. Figure 27c shows an example of this light etch preparation, whereby, the presence of the stringer-phase is clearly revealed. In this condition, it is possible to analyze the stringer-phase, utilizing the EDAX attachment to the scanning electron microscope. Figure 27c is an SEM micrograph taken in conjunction with the stringer-phase analysis which will be discussed later.

Figures 28a and 28b reveal the microstructure of the 20Mn-18Cr alloy in the quenched condition while Figs. 28c and 28d show the air-cooled variation of the same alloy. The etching conditions were varied between Figs. 28a and 28c and with a variation in the contrast conditions utilizing polarized light, it was possible to reveal an extremely fine microstructure shown most clearly in Figs. 28c and 28d. Essentially an internetwork of phases on a fine scale, the optical micrographs bring out the important characteristic of the microstructures. A continuous interweaving of phases is responsible for the inherent brittle behavior observed in both the tensile and Charpy V-notch testing.

2. Scanning Electron Fractography

The fracture surfaces of the broken Charpy V-notch impact specimens were examined to determine the microstructural dependence of the fracture behavior. Fracture surfaces of specimens tested at room temperature and at -196°C were examined and changes in impact properties can be assessed on the basis of the resultant nature of the fracture surfaces.

a. 14Mn alloys. The fractographs of the 14Mn alloys are shown in Figs. 29 and 30. Figures 29a and 29b show the fracture surface of the 14Mn-13Cr alloy tested at room temperature. The inherent ductile nature of the fracture is revealed. At -196°C, the fracture surface still revealed a high degree of ductility as shown in Figs. 29c and 29d.

This is contrasted by the behavior of the 14Mn-18Cr alloy which exhibited ductile behavior at room temperature but was brittle at -196°C. Figure 30 shows the fracture surfaces of the 14Mn-18Cr alloy. The ductility at room temperature is clearly shown by the dimpled fracture surface shown in Fig. 30a. Figures 30b, 30c, and 30d show the fractographs of the 14Mn-18Cr alloy tested at -196°C. Smooth cleavage faces and transgranular crack propagation illustrate the general loss of ductility at low temperatures.

b. 16Mn alloys. Figures 31 and 32 show the fracture surfaces of the 16Mn-13Cr alloys and 16Mn-18Cr alloys, respectively. The nature of the fracture surfaces changed very little between the quenched and air-cooled varitions of the alloys, therefore, only the fracture surfaces of the air-cooled alloys are shown.

The fracture surfaces for the 16Mn-13Cr alloy at room and liquid nitrogen temperatures, as illustrated by Fig. 31, are very similar thus revealing the retention of ductile behavior at temperatures as low as -196°C. The fracture surface of the 16Mn-18Cr alloy tested at room temperature is given in Fig. 32a. Again, a typically ductile fracture surface is revealed. At -196°C, the fracture characteristics change to those of a brittle material with cleavage faces running across the fracture surface. This fracture behavior is illustrated in Figs. 32b and 32c.

c. 18Mn alloys. The fracture behavior of the 18Mn-13Cr alloys was not dependent upon heat treatment, so only the air-cooled alloy fractographs are shown in Fig. 33. At room temperature (Fig. 33a), large dimple sizes and a ductile tearing fracture mechanism is clearly shown. Even at -196°C, Fig. 33b reveals a similar fracture mechanism and a very ductile, high energy-absorbing type of fracture surface.

Figure 34a shows the fracture surface of the 18Mn-18Cr alloy tested at room temperature. The ductile nature of the fracture surface is obvious from the dimple rupture characteristics. Figures 34b, 34c, and 34d show the fracture surfaces of this alloy when tested at -196°C. It is quite clear that a transition in fracture behavior has occurred by the prominence of cleavage faces. A loss of ductility at low temperatures, similar to that of the other 18Cr alloys, is characteristic of the 18Mn-18Cr alloy.

d. 20Mn alloys. Figure 35 reveals the fracture characteristics of the quenched and air-cooled variations of the 20Mn-13Cr alloys. The fracture surface characteristics were independent of heat treatment and therefore, only the fractographs of the air-cooled alloy are needed to evaluate the fracture behavior of these alloys. Figures 35a and 35b show the fracture surface of the alloy tested at room temperature. Noteworthy is the presence of "holes" in the fractograph which are characteristic of the fracture along the stringer phase found in these alloys. This behavior is best shown in Figs. 35a and 35c. Despite locally ductile regions of the fracture surface, as shown by Fig. 35b the overall fracture characteristics of this alloy are those of a material containing a partial network of a brittle phase. Figures 35c and 35d correspond to fracture at -196°C, where the ductile areas are not evident. It is interesting that the energy absorption at 23°C and -196°C was unchanged and that the locally ductile fracture at 23°C did not add to the energy-absorption ability of the alloy.

Figures 36a and 36b reveal the fracture surfaces of the 20Mn-18Cr alloy. The very fine brittle fracture surface reveals that crack propagation occurred along the brittle constituent phase network. A fracture surface such as this implies a very low energy absorbing ability which was observed experimentally with these alloys.

IV. DISCUSSION

In an effort to understand the phase transformation behavior in the Fe-Mn-Cr system, thermodilatometric experiments were performed between the temperatures 1100°C and 23°C. A heating rate of 6 °C/sec and a cooling rate of 37 °C/sec were utilized. Table VI gives a list of the observations made on heating an on cooling.

Only phase transformations corresponding to $\gamma \rightarrow \varepsilon$ on cooling and $\varepsilon \rightarrow \gamma$ on heating were observed in this temperature range and at this cooling rate. The $\gamma \rightarrow \varepsilon$ phase transformation was identified by a volume decrease at the transformation start temperature. Schumann[24] has found that the $\gamma \rightarrow \varepsilon$ transformation has a corresponding volume decrease of approximately 2.1% while the $\gamma \rightarrow \alpha$ transformation had a 2.7% volume increase. It was on this basis that the transformation behavior was investigated.

One notes in Table VI that among the 13Cr alloys, increasing manganese concentration depresses the $\gamma \rightarrow \varepsilon$ Ms temperature, while manganese concentration seems to have little effect on the 18Cr alloy behavior. Also of interest is the observation that there were no thermally-induced phase transformations for the 20Mn-18Cr alloy. Another interesting feature is the absence of any $\gamma \rightarrow \alpha$ or $\varepsilon \rightarrow \alpha$ phase transformations in this temperature range. This suggests that the start temperatures for the thermally-induced transformations to the alpha phase lie in the temperature range below room temperature.

Some confusion has been generated in the past over the specific transformation sequence in alloy systems where ε martensite is formed.

Epsilon martensitic phases form in 18/8 austenitic stainless steels as well as in iron-based manganese alloys in which the manganese concentration is higher than 10%. Dash and Otte,[25] and Ooka and Suemune[26] have concluded that the epsilon phase is a transformation product which forms to relieve the transformation strains associated with the γ → α phase transformation. Cina,[27] Dunning,[28] Manganon and Thomas,[29] and Haddick[21] conclude that the epsilon phase is a transition phase and that the sequence of phase transformation behavior is γ → ε → α. Kelly,[30] and Manganon and Thomas[29] have proposed specific phase transformation mechanisms as to how the γ → ε → α phase transformation sequence could be accounted for on an atomic scale. This author will lend evidence to support the γ → ε → α transformation sequence in high manganese iron-based alloys.

The volume percentages of phases present in the "as heat treated" condition are given in Table VII. In addition, the volume percentages of phases present have been determined after tensile testing at room temperature (23°C) and liquid nitrogen temperature (-196°C). These values should be used only to give a qualitative idea of the relative stabilities of the phases and the relative effects of quenching to -196°C in the B heat treatment scheme. It is now possible to evaluate the experimental alloys on the basis of composition.

A. Microstructural Evaluation

1. 14Mn Alloys

The microstructure of the 14Mn-13Cr alloy is shown in Fig. 23b. From Table VII this corresponds to 24%γ, 22%ε, and 54%α. Although with a microstructure as complex as this, it is difficult to distinguish specific constituents by optical microscopy, it is possible to observe some interesting features. One notes that at the position of the "arrow" there is a band of epsilon martensite with alpha martensite contained within. Other bands of epsilon martensite may be noted throughout the microstructure which lie in specific crystallogarphic orientations with respect ot the matrix (gamma) grain. Gordon-Parr[31] has found that the orientation of these epsilon martensite bands with respect to the gamma phase is $(0001)_\varepsilon \parallel (111)_\gamma$. This corresponds to the Nishiyama transformation mechanism and would be expected in this case where the $(0001)_\varepsilon$ planes are close packed, as are the $(111)_\gamma$ planes.

The observations seem to indicate that the transformation sequence is indeed $\gamma \rightarrow \varepsilon \rightarrow \alpha$ in these alloys; however, it must also be pointed out that some ferrite exists prior to the occurrence of any transformation. Kinzel and Franks[32] have reported a number of "constant manganese concentration" Fe-Mn-Cr phase diagrams, which indicate that at 900°C, the alloy is in a two-phase (γ,α) region. The two-phase region exists up to temperatures as high as 1250°C for chromium concentrations of 13% and 18%, i.e., the chromium concentrations that were studied in this investigation.

The microstructure of the 14Mn-18Cr alloy is shown in Fig. 23d. The phase that appears to be the matrix phase was found to be high in chromium and lower in manganese concentration by EDAX analysis. The approximate composition of this phase was found to be 22%Cr, 12%Mn, balance Fe and is assumed to be the ferritic phase. The X-ray analysis results seem to confirm this, since, from Table VII, the microstructure contains approximately 16%γ, 5%ε, and 79%α. The epsilon martensite in this alloy is relatively unstable and transforms to the alpha phase during the liquid nitrogen refrigeration treatment. Islands of the gamma phase are observed containing epsilon martensite and alpha martensite. One notices that the gamma islands have formed along specific orientations within the matrix. Kelly[30] has suggested that the orientation relationship for the γ-α phases is $(111)_\gamma \parallel (101)_\alpha$ and $[1\bar{1}0]_\gamma \parallel [11\bar{1}]_\alpha$ which is the Kurdjumov-Sachs relationship.

2. 16Mn Alloys

The microstructures of the 16Mn-13Cr alloys are shown in Fig. 24. Figures 24a and 24b are the microstructures of the alloy given heat treatment B, while Figs. 24c and 24d refer to the air-cooled alloy. From Table VII, the alloy given heat treatment B has a microstructure consisting of 18%γ, 33%ε, and 49%α. In Figs. 24a and 24b, arrows again point to regions where bands of epsilon martensite have formed with subsequent transformation to alpha martensite. According to Kelly,[30] the crystallographic orientation of these phases are:

$$(111)_\gamma \parallel (0001)_\varepsilon \parallel (101)_\alpha$$

$$[1\bar{1}0]_\gamma \parallel [1\bar{2}10]_\varepsilon \parallel [11\bar{1}]_\alpha$$

It must be remembered that the total alpha phase present is a combination of ferrite and alpha martensite. This is verified by examining the microstructures of the air-cooled alloy.

Figures 24c and 24d show the microstructures of the 16Mn-13Cr air-cooled alloy. From Table VII, the phase composition is 31%γ, 33%ε, and 36%α i.e., an almost perfectly balanced triplex structure of γ, ε, and α.

Larger epsilon martensite bands may be observed. The increase in retained austenite from 18% to 31% by air-cooling verifies indeed that phase transformations occur when the alloy is refrigerated at liquid nitrogen temperature. Also, it should be pointed out that with the increase in manganese concentration from 14% to 16%, an observed increase in epsilon martensite occurs, supposedly because of the further decrease in stacking fault energy and a lowering of the volume free energy of the epsilon phase.

Figure 25 shows the microstructures of the 16Mn-18Cr alloys. Figures 25a and 25b show the microstructure of the quenched alloy. From Table VII the phase composition of this alloy is 21%γ, 33%ε, and 46%α. Similar to the 14Mn case, the matrix phase is ferrite, and the gamma, epsilon martensite, and alpha martensite are contained in the islands within the matrix. Figure 25b shows the crystallographic dependence of the orientation of the gamma islands with respect to the matrix alpha phase. It is evident that across grain boundaries of the alpha, the orientation of the gamma changes, thus accommodating the strains at the interface.

Figures 25c and 25d show the air-cooled 16Mn-18Cr alloy microstructure comprised of 22%γ, 46%ε, 32%α. In this case no alpha martensite has formed. An EDAX analysis was carried out and it was found that the matrix ferritic phase, marked "A", had an approximate composition of 23%Cr, 12%Mn, balance Fe, while the gamma and epsilon martensite phases, marked "B", has a composition of 14%Cr, 16%Mn, balance Fe. Figure 37 shows the EDAX scan thus obtained. The background scan is the alpha phase while the foreground scan is the gamma phase. The peak on the left at E(kV) ≈ 05.3 is the Cr Kα peak; at E(kV) ≈ 05.9 is the Mn K_α; and at E(kV) ≈ 06.3 is the Fe K_α peak. One notes that the chromium concentration of the alpha phase is much grater than that of the gamma phase. No compositional variations were noted between gamma and epsilon martensite since no diffusion of atoms occurs during the epsilon martensite transformation.

Figure 25c also shows evidence of twinning of the austenite. Close inspection reveals the presence of primary twins and secondary twins within austenite grains. Figure 25d shows the orientational changes of the gamma and epsilon phases across an alpha grain boundary.

3. 18Mn Alloys

The microstructures of the 18Mn-13Cr alloy are given in Figs. 26a and 26b. The microstructure of the quenched alloy is shown in Fig. 26a and corresponds to a phase composition of 51%γ, 39%ε, and 10%α. Readily noticeable are large, relatively untransformed, blockly areas of the microstructure. These areas correspond to the retained austenite. At 18Mn-13Cr, structures of the austenite and epsilon are favored despite the refrigeration to -196°C.

Figure 26b shows the microstructure of the air-cooled 18Mn-13Cr alloy. Table VII gives a phase composition of 47%γ, 46%ε, and 7%α. The epsilon martensite has formed in very thin bands, alternating orientations with respect to austenite grain orientations. It will be noted later that the high retained austenite levels present in the 18Mn-13Cr alloys lead to very interesting mechanical properties.

Figures 26c and 26d show the microstructures of the 18Mn-18Cr(B) alloy, where the phase composition is 18%γ, 30%ε, and 52%α. Figure 26c reveals an area of the microstructure where the orientation of the gamma and epsilon seem to be relatively random, while Fig. 26d shows a localized region where definite crystallographic orientations exist. In addition, close inspection again reveals the existence of twins in the austenite grains.

4. 20Mn Alloys

The microstructures of the 20Mn-13Cr alloys are given in Figs. 27a and 27b for the alloy in the quenched and air-cooled state, respectively. The striking feature of the microstructure is the stringer phase which is very prominant at these manganese levels. From Table VII, quenching seems to retain more austenite (37% as compared to 23% for the air cool) and transforms less austenite to epsilon martensite (48% as compared to 60% for the air cool), suggesting that the epsilon martensite transformation may be sluggish at these manganese concentrations. Table VII gives no reference to the stringer phase, because, no X-ray peaks were observed other than those for the gamma, epsilon, and alpha phases. It is quite obvious though that the presence of this phase will affect the mechanical properties and this has been revealed earlier.

The microstructure of the 20Mn-18Cr alloy is shown in Fig. 28. It was in this alloy that several X-ray peaks began to appear which were not present in the other alloys. An EDAX analysis was performed and the two phases marked "A" and "B" were found to have markedly different phase compositions, while no other phase compositional variations could be found. Phase A was found to have an approximate composition of (21%Cr, 18%Mn, balance Fe) while phase B was found to have a composition of (15%Cr, 19%Mn, balance Fe). Figure 38 shows the EDAX scan obtained with the phase A scan as the background and the phase B scan in the foreground. Higher levels of chromium and manganese are revealed in phase A by the increase in intensities of the corresponding chromium and manganese peaks. By visual inspection, the phase composition is approximately 60-70%A and 30-40%B.

Subsequent X-ray analysis was based on the assumption that the high Cr, high Mn phase A was the ordered complex tetragonal sigma phase. From the X-ray scan obtained for the 20Mn-18Cr alloy, the $(103)_\sigma$, $(113)_\sigma$, and $(333)_\sigma$ peaks were identified. These peaks were observed at angles of $2\theta = 61.8°$, $2\theta = 62.8°$, and $2\theta = 77.4°$, respectively. The identification of the sigma phase warrants a discussion on the presence of sigma phase in the the Fe-Mn-Cr system.

B. Sigma Phase

The complex tetragonal sigma phase[32] appears in both the Fe-Cr binary system and the Mn-Cr binary system. In the Fe-Cr system, the sigma phase is approximately 50%Fe-50%Cr, while in the Mn-Cr system, the composition is approximately $CrMn_3$. The conventional unit cell in either case has a c/a ratio of 0.51xx where disagreement is found only in the third and fourth digit to the right of the decimal point, i.e., $c/a = 0.5164$ for σ in Fe-Cr, while $c/a = 0.5181$ for σ in Mn-Cr.

In the X-ray analysis performed for the 20Mn-18Cr alloy an average c/a value was assumed. X-ray peak positions could then be calculated from the assumed c/a ratio.

Repolishing and light etchings were performed on the 14Mn-13Cr, 16Mn-13Cr, 18Mn-13Cr, and 20Mn-13Cr alloys and EDAX analyses were carried out on the "stringer phases" observed earlier.

Figure 39 shows an area of the 14Mn-13Cr microstructure containing the stringer phase (arrow). EDAX analysis showed that the stringer had a composition of 22%Cr, 9%Mn, balance Fe while the matrix material had a composition of 13%Cr, 12%Mn, balance Fe. Figure 40a shows the EDAX scan of the matrix material, while Fig. 40b shows the EDAX scan of the stringer.

Figure 41 shows a stringer in the 16Mn-13Cr alloy. In this case, the stringer was found to have a composition of 22%Cr, 9%Mn, balance Fe while the matrix was found to have a composition of 13%Cr, 13%Mn, balance Fe. The corresponding EDAX scans are shown in Figs. 42a and 42b. Figure 42a is the EDAX scan of the matrix and Fig. 42b is the scan of the stringer.

Figure 43 reveals an area of the microstructure in the 18Mn-13Cr alloy containing a stringer. The EDAX scans are given in Figs. 44a and 44b for the matrix and stringer, respectively. The composition of the stringer was found to be 22%Cr, 14%Mn, balance Fe and the composition of the matrix was 13%Cr, 17%Mn, balance Fe.

Figure 27c shows a stringer in the 20Mn-13Cr alloy. The composition of the stringer was 24%Cr, 13%Mn, balance Fe while the composition of the matrix was 13%Cr, 18%Mn, balance Fe. The corresponding EDAX scans for the matrix and stringer are given in Figs. 45a and 45b, respectively.

In each of these cases the chromium concentration of the matrix in areas near the stringer was found to be below the nominal concentration in the alloy, indicating the segregation of chromium to the stringer phase. The compositions of the stringer phases are listed below:

14Mn-13Cr : 22Cr, 9Mn, balance Fe
16Mn-13Cr : 22Cr, 9Mn, balance Fe
18Mn-13Cr : 22Cr, 14Mn, balance Fe
20Mn-13Cr : 24Cr, 13Mn, balance Fe
20Mn-18Cr : 21Cr, 18Mn, balance Fe

Although it is impossible to assert that the stringer phases are indeed the sigma phase from the data obtained, the compositions variations are not pronounced and it may be assumed that the stringers are indeed sigma phase. As the manganese concentration of the alloy is increased, the manganese concentration in the sigma phase increases. Chromium concentrations remain relatively stable regardless of alloy composition.

Thus the presence of the sigma phase in the Fe-Mn-Cr alloys is most pronounced at high concentrations. Also interesting is the absence of sigma phase in the 14, 16, and 18Mn alloys with 18Cr.

C. Mechanical Property Evaluation

In order to understand the mechanical properties of the Fe-Mn-Cr alloys, it is necessary to consider the phase composition of the alloys and how they relate to the subsequent behavior. The initial phase compositions of the Fe-Mn-Cr alloys may be altered by heat treatment, as was established earlier. However, there are also strain-induced phase transformations that occur when the alloys are subjected to plastic deformation at temperatures below the M_d, the temperature above which plastic deformation does not induce phase transformations.

Mechanically-induced phase transformations are not unusual and have been the basis for many studies,[8,9,24-30] both from an experimental and a theoretical viewpoint. As was stated earlier, the 18/8 type austenitic stainless steels experience strain-induced phase transformations similar to those found in the Fe-Mn-Cr system. The larger reduction in stacking fault energy, as a result of the high manganese concentrations investigated in this study,[20,31] favors the formation of epsilon martensite in a $\gamma \rightarrow \varepsilon \rightarrow \alpha$ transformation sequence.[30]

It is also important to note that in these materials with low stacking fault energies, one must deal with stress- and strain-induced transformations for both metastable phases, i.e., γ and ε. If the temperature of deformation is near the M_s temperature, then a stress-assisted phase transformation will occur prior to plastic deformation.[9] Also, the stabilities of the metastable phases may change with temperature.

Both Mn and Cr have been reported to decrease the austenite stacking fault energies.[30] Therefore, in these experimental alloys, overlapping effects of stacking fault energy contributions from both Mn and Cr will account for changing phase transformation characteristics with composition and temperature of deformation. In addition, the structure may change when the alloy is tested at low temperatures.

The phase compositions of the alloys are given in Table VII in the "as-heat treated" condition and after tensile testing at 23°C and at -196°C. An evaluation of the mechanical properties requires an evaluation of the initial microstructure and a consideration of the stabilities of the metastable austenitic and epsilon martensitic phases. From Table VII, the conclusion may be drawn that the M_d temperatures for all of the experimental alloys (with the exception of the Fe-20Mn-18Cr alloy) are higher than room temperature, since phase transformations occur during room temperature tensile testing.

1. 14Mn Alloys

a. Tensile properties. The tensile properties of the 14Mn alloys are given in Figs. 5-8. The phase compositions are given in Table VII. The 14Mn-13Cr alloy (24%γ, 22%ε, and 54%α) contains 46% (all phase compositions are volume percentages) metastable phases, while the 14Mn-18Cr alloy contains only 21% metastable phases.

After tensile testing, the 14Mn-13Cr alloy is completely transformed to the stable alpha phase, while the 14Mn-18Cr alloy retains a small amount of epsilon martensite. The effect of the increased degree of transformations in the 14Mn-13Cr alloy leads to higher strain hardening rates and greater uniform elongations in this alloy.

This increased ductility leads to higher levels of energy absorption in tensile testing, as well as better overall low temperature properties. The primary phase constituent of the 14Mn-18Cr alloy is the alpha (bcc) phase. At 23°C, this alloy shows moderate degrees of ductility and energy absorption. However, as the temperature is decreased, particularly below -78°C, the ductility drops off rapidly and the alloy behaves as a bcc ferritic alloy. At -196°C all ductility has been lost.

b. Charpy V-notch impact properties. For the 14Mn-13Cr alloy from Fig. 21, the impact energy decreases gradually with temperature which can be attributed to the presence of the retained austenite and epsilon martensite which transform during the test. The transformation has been confirmed by simple hand magnet experiments which show that there is an increase in the ferromagnetic alpha phase along the fracture surface due to the plastic deformation induced by the testing procedure. The ability of nearly 50% of the alloy to transform results in good toughness properties even at -196°C, i.e., 56 ft-lb (76 joules) at -196°C.

In a manner typical of ferritic materials, the 14Mn-18Cr alloy experiences a sharp decrease in energy absorption ability over a rather small temperature range. The ductile-brittle transition temperature is more pronounced and below approximately -40°C, the alloy behaves in a brittle manner. The controlling microstructural feature is again the 79% alpha phase which is present.

2. 16Mn Alloys

a. Tensile properties. The air-cooled 16Mn-13Cr alloy has a phase composition of 18%γ, 33%ε, and 49%α. Any differences in mechanical properties can be attributed to these differences in phase composition, i.e., the decrease in retained austenite and increase in alpha which results from the quenching treatment. Md temperatures were again observed to be above room temperature, but the stabilities of the metastable phases with respect to plastic deformation have increased over those for the 14Mn-13Cr alloy. A comparison of the room temperature tensile properties from Table IV for the two heat treatments shows that the increased amounts of alpha in the quenched alloys gives higher yield and ultimate strengths. Again, however, the decrease in the volume percentage of metastable phases produces a decrease in uniform elongations and total elongations. After tensile testing, the levels of the alpha phase have risen to just over 50%, while the levels of the epsilon phase have risen to about 40%. With respect to plastic deformation, the epsilon phase seems to be stable at room temperature.

The tensile properties of the air-cooled 16Mn alloys are given in Figs. 9-12. The phase composition of the 16Mn-18Cr (A) alloy is 22%γ, 46%ε, and 32%α and the phase composition of the 16Mn-13Cr (A) alloy is given above. The increase in chromium content has led to the formation of greater initial amounts of epsilon martensite. From Table VII, one observes that after room temperature tensile testing, the 16Mn-18Cr (A) alloy retains only 24% epsilon martensite. Similar values are notes following a -196°C tensile test. The higher chromium level leads to a less stable epsilon with respect to mechanically-induced phase transformations.

The effect of the strain-induced transformations is readily observed in Fig. 9, where high strain hardening rates accompany the gamma to epsilon strain-induced phase transformation in the 16Mn-13Cr (A) alloy. The strain hardening rates are not as high for the 16Mn-18Cr (A) alloy, where the primary strain-induced phase transformation is epsilon to alpha. At -196°C, the ductility, the energy-absorption in tensile testing, and the strain hardening exponent have decreased significantly, which is indicative of the dependence of the mechanical properties on the amount of alpha phase present.

A comparison of the room temperature mechanical properties of the air-cooled and the quenched 16Mn-18Cr alloys shows that the microstructural variations were not significant, since no significant mechanical property differences are noted. It is interesting though that the air-cooled alloy had an epsilon martensite level of 46% while the quenched alloy had an epsilon level of 33%.

b. Charpy V-notch impact properties. The effect of heat treatment on the 16Mn alloys can be assessed readily from Fig. 21. The air-cool treatment increases the impact energies in both the 13Cr and 18Cr alloys, without changing the general shape of the curve. The balanced microstructure attained in the 16Mn-13Cr (A) alloy appears to be very effective in its energy-absorbing ability under impact loading conditions. An extrapolated DBTT for this alloy is -220°C, and the impact energy at -196°C was found to be 85 ft-lb (115 joules).

In a fashion similar to that of the 14Mn-18Cr alloys, the 16Mn-18Cr alloys behaved in a brittle manner at low temperatures. This may be attributed to the instability of the metastable phases for these alloys. Once formed, the alpha is brittle at low temperatures, and provides the brittle phase for cleavage, a low-energy fracture mechanism.

3. 18Mn Alloys

From Table VII, the air-cooled 18Mn-13Cr alloy has a phase composition of 47%γ, 46%ϵ, and 7%α while the quenched alloy has a phase composition of 51%γ, 39%ε, and 10%α. The quench treatment has resulted in a slightly higher alpha level. In addition, it is observed that the air-cooled specimen contains more epsilon than the quenched specimen. A similar observation was made for the 16Mn-18Cr alloy. The phase composition of the 18Mn-18Cr (B) alloy was 18%γ, 30%ε, and 52%α.

The primary influence in the 18Mn-13Cr alloys on the mechanical properties is their high levels of retained austenite. The tensile properties of these alloys are given in Figs. 13-16. Over 90% of the structural phase constituents of the 18Mn-13Cr alloys are metastable phases. From Table VII, there is a 44% net increase in alpha phase for the air-cooled alloy, and a 55% net increase in alpha phase for the quenched alloy following tensile testing at room temperature. This high degree of mechanically-induced transformations results in excellent ductility and uniform elongations.

Figure 13 shows that the yield strengths are fairly constant with temperature. For the air-cooled alloy, there is a drop in yield strength at -78°C, indicating the possible role of a stress-induced phase transformation at this temperature. Strain hardening rates increase with decreasing temperature, and the similarity in initial phase compositions results in a very similar mode of behavior between the air-cooled and quenched 18Mn-13Cr alloys. Excellent ductility properties are shown by Fig. 14, where elongations of 50% for 18Mn-13Cr (B) and 60% for 18Mn-13Cr (A), were obtained at -196°C. The strain-induced phase transformations delay necking and strain-hardening exponents as high as 0.360 were found at -196°C for the 18Mn-13Cr (A) alloy.

This ductile behavior is again revealed in Fig. 16 where the energy absorbed in tensile testing increases steadily with decreasing temperatures. Even at -196°C, the combination of high strain hardening rates and excellent uniform elongations allow energy absorption in tensile testing to reach 270 ft-lbs for the 18Mn-13Cr (A) alloy. The significance of the high retained austenite levels cannot be overemphasized, and since the mechanical stability of the metastable phases is favorable, excellent combinations of strength and ductility are achieved.

For most austenitic stainless steels in the annealed condition, the room-temperature mechanical properties may be given as:[33]

Yield strength	30 - 40 ksi
Ultimate tensile strength	80 - 105 ksi
Elongations	40 - 60%
Reductions in area	60 - 80%

The mechanical properties of the experimental 18Mn-13Cr alloy are equivalent to those of the standard austenitic stainless steels.

The 18Mn-18Cr (B) alloy behaved similarly to the other 18Cr alloys previously discussed. A sharp decrease at low temperatures of the ductility properties may be associated with the large amounts of the alpha phase present and its tendency to behave in a brittle manner at low temperatures.

b. Charpy V-notch impact properties. Excellent impact resistance over the temperature range tested was observed from Fig. 22 for the 18Mn-13Cr alloys. Upper shelf energies of 168 ft-lb (228 joules) and extrapolated DBTTs of -230°C and -245°C for the quenched and air-cooled alloys, respectively, were observed. The considerable amount of retained austenite (≈50%) in these alloys leads to good toughness at very low temperatures. In addition, had magnet inspection revealed that the metastable phases were transforming to the alpha phase during the course of the tests.

The 18Mn-18Cr (B) alloy was typical of the 18Cr alloys, in that the increased alpha phase content provided the primary controlling factor in the impact testing. At room temperature the alpha is ductile and good impact resistance is observed, i.e., 130 ft-lbs (176 joules). As the temperature decreases, the alpha-phase becomes brittle and provides the low-energy crack propagation path. At temperatures below -80°C, the alloy is very brittle, and with the DBTT at -48°C, the cryogenic utility of this alloy is unfavorable.

4. 20Mn Alloys

a. Tensile properties. The tensile properties of the 20Mn-13Cr alloys are interesting because they show little effect from the presence of the sigma phase stringers. The phase compositions from Table VII are 23%γ, 60%ε, and 17%α for the air-cooled alloy, and 37%γ, 48%ε, and 15%α for the quenched alloy. It is observed again that more epsilon has formed with the air-cool treatment, and that there is less retained austenite with the air-cool treatment.

A comparison of room temperature properties from Table IV reveals that the lower level of retained austenite led to a higher yield strength while the ultimate strengths are virtually identical.

Figures 17-20 give the tensile properties of the 20Mn-13Cr (A) alloy versus testing temperature. From Table VII, it is noted that the mechanical stability of the epsilon phase is high even after tensile testing at -196°C, where the alloy still contained 61% of epsilon. One may note that the degree of strain-induced phase transformation in this system is limited. The austenite is fairly stable while the epsilon is extremely stable over the complete range of testing temperatures.

From Fig. 17, the strain hardening rate increases somewhat at -196°C. The reduction in area does drop rapidly below -78°C, and at -196°C virtually no necking of the test specimen was observed. The alloy retained much its ductility at -196°C in that the strain-hardening exponent was found to be 0.318 (i.e., 32% true strain at the point of necking). The energy absorption in tensile testing was found to increase with decreasing temperature to levels similar to those of the 18Mn-13Cr alloy at -196°C.

The tensile properties for the 20Mn-18Cr alloys reveal a profound affect from the large amount of sigma phase present in these alloys. The alloy behaved in a brittle manner at room temperature. The sigma phase tends to act as a brittle constituent and in this case is the primary constituent phase. The presence of large amounts of this ordered sigma phase is dramatically detrimental to the mechanical properties of this alloy.

Once a crack has initiated there is a brittle network for easy propagation. The mechanical properties illustrate the undesirable features of the sigma phase in stainless alloys. Sigma phase is also a problem in standard stainless steels and careful composition and heat treatment temperature control must be maintained to ensure that sigma phase will not form.[33]

b. Charpy V-notch properties. The presence of the sigma phase is responsible for an extreme degradation of Charpy V-notch impact resistance in the 20Mn alloys. Although the presence of the stringers in the 20Mn-13Cr alloys did not affect the tensile properties appreciably, their presence controls the charpy properties.

With the high loading rates and strain rates associated with the Charpy test, the stringers act as low-energy crack propagation paths. Despite the energy absorption abilities of the matrix material, the impact energies are limited by the presence of the stringers. In the tensile test, the deformation of the matrix material could accommodate the applied load since the strain rate is so much lower, but in the Charpy test the crack will propagate along the brittle sigma phase, resulting in low energy absorption ability.

With the high sigma content of the 20Mn-18Cr alloys, resultant impact energy absorption was minimal. Only 4 ft-lb (5 joules) impact energy was observed in the temperature range of -196°C to 23°C.

D. Fracture Properties

A knowledge of the microstructural features permits an evaluation of the fracture properties on the basis of key features. In many cases, it is important to realize how the fracture occurred in order to eliminate fracture initiation features for future alloy development.

1. 14Mn Alloys

The fracture surfaces of Charpy specimens tested at room temperature and at liquid nitrogen temperature are given in Figs. 29 and 30. Also given are the impact energies for which the surfaces correspond (figure captions).

Figures 29a and 29b are fracture surfaces of the 14Mn-13Cr alloy tested at room temperature. The fracture mechanism is microvoid coalescence where voids have nucleated at the interface of inclusion particles and the matrix. Figure 46 shows an EDAX analysis scan of a typical particle found at the fracture surface. The white dots correspond to the counts of intensity for titanium, and the white lines are the positions of the $K\alpha$ and $K\beta$ titanium peaks.

The particles are found to be high in titanium and are presumably gettered interstitial compounds. One can assume that the gettering agents Ti, and Al are indeed effective in tying up the interstitials, thus reducing their effect.

Figures 29c and 29d illustrate the fracture surfaces of the 14Mn-13Cr (B) alloy tested at -196°C. The typical dimple size has reduced indicating that smaller particles, which were not critical at room temperature, can nucleate voids at this low temperature. The interfacial stress[34] may be written as the sum of the local triaxial stress and the stress in the particle-free matrix due to the local plane strain around the particle, i.e.,

$$\sigma_i = \sigma_t + \sigma_y(\varepsilon_p)$$

At low temperatures, the yield stress has increased, thus, $\sigma_t(T_2) > \sigma_t(T_1)$ where $T_2 < T_1$. The triaxial stress increases with work hardening, yield strength, and plane strain. In addition, $\sigma_y(\varepsilon_p)$ increases with work hardening, yield strength, and plane strain. At the crack tip plane strain conditions exist, therefore, at low temperatures the interfacial energies of smaller particles can become critical causing void nuclation. In addition, the stress levels may reach a value greater than the fracture stress of the particles, whereby the particle will fracture thus nucleating a void. One may note in many instances where at the base of a dimple there will be several small pieces of what was one inclusion.

Figure 30a shows the fracture surface of the 14Mn-18Cr (B) alloy tested at room temperature. Again, the fracture surface is fibrous and corresponds to the microvoid coalescence mechanism of fracture. At -196°C, however, the fracture mechanism has changed to cleavage as shown in Figs. 30b, c, and d. In Fig. 30c one notes the striations along cleavage planes representing the microstructural features of the material. In Fig. 30d, the cleavage plane shows sets of striations which lie in parallel directions. These are intersections of the cleavage crack with epsilon martensite bands, or at the boundaries of epsilon martensite bands.

2. <u>16Mn Alloys</u>

In Fig. 31 one has the fracture surfaces of the 16Mn-13Cr (A) alloy tested at room temperature and at -196°C. The fracture is a ductile dimple rupture fracture where dimple sizes do not change appreciably at -196°C. Microvoid coalescence is the fracture mechanism and readily observable are many fractured inclusions where voids have nucleated. At 23°C, one notes many single inclusions at the base of dimples where the local stress state did not exceed the fracture stress of the inclusions.

Figure 32a shows the room temperature fracture surface of the 16Mn-18Cr (A) alloy. The alloy behaves in a ductile manner at high temperatures and the resultant fracture is by microvoid coalescence. Singular inclusions may be seen at the base of the dimples.

A decrease in temperature to -196°C results in a change in fracture mechanism as is evident by Figs. 32b, c. The alloy fails by cleavage at these low temperatures and Fig. 32c shows an area of a cleavage plane along bands of epsilon martensite.

3. 18Mn Alloys

In Figs. 33a and 33b the fracture surfaces for the 18Mn-13Cr (A) alloy tested at 23°C and -196°C, respectively, show the ductile nature of the fracture. A ductile tearing of the material is inferred from the lining up of the dimples in the direction of the impact. Dimple sizes are smaller at -196°C, indicating that voids have been nucleated by smaller particles, which were not critical void nucleation sites at 23°C.

The ductile microvoid coalescence fracture mechanism in this alloy led to an absorption of 168 ft-lb (228 joules) of energy upon Charpy testing at room temperature. At -196°C the impact energy was found to be 122 ft-lb (165 joules). An extrapolated DBTT was calculated to be

≈ -245°C.

In Fig. 34a, the fracture surface for the 18Mn-18Cr alloy tested at room temperature is shown. The ductile failure corresponds to an impact energy of 130 ft-lb (176 joules). As the temperature is decreased, the fracture mechanism changes from microvoid coalescence to cleavage. The DBTT for the 18Mn-18Cr (B) alloy is -48°C. The fracture behavior of this alloy is quite similar to that of the other 18Cr alloys. At -196°C, Figs. 34b, c, d illustrate the cleavage fracture. Figure 34c shows an area where the cleavage crack changed propagation direction across an alpha grain boundary. Figure 34d shows band-like striations corresponding to fracture along epsilon martensite bands in the microstructure.

4. 20Mn Alloys

Figure 35 shows the fracture surfaces for the 20Mn-13Cr (A) alloy tested at 23°C and -196°C. The energy absorbed in Charpy testing was 32 ft-lb (43 joules) and was independent of testing temperature.

In Fig. 35a, delaminations of the material are accompanied by local areas of ductility. Figure 35b shows the ductility associated with localized areas of the fracture surface.

At -196°C, Fig. 35c shows the delaminations to be much more severe and the fracture surface at this temperature shows virtually no signs of ductility. The fracture of the 20Mn-13Cr alloys was controlled by the delamintion of the material along sigma phase boundaries. The low-energy delamination mechanism limited the impact energy to 32 ft-lbs regardless of whether ductility existed locally as in the room temperature case.

Figure 36 shows the fracture surface of the 20Mn-18Cr alloy. The fracture surface corresponds to a brittle failure mode with impact energy of only 4 ft-lbs (5 joules). One notes when comparing Fig. 36b and Fig. 28d that fracture has occurred along the brittle sigma phase. The sigma phase provides a brittle continuous network crack path for easy crack propagation.

E. Effects of Manganese

As the manganese concentration is increased in the 13Cr and 18Cr alloys, there is an increased tendency to form the metastable epsilon phase. Large volume percentages of epsilon phase are associated with manganese levels of 18 and 20%. The decrease in stacking-fault energies at these manganese concentrations promotes the formation of epsilon martensite. Table VII illustrates the effects of manganese concentrations on initial phase compositions. Also, as the epsilon martensite formation is promoted, increases in its mechanical stability with respect to transforming to alpha martensite are also observed. This effect is most noticeable in the 13Cr alloys.

In addition, at manganese levels of 16% or greater, the air cooling treatment also promotes epsilon formation, except in the 16Mn-13Cr alloy, where epsilon content was independent of heat-treatment cooling rate.

Sigma phase formation was observed in the 14Mn-13Cr, 16Mn-13Cr, 18Mn-13Cr, and 20Mn alloys. Except for the 20Mn alloys, the small amounts of sigma phase present did not seem to have an important effect on the mechanical properties. It was only at manganese concentrations of 20% that sigma played a primary role in the mechanical behavior of the alloys. While not having a major effect on the tensile properties, the sigma phase stringers in the 20Mn-13Cr alloy had a profound effect on the impact properties. For the 20Mn-18Cr alloy, sigma phase was the dominant phase, leading to brittle behavior.

Figures 47-50 illustrate the effects of manganese concentrations on the tensile properties of the quenched-and-refrigerated alloys. In Fig. 47, the yield strengths of the 13Cr alloys are seen to drop at 18%Mn. In the 18Mn alloy, this drop may be associated with the high levels of retained austenite (≃50%). In addition, the strain hardening and UTS/YS ratios decrease at 18 and 20%Mn. The stability of the epsilon phase at these manganese concentrations reduces the strain-induced phase transformation effects observed in the 14 and 16Mn alloys.

The yield strengths of the 18Cr alloys increase and the UTS/YS ratios decrease with increasing manganese concentration. At 20Mn, sigma phase formation leads to a high yield strength, but with quite a loss of ductility.

These observations are again clearly seen in Figs. 48-50. For the 13Cr alloys, ductility properties, strain hardening exponents, and tensile-test energy absorption all reach maximum at 18%Mn and drop off at 20%Mn. At 18%Mn, the high retained austenite levels lead to good ductility properties, whereas at 20%Mn, the increased levels of epsilon cause decreases in these ductility-related quantities.

For the 18Cr alloys, the elongations, strain hardening exponents, and tensile testing energy absorption increase up to 18%Mn and then drop off sharply due to sigma formation at 20Mn-18Cr composition levels. At room temperature, the 18Mn-18Cr alloy had an elongation of 40%, showing ductility comparable to the 13Cr alloys, however, these properties deteriorate at lower temperatures.

Figures 51-54 present the tensile results as a function of manganese concentration at room temperature and at low temperatures for the 13Cr alloys. From Fig. 51, the yield strengths increase with increasing manganese levels and are not affected strongly by decreasing the temperature from 23°C to -196°C. The strain-hardening rates are strongly affected by decreasing the temperature and lead to UTS/YS ratios which increase dramatically with decreasing temperatures. From Fig. 52, the elongations reach a maximum at 18Mn, associated with the 50%γ level in this alloy, and increase at -196°C illustrating the excellent ductilities associated with these air-cooled alloys. The strain-hardening exponents, which give the uniform elongations, are shown in Fig. 53. Again it is noted that as the temperature decreases, the uniform elongations increase, i.e., the strain hardening rates in these alloys increase. Finally, in Fig. 54, energy absorption in tensile testing reached values greater than 250 ft-lbs (350 joules) at -196°C. These levels of energy absorption may be attributed to the combination of increased strain hardening and excellent low-temperature ductility observed for these alloys.

The ductile-brittle transition temperature versus manganese concentration is shown in Fig. 57 for the alloys given the quenched-and-refrigerated heat treatment. For the 18Cr alloys, the DBTT decreased for Mn levels of 16 and 18%, with the 16Mn-18Cr (B) alloy having the lowest DBTT. This alloy contained the least initial alpha phase content, and the DBTT behavior may be associated with this observation.

For the 13Cr alloys, the extremely low DBTTs can be attributed to the γ phase contents, as well as the alpha contents. The DBTT increases at 16Mn and decreases again at 18Mn. Also, from Table VII, the gamma phase contents decrease at 16Mn and increase dramatically at 18Mn. The alpha contents decrease sharply at 18Mn. The high levels of austenite lead to the ductility and observed impact resistance at very low temperatures.

F. Effects of Chromium

There was a dramatic difference in the behavior of the 13Cr and 18Cr alloys. In addition to being an alpha former, chromium also decreases the stacking-fault energy of Fe-Mn austenites.[30] It is important to note that at levels of chromium of 13%, the promotion of epsilon phase was indeed observed. However, as the chromium was increased to 18% the predominant effect observed was stabilization of the alpha phase, resulting in initial alpha phase volume percentages which were quite high, typically 45% or greater in the quenched-and-refrigerated alloys. These increased alpha phase levels led to a drastic change in mechanical properties. In general, decreases in ductility and tensile testing energy absorbing ability were observed in the 18Cr alloys as compared to the 13Cr alloys. Also, large increases in DBTTs were observed for the 18Cr alloys.

In the 20Mn alloys, sigma phase formation controlled the mechanical properties. The presence of sigma phase decreased ductility and impact resistance. In the 20Mn-18Cr alloy, sigma phase was the primary constituent of the microstructure, and in this case, the alloy behaved in a very brittle manner even at room temperature. Very small amounts of sigma phase were observed in the 14Mn-13Cr, 16Mn-13Cr, and 18Mn-13Cr alloys, but did not seem to have a deleterious effect on the mechanical properties.

Figures 55 and 56 show the strength properties and ductility properties versus chromium content for the 16Mn and 20Mn alloys given the quench-and-refrigeration heat treatment. The 0Cr and 8Cr data points are taken from Schanfein.[20] From Fig. 55, for the 16Mn alloys, the yield strengths increase with increasing chromium while the ultimate tensile strengths increase, and reach a peak at 13Cr and then drop. The yield and ultimate strengths strengths decrease slightly up to 13Cr and then increase sharply to the 18Cr value for the 20Mn alloys.

Figure 56 shows that for the 16Mn alloys, chromium additions decrease the ductility properties and then further additions tend to improve the elongations while the reductions in area remain relatively constant. On the other hand, the 20Mn alloys revealed enhanced ductility properties with additions of 8Cr, but the ductility properties dropped off rapidly with 13 and 18%Cr additions. At 18Cr, the 20Mn alloys form sigma phase, resulting in a loss of ductility while at 13Cr the decrease in ductility properties may be associated with the high levels of epsilon formed, which tends to be less ductile than the austenitic phase.

Figure 58 shows the variation of DBTT with chromium concentrations for the 16Mn alloys given the quench and refrigeration treatment. Again, the 0Cr and 8Cr are taken from Schanfein.[20] As one readily notes, the DBTT is not affected by chromium additions up to about 13%. At 18Cr the DBTT has increased greatly, presumably due to the stabilization effects that chromium has on the alpha phase. The alpha phase behaves in a brittle manner at low temperatures causing a rise in the DBTT as the alpha phase volume percentage increases.

G. Effects of Temperature

The testing temperature affected the mechanical behavior of all of the alloys except the 20Mn-18Cr alloy. A particularly strong temperature dependence was noted for the 18Cr alloys, where at low temperatures the primary phase constituent, alpha, behaved in a brittle manner. For the 13Cr alloys, the primary effect of temperature was in altering metastable-phase stabilities. In most cases increases in work hardening at low temperatures enhanced uniform elongations. Increases in ultimate tensile strengths as temperature decreased were observed for the 13Cr alloys. In these alloys, the yield strengths were relatively independent of temperature, especially at manganese concentrations of 16% or greater.

This increased strain hardening at lower temperatures led to increasing energy absorption in tensile testing, as well as increased strain hardening exponents. The excellent ductilities observed at low temperatures for the 13Cr alloys makes them prime candidates for cryogenic materials. In addition, the corrosion resistance obtained by the chromium additions (which is discussed in the next section) would permit their use in corrosive applications where ordinary plain carbon or alloyed steels cannot withstand the environment. With DBTT's below -196°C, the 16Mn-13Cr and 18Mn-13Cr air-cooled alloys are prime candidates for these cryogenic applications.

H. Corrosion Behavior

On the basis of the preliminary corrosion testing which has been performed, it is possible to assert that the experimental alloys form a promising base system for further investigation. The corrosion tests performed thus far are discussed in the appendix and summarized in Tables VIII and IX.

Uhlig[35] has emphasized the dependence of corrosion behavior in materials on electrochemical potentials of the various phases. Corrosion can proceed if an electrochemical cell can be established between phases in the material. For this reason it is advantageous to have single phase structures in corrosion inducing environments.

As a result of the compositional variations of the phases present in the Fe-Mn-Cr alloys, electrochemical cells may be activated between phases and corrosion may proceed. The ideal extension of these studies is to design other alloys with austenite-forming and stabilizing elemental additions. In this manner a single phase austenitic structure might be obtained, with improved corrosion resistant properties.

The effects of martensitic transformations are not as severe since no compositional variations between phases exist following the phase transformations. There are inherent energy differences between the austenite and martensitic phases arising from crystal structure differences and dislocation density variation, but these differences do not give rise to severe corrosion problems. Most AISI 300 series stainless steels in fact contain martensitic transformation products in the cold rolled condition.[35]

V. CONCLUSIONS

1. Marked differences in microstructure may be produced by variations in alloy chemistry and heat treatment in Fe-Mn-Cr alloys.
2. Using an air-cool, as opposed to an ice-brine quench and liquid-nitrogen refrigeration, improved the properties of the 18Mn-13Cr and 16Mn-13Cr alloys, therefore, these alloys show excellent commercial potential.
3. Chromium additions of 13 wt% to the 14, 16, and 18% manganese alloys decreased the ductile-brittle transition temperatures dramatically over the corresponding 18 wt% chromium alloys.
4. The 16Mn-13Cr and 18Mn-13Cr alloys show outstanding promise as base systems for replacement austenitic alloys because of their excellent combinations of strength and ductility which compare favorably with those of the standard austenitic stainless steels.
5. The formation of sigma phase in the 20Mn alloys led to a sharp deterioration in mechanical properties as compared to the other alloys investigated.
6. Excellent low-temperature ductility for the 14Mn-13Cr, 16Mn-13Cr, and 18Mn-13Cr alloys points toward their possible utility in crygogenic applications. Additions of 13%Cr also would favor the utility of these alloys in corrosive environments.
7. Increases in the volume percentage of the fcc gamma phase in triplex structures of γ, ϵ, and α led to decreases in the ductile-brittle transition temperature.

APPENDIX

Preliminary Corrosion Property Evaluation

A series of five immersion corrosion tests were made by Battelle Northwest Laboratories, Richland, Washington. The base stainless steel used for comparison was AISI type 347 which has a nominal composition of 17-19Cr, 9-13Ni, 0.08C, 2.0Mn, 1.0Si, 0.045P, 0.030S, with the Nb plus Ta content at least 10 times the C content. This is an austenitic grade which has been stabilized with Nb and Ta additions. The Nb and Ta additions serve to act as carbide formers to prevent and/or reduce the susceptibility to grain-boundary chromium carbide precipitation and resultant sensitization.

The corrosion tests are outlined in Table VIII. In all cases, corrosion rates were reported in thousandths of inches of penetration per month (mils/month). The specimens were annealed at 900°C for two hours and then air-cooled, prior to testing.

Test I is an air-oxidation resistance test carried out at 1100°C for 136 hours. Figure 59 shows the comparative corrosion behavior of 347SS and the 16Mn-13Cr, 16Mn-18Cr, 18Mn-13Cr, 20Mn-13Cr alloys. The general conclusion may be drawn that the experimental alloys exhibited similar oxidation resistance at 1100°C to 347SS.

Test II is an immersion corrosion test utilizing a boiling $6\underline{M}\ NH_4F - 0.5\underline{M}\ NH_4NO_3$ solution. Industrially, this solution is used to declad zircalloy fuel rods where the cladding is generally AISI type 310 austenitic stainless steel. Again, the corrosion behavior of the experimental alloys was found to be similar to that of the 347SS (Fig. 60).

Tests III and IV are designed to test the experimental alloys in environments which cause intergranular attack in AISI 300 series stainless steels. The Huey test (test III) involves exposure to 65% nitric acid while in test IV the solution is a nitric acid-chromium trioxide solution; both solutions have been shown to attack 300 series stainless steels via intergranular corrosion mechanisms. The specimens were tested in the annealed condition and in the annealed plus sensitized condition. Sensitization was performed by a one-hour anneal at 675°C followed by a water quench.

Figure 61 shows the results of the Huey test. The experimental alloys had corrosion rates which were an order of magnitude greater than that of 347SS. In every case, corrosion rates rose following the sensitization treatment.

Figure 62 shows the results of test IV. In this instance, the experimental alloys behaved similarly to 347SS in the annealed condition but had corrosion rates an order of magnitude lower than those for 347SS in the sensitized condition. In each case, the corrosion rates of the experimental alloys decreased following the sensitization treatment.

The apparent divergence in conclusions for these two test indicates that an intergranular attack test is not applicable to the experimental alloys. Specimens of the experimental alloys revealed no intergranular attack when cross-sectioned, polished, and viewed by optical microscopy. The attack seemed to be simply a general corrosion attack and could not be linked to any grain-boundary precipitation reactions. This would be expected since the experimental alloys do not contain carbon as an alloying addition, thereby preventing $Cr_{23}C_6$ or other complex carbide precipitation reactions.

Test V involved an exposure of the experimental alloys to an $FeCl_3$ solution at room temperature to evaluate resistance to pitting and crevice attack. Conditions conducive to crevice attack were produced by placing a rubber band around the test specimen. All experimental alloys were prone to pitting and the 16Mn-13Cr alloy was susceptible to crevice attack as well. 347SS was susceptible to crevice attack.

The results of these tests are summarized in Table IX.

REFERENCES

1. V. F. Zackay, E. R. Parker, J. W. Morris, Jr., and G. Thomas, The Applications of Materials Science to the Design of Engineering Alloys, LBL-2261 preprint, October 1973.
2. American Society for Metals Handbook, Volume 1, 8th edition, 1961, p. 408.
3. V. F. Zackay and E. R. Parker, Progress in Ferrous Alloy Design, presented at Battelle Northwest Harrison Springs Conference, LBL-4112, pp. 8-13.
4. C. H. Samans, Metallic Materials in Engineering, Fifth Printing, The Macmillon Company, (c) 1963, pp. 417-459.
5. R. M. Brick, R. B. Gordon, and A. Phillips, Structure and Properties of Alloys, Third Edition, McGraw-Hill Book Company, (c) 1965, pp. 339-358.
6. A. Levy, Project Engineer, Lawrence Berkeley Laboratory, private communication.
7. V. F. Zackay, J. F. Carlson, and P. L. Jackson, High Nitrogen Austenitic Cr-Mn Steels, ASM Trans. 48, 509-525 (1956).
8. V. F. Zackay, E. R. Parker, D. Fahr, and R. Busch, The Enhancement of Ductility in High Strength Steels, ASM Trans., Quart. 60, (2), 252-259 (1967).
9. D. Bhandarkar, V. F. Zackay, and E. R. Parker, The Role of Deformation Induced Phase Transformations in the Plasticity of Some Iron-Base Alloys, LBL-2775, August 1974.

10. E. R. Parker and V. F. Zackay, Strong and Ductile Steels, Scientific American 219, 36-45 (1968).

11. J. P. Bressanelli and A. Moskowitz, Effects of Strain Rate, Temperature, and composition on Tensile Properties of Metastable Austenitic Stainless Steels, ASM Trans. 59, 223-239 (1966).

12. A. R. Troiano and F. T. McGuire, A Study of the Iron-Rich Iron-Manganese Alloys, ASM Trans. 31(2), 340-364 (1943).

13. R. K. Buhr, S. L. Gertsman, and J. Reekie, Transformation Products in Cold-Worked Steel, ASM Trans. 49, 706-720 (1957).

14. D. W. Gomersall and J. Gordon-Parr, Transformations in Iron-Manganese Alloys, Journal of the Iron and Steel Institute, pp. 275-279, March (1965).

15. D. J. Drobnjak, and J. Gordon-Parr, Thermomechanical Treatment and Transformation Characteristics of Fe-Mn Austenites, Metallurgical Transactions 1, 1521-1526 (1970).

16. W. Jolley, Effect of Mn and Ni on Impact Properties of Fe and Fe-C Alloys, Journal of the Iron and Steel Institute, pp. 170-173 February (1968).

17. K. S. Raghavan, A. S. Sastri, and M. J. Marcinkowski, Nature of the Work-Hardening Behavior in Hadfield's Manganese Steel, Transactions of the Metallurgical Society of AIME 245, 1569-1575 (1969).

18. M. J. Roberts, Effect of Transformation Substructure on the Strength and Toughness of Fe-Mn Alloys, Metallurgical Transactions 1, 3287-3294 (1970).

19. A. Holden, J. D. Bolten, and E. R. Petty, Structure and Properties of Iron-Manganese Alloys, Journal of the Iron and Steel Institute, pp. 721-728, September (1971).

20. M. J. Schanfein, The Cryogenic Properties of Fe-Mn and Fe-Mn-Cr Alloys, M.S. Thesis, LBL-2749, August (1974).

21. G. T. Haddick, Optimization of Strength and Ductility in Fe-Mn TRIP Steels, M.S. Thesis, LBL-3986, June (1976).

22. United States Steel, The Making, Shaping, and Treating of Steel, 8th Edition, (c) 1964, pp. 1111-1131.

23. R. Lindberg, Engineer, Lawrence Berkeley Laboratory, private communication.

24. H. Schumann, Martensitic Transformations in Low Carbon Manganese Steels, Arch. Eisenluttenwesen 39, 647-656 (1967).

25. J. Dash and H. M. Otte, The Martensite Transformation in Stainless Steel, Acta Metallurgica 11, 1169-1178 (1963).

26. T. Ooka and K. Suemune, Electron Microscopic Structures of Iron-Manganese Alloys, Nippon Kinzuko Jakkai-Si 30(5), 428-434 (1966).

27. B. Cina, A Transitional h.c.p. Phase in the $\gamma \rightarrow \alpha$ Transformation in Certain Fe-Base Alloys, Acta Metallurgica 6, 748-762 (1958).

28. J. S. Dunning, The Effect of Stacking Fault Energy on the Strain Induced Martensite Transformation and Tensile Characteristics in Iron Based Alloys, Ph.D. Thesis, UCRL-19052, December (1969).

29. P. L. Mangonon, Jr. and G. Thomas, The Martensite Phases in 304 Stainless Steel, UCRL-18868 preprint, June (1969).

30. P. M. Kelley, The Martensite Transformation in Steels with Low Stacking Fault Energy, Acta Metallurgica 13, 635-646 (1965).

31. J. Gordon-Parr, The Crystallographic Relationship Between the Phases γ and ε in the System Iron-Manganese, Acta Metallurgica 5, 842-843 (1952).

32. W. B. Pearson, Lattice Spacings and Structures of Metals and Alloys, Vol. 2, First Edition, (c) 1967, pp. 211 and 213.

33. American Society for Metals, Source Book on Stainless Steels, First Printing, copyright 1976, pp. 62-172, 384-392.

34. R. O. Ritchie, Miller Fellow, Lawrence Berkeley Laboratory, private communication.

35. H. H. Uhlig, Corrosion and Corrosion Control, Second Edition, copyright 1963, pp. 298-300.

36. B. D. Cullity, Elements of X-Ray Diffraction, Third Printing, Addison-Wesley Publishing Company, copyright 1956, pp. 391-396.

ACKNOWLEDGEMENTS

The author is extremely grateful to Professors E. R. Parker and V. F. Zackay for their guidance and encouragement throughout the course of this research. Appreciation is also extended to Professors S. F. Ravitz and F. E. Hauser for reviewing the manuscript. Special thanks go the Professor G. Thomas, who encouraged me during the early part of my stay at Berkeley.

Deep appreciation is also extended to all of the fellow graduate students, whose discussions and interchange aided me immensely. To single out any one particular student would be a slight to the others. Thanks are also extended to the technical and support staff of the Materials and Molecular Research Division as well as my research helpers at the laboratory.

My deepest thanks go to my wife, Denise, whose patience and understanding gave me the inspiration to continue in graduate school.

This research was completed with support from the United States Energy Research and Development Administration.

Table I. Chemical Compositions and Alloy Designations.

Alloy Designation	Fe	Mn	Cr	Al	Ti
14Mn-13Cr	bal.	14	13	0.10	0.15
14Mn-18Cr	bal.	14	18	0.10	0.15
16Mn-13Cr	bal.	16	13	0.10	0.15
16Mn-18Cr	bal.	16	18	0.10	0.15
18Mn-13Cr	bal.	18	13	0.10	0.15
18Mn-18Cr	bal.	18	18	0.10	0.15
20Mn-13Cr	bal.	20	13	0.10	0.15
20Mn-18Cr	bal.	20	18	0.10	0.15

Table II. Heat Treatments.

(A) 900 °C (2 hours) → Air Cool to Room Temperature

(B) 900 °C (2 hours) → Ice Brine Quench → Liquid Nitrogen Refrigeration → Room Temperature

Note: Ice Brine Quench (10% Salt Solution).

Table III. Rockwell "C" Hardness and Heat Treatments of Experimental Alloys.

Alloy Designation	Heat Treatment	Hardness (Rc)
14Mn-13Cr	B	18.2
14Mn-18Cr	B	7.5
16Mn-13Cr	A	6.6
16Mn-13Cr	B	23.0
16Mn-18Cr	A	11.4
16Mn-18Cr	B	11.0
18Mn-13Cr	A	7.3
18Mn-13Cr	B	9.8
18Mn-18Cr	B	9.3
20Mn-13Cr	A	19.4
20Mn-13Cr	B	18.0
20Mn-18Cr	A	42.8
20Mn-18Cr	B	45.0

Table IV. Tensile Properties of Experimental Alloys.

Alloy Designation	Heat Treatment	Testing Temperature (°C)	Y.S. (KSI)	Y.S. (MPa)	U.T.S. (KSI)	U.T.S. (MPa)	Elongation (%)	Reduction in area (%)	Strain hardening exponent, n	Energy Absorbed (ft-lb)	Energy Absorbed (joules)
14Mn-13Cr	B	23	53.3	368	116.8	805	32	66	0.132	104	141
		-78	63.4	437	148.9	1027	30	71	0.183	156	212
		-196	75.6	521	196.1	1352	31	62	0.115	215	292
14Mn-18Cr	B	23	46.1	318	86.6	597	31	70	0.130	85	115
		-78	56.1	387	108.2	746	27	64	0.134	107	145
		-196	77.5	534	124.0	855	3	3	0.036	18	24
16Mn-13Cr	B	23	55.9	385	117.0	807	27	62	0.096	88	119
	A	23	44.9	310	100.2	691	43	80	0.238	149	202
		-78	43.1	297	125.5	865	42	69	0.229	162	220
		-196	45.6	314	161.4	1113	53	67	0.264	250	339
16Mn-18Cr	B	23	56.4	389	89.4	616	35	68	0.174	102	138
	A	23	52.9	365	89.2	615	33	69	0.179	103	140
		-78	54.3	374	107.0	738	37	74	0.220	146	198
		-196	65.5	452	120.3	829	7	8	0.062	36	49
18Mn-13Cr	B	23	45.0	310	92.4	637	52	82	0.283	160	217
		-78	39.0	269	113.9	785	53	82	0.259	198	269
		-196	43.4	299	163.3	1126	50	70	0.305	250	340
	A	23	43.7	301	92.1	635	58	82	0.326	176	238
		-78	48.2	332	114.6	790	57	81	0.341	212	287
		-196	53.4	368	161.2	1111	60	71	0.360	270	366
18Mn-18Cr	B	23	61.2	422	84.3	581	39	65	0.186	113	153
		-78	70.0	483	106.0	731	38	69	0.224	152	206
		-196	87.8	605	131.3	905	11	11	0.102	57	77
20Mn-13Cr	B	23	58.3	402	97.0	669	42	51	0.233	117	159
	A	23	65.6	452	98.7	681	36	69	0.228	139	188
		-78	66.0	455	116.9	806	35	70	0.286	197	267
		-196	78.7	543	164.2	1132	34	34	0.318	265	359
20Mn-18Cr	B	23	93.0	641	123.0	848	5	4	0.049	38	52
	A	23	122.2	843	146.4	1009	4	4	0.023	25	34

Table V. Charpy V-Notch Impact Properties of Experimental Alloys

Alloy Designation	Heat Treatment	Impact Energy at 23°C (ft-lb)	(joules)	DBTT* (°C)	Impact Energy at -196°C (ft-lb)	(joules)
14Mn-13Cr	B	130	176	-173	56	76
14Mn-18Cr	B	115	156	-15	4	5
16Mn-13Cr	B	88	119	-148	14	19
	A	140	190	<-196(≃-220)	85	115
16Mn-18Cr	B	108	146	-56	4	5
	A	148	201	-40	8	11
18Mn-13Cr	B	168	228	<-196(-230)	112	152
	A	168	228	<-196(-245)	122	165
18Mn-18Cr	B	130	176	-48	4	5
20Mn-13Cr	B	28	38	-0-	28	38
	A	32	43	-0-	32	43
20Mn-18Cr	B	4	5	-0-	4	5
	A	4	5	-0-	4	5

*DBTT ≡ that temperature at which the Charpy absorbed was equal to one-half the value of the Charpy V-notch energy at room temperature.

Table VI. Phase Transformation Behavior as Determined via Thermodilatometric Experiments.

Alloy Designation	On Heating	On Cooling
14Mn-13Cr	$\varepsilon \rightarrow \gamma$ @ 150 °C	$\gamma \rightarrow \varepsilon$ @ 140 °C
14Mn-18Cr	$\varepsilon \rightarrow \gamma$ @ 145 °C	$\gamma \rightarrow \varepsilon$ @ 60 °C
16Mn-13Cr	$\varepsilon \rightarrow \gamma$ @ 170 °C	$\gamma \rightarrow \varepsilon$ @ 100 °C
16Mn-18Cr	$\varepsilon \rightarrow \gamma$ @ 170 °C	$\gamma \rightarrow \varepsilon$ @ 55 °C
18Mn-13Cr	$\varepsilon \rightarrow \gamma$ @ 165 °C	$\gamma \rightarrow \varepsilon$ @ 100 °C
18Mn-18Cr	$\varepsilon \rightarrow \gamma$ @ 160 °C	$\gamma \rightarrow \varepsilon$ @ 85 °C
20Mn-13Cr	$\varepsilon \rightarrow \gamma$ @ 150 °C	$\gamma \rightarrow \varepsilon$ @ 80 °C
20Mn-18Cr	No phase transitions observed	

Table VII. Volume Percentages of Phases Present as Determined via X-Ray Analysis

Alloy Designation	Heat Treatment	As Heat Treated			After Tensile Testing at 23 °C			After Tensile Testing at -196 °C		
		γ	ε	α	γ	ε	α	γ	ε	α
14Mn-13Cr	B	24	22	54	0	0	100	0	0	100
14Mn-18Cr	B	16	5	79	0	5	95	0	3	97
16Mn-13Cr	A	31	33	36	8	40	52	4	42	54
16Mn-13Cr	B	18	33	49	6	43	51	-	-	-
16Mn-18Cr	A	22	46	32	12	24	64	7	26	67
16Mn-18Cr	B	21	33	46	10	20	70	-	-	-
18Mn-13Cr	A	47	46	7	16	33	51	9	24	67
18Mn-13Cr	B	51	39	10	7	28	65	5	26	69
18Mn-18Cr	B	18	30	52	5	19	76	4	13	83
20Mn-13Cr	A	23	60	17	14	60	26	13	61	26
20Mn-13Cr	B	37	48	15	26	51	23	-	-	-

Table VIII. Preliminary Corrosion Tests.

Test I - High Temperature Air-Oxidation Test

1. Test tempeature = 1100°C
2. Test duration = 136 hours
3. Specimens were descaled in alkaline permanganate-citric acid.

Test II - Boiling 6M NH_4F - 0.5M NH_4NO_3

1. Test duration = 24 hours
2. This solution is used to declad zircalloy fuel rods.

Test III - Huey Test

1. Boiling 65 w/o Nitric Acid
2. Test duration = 48 hours
3. Five test specimens were averaged for each composition in each condition.
4. Sensitization ⇒ one-hour exposure of annealed specimens at 675°C followed by a water quench.

Test IV - Boiling 6M HNO_3 - 0.01M CO_3

1. Test duration = 48 hours
2. Sensitization ⇒ same as Test III.

Test V - 0.1 M $FeCl_3$

1. Test temperature = 25°C
2. Test duration = 24 hours

Table IX. Preliminary Corrosion Test Results.

Alloy	Test I(1) Oxidation in air at 1100 °C (mils/mo)	Test II(2) Boiling 6M NH_4F -0.5M NH_4NO_3 (mils/mo)	Test III(3) Huey Rate (mils/mo)	Test IV(4) Boiling 6M HNO_3 -0.01M CrO_3 (mils/mo)	Test V(5) 0.1 M $FeCl_3$ 25 °C (mils/mo)
16Mn-13Cr annealed	24.3	27.5	12.6	3.2	pitting and crevice attack
16Mn-13Cr sensitized	-	-	21.5	0.5	
16Mn-18Cr annealed	13.9	35.9	11.8	4.1	pitting
16Mn-18Cr sensitized	-	-	18.7	0.4	
18Mn-13Cr annealed	25.8	24.6	14.4	1.5	pitting
18Mn-13Cr sensitized	-	-	18.4	1.1	
20Mn-13Cr annealed	11.9	23.7	15.6	4.4	pitting
20Mn-13Cr sensitized	-	-	19.3	2.9	
347SS-annealed	29.6	41.2	0.5-1.0	4.3	crevice attack
347SS sensitized	-	-	1.0-2.0	14.1	

(1) 136-hour exposures
(2) 24-hour exposures
(3) Average of five 48-hour exposures to boiling 65 w/o HNO_3
(4) 48-hour exposures
(5) 24-hour exposures

FIGURE CAPTIONS

Fig. 1. Strength properties versus manganese concentration for the Fe-Mn binary system.

Fig. 2. Ductility properties versus manganese concentration for the Fe-Mn binary system.

Fig. 3. Comparison of the Fe-Ni and Fe-Mn binary systems.

Fig. 4. (a) ASTM standard E23-72 Charpy V-notch impact specimen

(b) ASTM standard E8-69 round tensile specimen.

(c) Dimension specifications of the dilatometer specimens

Fig. 5. Strength properties versus testing temperature for the 14Mn-13Cr and 14Mn-18Cr alloys, heat treatment (B).

Fig. 6. Ductility properties versus testing temperature for the 14Mn-13Cr and 14Mn-18Cr alloys, heat treatment (B).

Fig. 7. Strain hardening exponent versus testing temperature for the 14Mn-13Cr and 14Mn-18Cr alloys, heat treatment (B).

Fig. 8. Energy absorbed in tensile testing versus testing temperature for the 14Mn-13Cr and 14Mn-18Cr alloys, heat treatment (B).

Fig. 9. Strength properties versus testing temperature for the 16Mn-13Cr and 16Mn-18Cr alloys, heat treatment (A).

Fig. 10. Ductility properties versus testing temperature for the 16Mn-13Cr and 16Mn-18Cr alloys, heat treatment (A).

Fig. 11. Strain hardening exponent versus testing temperature for the 16Mn-13Cr and 16Mn-18Cr alloys, heat treatment (A).

Fig. 12. Energy absorbed in tensile testing versus testing temperature for the 16Mn-13Cr and 16Mn-18Cr alloys, heat treatment (A).

Fig. 13. Strength properties versus testing temperature for the 18Mn-13Cr alloys, heat treatments (A) and (B), and 18Mn-18Cr alloys, heat treatment (B).

Fig. 14. Ductility properties versus testing temperature for the 18Mn-13Cr alloy, heat treatments (A) and (B), and 18Mn-18Cr alloys, heat treatment (B).

Fig. 15. Strain hardening exponent versus testing temperature for the 18Mn-13Cr alloys, heat treatments (A) and (B), and 18Mn-18Cr alloy, heat treatment (B).

Fig. 16. Energy absorbed in tensile testing versus testing temperature for the 18Mn-13Cr alloys, heat treatments (A) and (B), and 18Mn-18Cr alloy, heat treatment (B).

Fig. 17. Strength properties versus testing temperature for the 20Mn-13Cr alloy, heat treatment (A).

Fig. 18. Ductility properties versus testing temperature for the 20Mn-13Cr alloy, heat treatment (A).

Fig. 19. Strain hardening exponent versus testing temperature for the 20Mn-13Cr alloy, heat treatment (A).

Fig. 20. Energy absorbed in tensile testing versus testing temperature for the 20Mn-13Cr alloy, heat treatment (A).

Fig. 21. Charpy V-notch impact energy versus testing temperature for the 14Mn and 16Mn alloys.

Fig. 22. Charpy V-notch impact energy versus testing temperature for the 18Mn and 20Mn alloys.

Fig. 23. Optical micrographs of the 14Mn alloys, heat treatment (B):

(a) 14Mn-13Cr

(b) 14Mn-13Cr

(c) 14Mn-18Cr

(d) 14Mn-18Cr

Fig. 24. Optical micrographs of the 16Mn-13Cr alloys:

(a) Heat treatment (B)

(b) Heat treatment (B)

(c) Heat treatment (A)

(d) Heat treatment (A)

Fig. 25. Optical micrographs of the 16Mn-18Cr alloys:

(a) Heat treatment (B)

(b) Heat treatment (B)

(c) Heat treatment (A)

(d) Heat treatment (A)

Fig. 26. Optical micrographs of the 18Mn alloys:

(a) 18Mn-13Cr, heat treatment (B)

(b) 18Mn-13Cr, heat treatment (A)

(c) 18Mn-18Cr, heat treatment (B)

(d) 18Mn-18Cr, heat treatment (B)

Fig. 27. Optical micrographs of the 20Mn-13Cr alloys:

(a) Heat treatment (B)

(b) Heat treatment (A)

(c) SEM micrograph of σ phase in the 20Mn-13Cr (A) alloy.

Fig. 28. Optical micrographs of the 20Mn-18Cr alloys:

(a) Heat treatment (B)

(b) Heat treatment (B)

(c) Heat treatment (A)

(d) Heat treatment (A)

Fig. 29. Scanning electron fractographs fo the 14Mn-13Cr (B) alloy:

(a) Tested at room temperature, (130 ft-lb)

(b) Tested at room temperature, (130 ft-lb)

(c) Tested at -196°C, (56 ft-lb)

(c) Tested at -196°C, (56 ft-lb)

Fig. 30. Scanning electron fractographs of the 14Mn-18Cr (B) alloy:

(a) Tested at room temperature, (115 ft-lb)

(b) Tested at -196°C, (4 ft-lb)

(c) Tested at -196°C, (4 ft-lb)

(d) Tested at -196°C, (4 ft-lb)

Fig. 31. Scanning electron fractographs of the 16Mn-13Cr (A) alloy:

(a) Tested at room temperature, (140 ft-lb)

(b) Tested at -196°C, (85 ft-lb)

Fig. 32. Scanning electron fractographs of the 16Mn-18Cr (A) alloy:

(a) Tested at room temperature, (148 ft-lb)

(b) Tested at -196°C, (8 ft-lb)

Fig. 33. Scanning electron fractographs of the 18Mn-13Cr (A) alloy:

(a) Tested at room temperature, (168 ft-lb)

(b) Tested at -196°C, (122 ft-lb)

Fig. 34. Scanning electron fractographs of the 18Mn-18Cr (B) alloy:

(a) Tested at room temperature, (130 ft-lb)

(b) Tested at -196°C, (4 ft-lb)

(c) Tested at -196°C, (4 ft-lb)

(d) Tested at -196°C, (4 ft-lb)

Fig. 35. Scanning electron fractographs of the 20Mn-13Cr (A) alloy:

(a) Tested at room temperature, (32 ft-lb)

(b) Tested at room temperature, (32 ft-lb)

(c) Tested at -196°C, (32 ft-lb)

(d) Tested at -196°C, (32 ft-lb)

Fig. 36. Scanning electron fractographs of the 20Mn-18Cr (A) alloy:

(a) Tested at room temperature (4 ft-lb)

(b) Tested at room temperature (4 ft-lb)

Fig. 37. Scanning electron microscopy EDAX analysis scan of alpha and gamma phases in the 16Mn-18Cr (A) alloy.

Fig. 38. Scanning electron microscopy EDAX analysis scans of sigma and alpha phases in the 20Mn-18Cr (A) alloy.

Fig. 39. Scanning electron micrographs of sigma phase stringer in the 14Mn-13Cr (B) alloy.

Fig. 40. Scanning electron microscopy EDAX analysis scans of the 14Mn-13Cr (B) alloy:

(a) matrix material

(b) sigma phase

Fig. 41. Scanning electron micrographs of sigma phase stringer in the 16Mn-13Cr (A) alloy.

Fig. 42. Scanning electron microscopy EDAX analysis scans of the 16Mn-13Cr (A) alloy:

(a) matrix material

(b) sigma phase

Fig. 43. Scanning electron micrographs of sigma phase stringer in the 18Mn-13Cr (A) alloy.

Fig. 44. Scanning electron microscopy EDAX analysis scans of the 18Mn-13Cr (A) alloy:

(a) matrix material

(b) sigma phase

Fig. 45. Scanning electron microscopy EDAX analysis scans of the 20Mn-13Cr (A) alloy:

(a) matrix material

(b) sigma phase

Fig. 46. Scanning electron microscopy EDAX analysis scan of a fracture surface inclusion particle in the 18Mn-13Cr (A) alloy.

Fig. 47. Room temperature strength properties versus manganese concentration of the Fe-Mn-Cr alloys, heat treatment (B).

Fig. 48. Room temperature ductility properties versus manganese concentration of the Fe-Mn-Cr alloys, heat treatment (B).

Fig. 49. Room temperature strain hardening exponents versus manganese concentration of the Fe-Mn-Cr alloys, heat treatment (B).

Fig. 50. Room temperature energy absorption in tensile testing versus manganese concentration of the Fe-Mn-Cr alloys, heat treatment (B).

Fig. 51. Room temperature and -196°C strength properties versus manganese concentration of the Fe-Mn-Cr alloys, heat treatment (A).

Fig. 52. Room temperature and -196°C ductility properties versus manganese concentration of the Fe-Mn-Cr alloys, heat treatment (A).

Fig. 53. Room temperature, -78°C, and -196°C strain hardening exponents versus manganese concentration of the Fe-Mn-Cr alloys, heat treatment (A).

Fig. 54. Room temperature, -78°C, and -196°C energy absorption in tensile testing versus manganese concentration of the Fe-Mn-Cr alloys, heat treatment (A).

Fig. 55. Room temperature strength properties versus chromium concentration of the Fe-Mn-Cr alloys, heat treatment (B).

Fig. 56. Room temperature ductility properties versus chromium concentration of the Fe-Mn-Cr alloys, heat treatment (B).

Fig. 57. Ductile-brittle transition temperature versus manganese concentration of the Fe-Mn-Cr alloys, heat treatment (B).

Fig. 58. Ductile-brittle transition temperature versus chromium concentration of the Fe-16Mn-Cr alloys, heat treatment (B).

Fig. 59. Oxidation rates in air, at 1100°C, for AISI 347 stainless steel, and for several of the experimental alloys.

Fig. 60. Corrosion rates in a boiling $6\underline{M}$ NH_4F - $0.5\underline{M}$ NH_4NO_3 solution for AISI 347 stainless steel, and for several of the experimental alloys.

Fig. 61. Huey rates (65 wt% boiling HNO_3) for AISI 347 stainless steel, and for several of the experimental alloys; in the annealed and sensitized condition.

Fig. 62. Corrosion rates in a boiling 6$\underline{M}$ HNO_3 - 0.01$\underline{M}$ CO_3 solution for AISI 347 stainless steel, and for several of the experimental alloys.

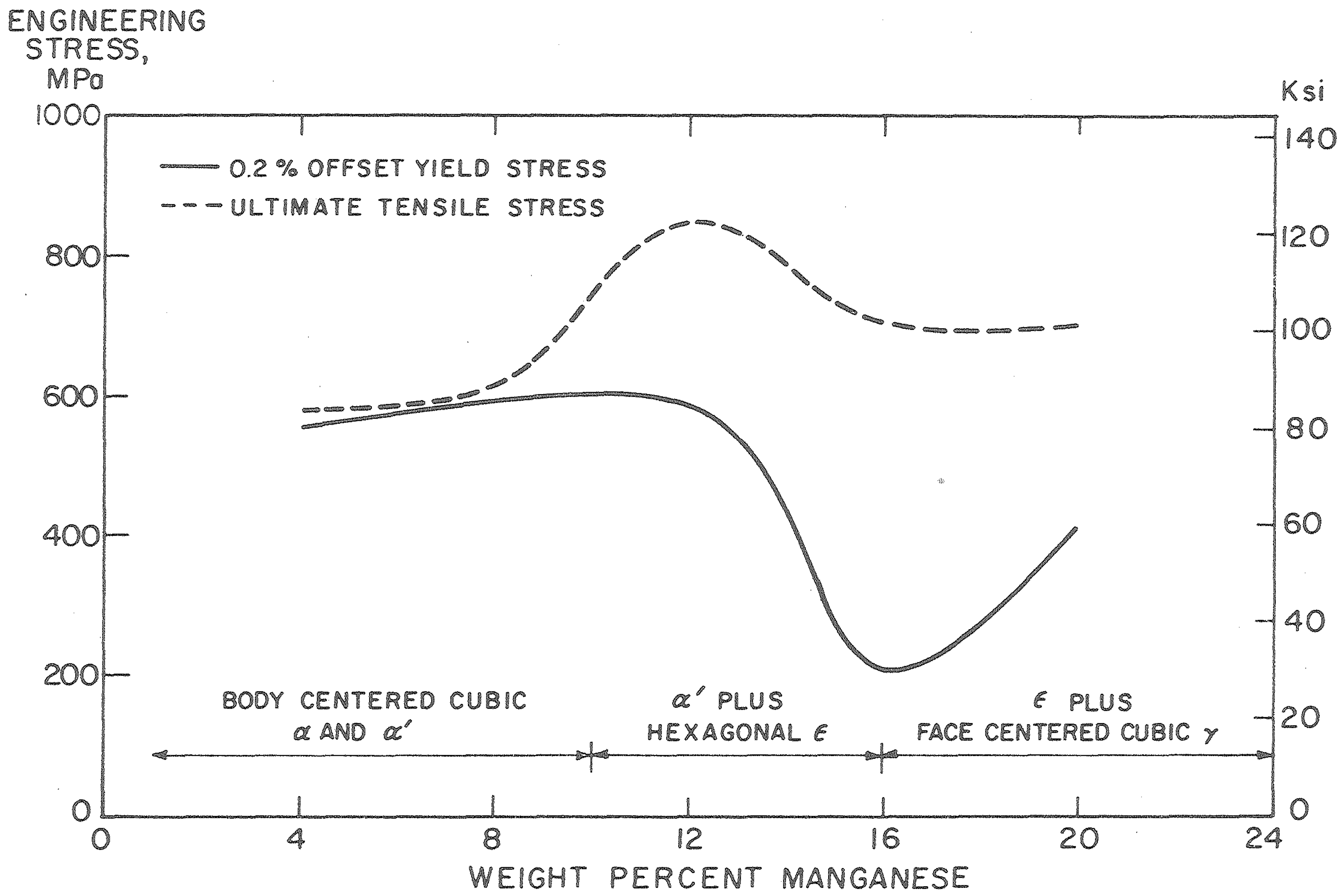

XBL 745 - 6257A

Fig. 1.

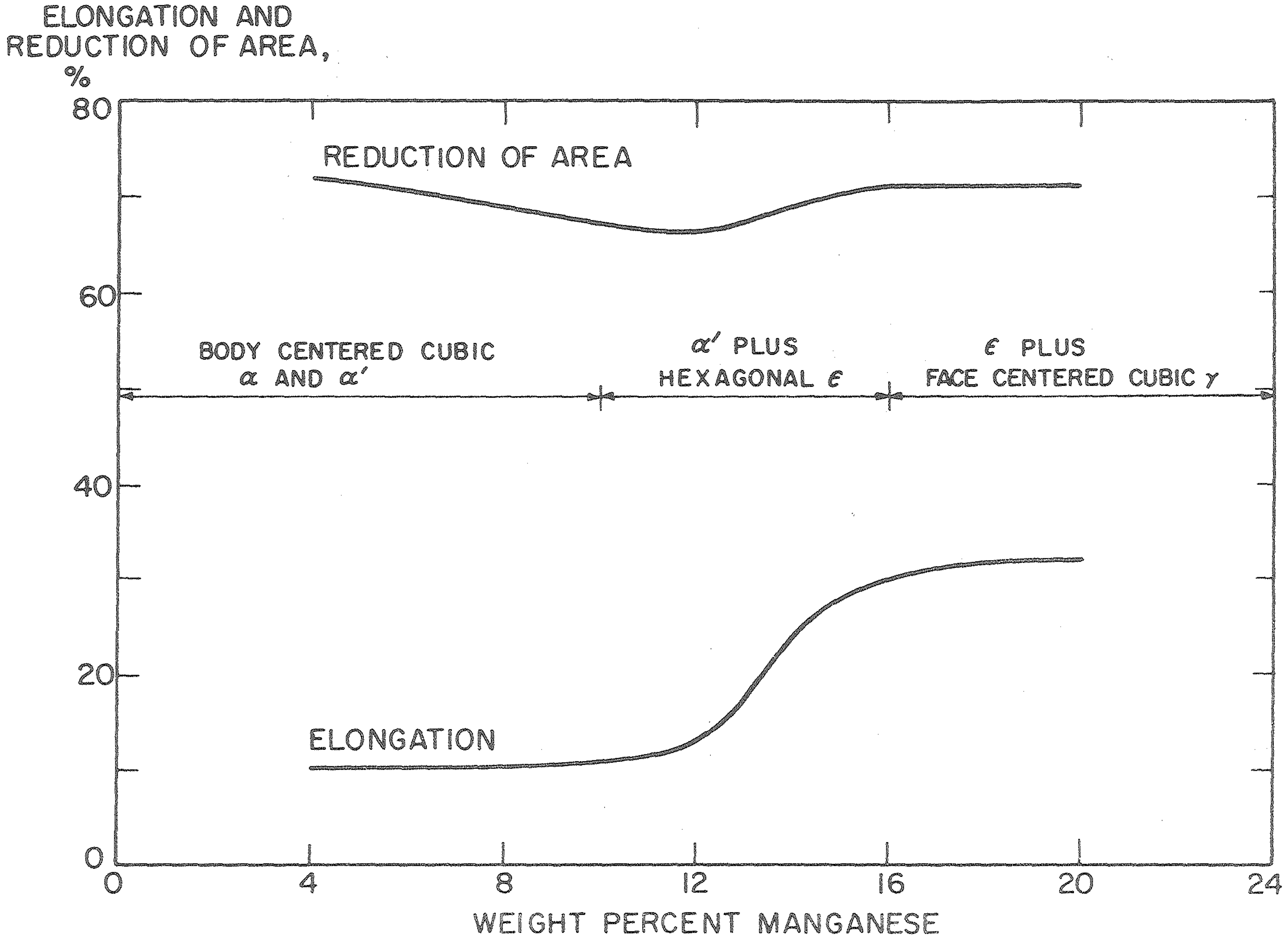

XBL-745 6256A

Fig. 2.

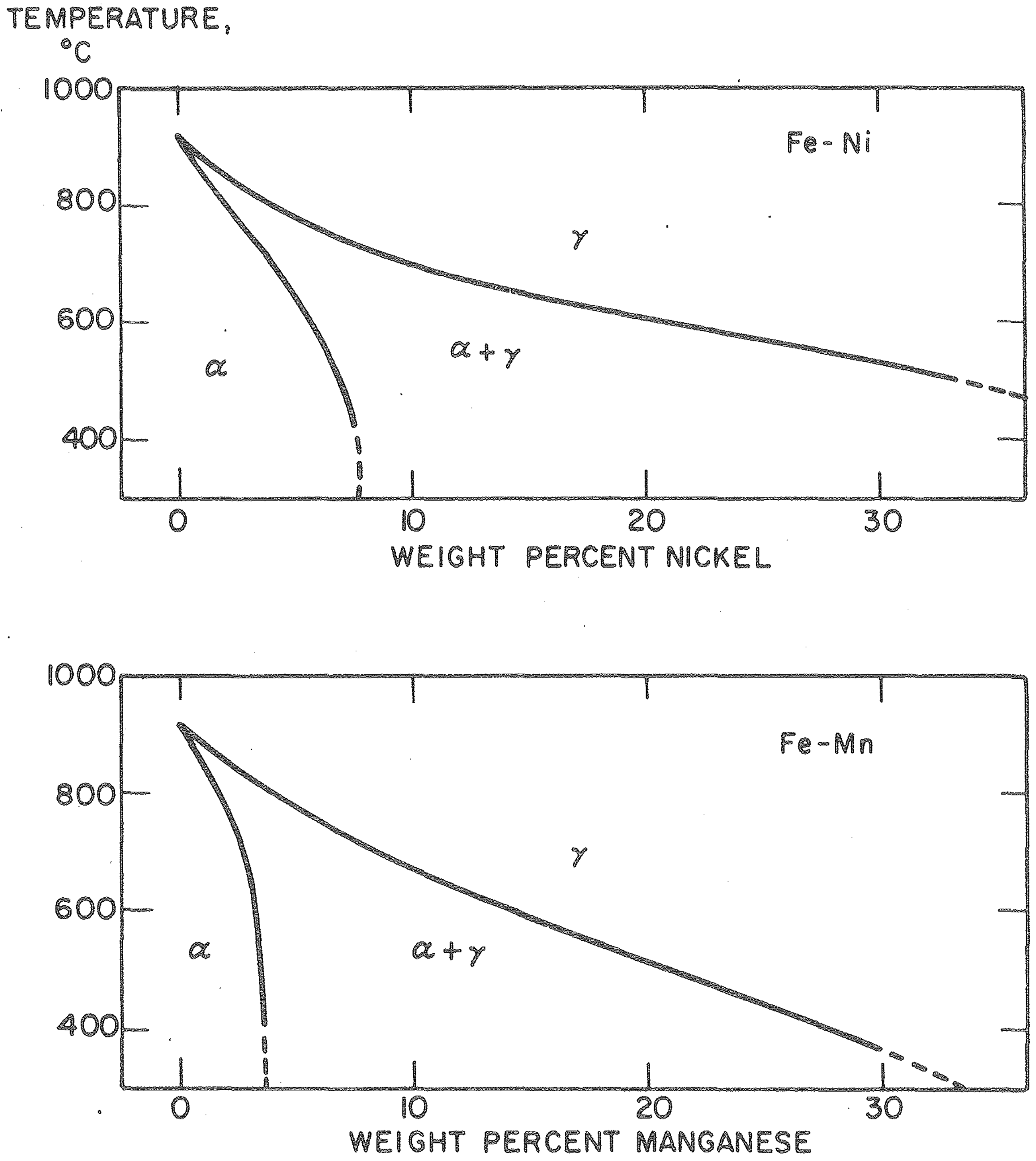

XBL 769-7500

Fig. 3.

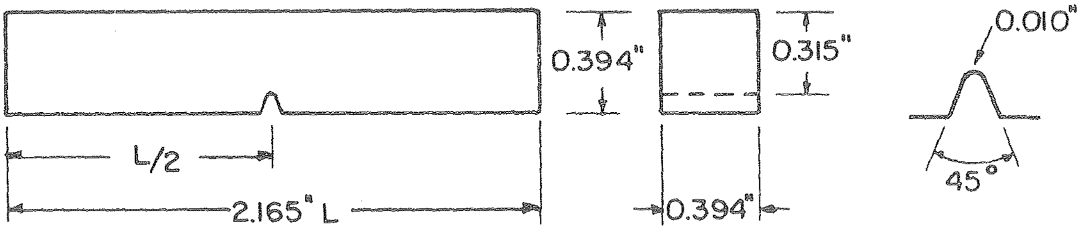

(a) CHARPY V-NOTCH IMPACT SPECIMEN

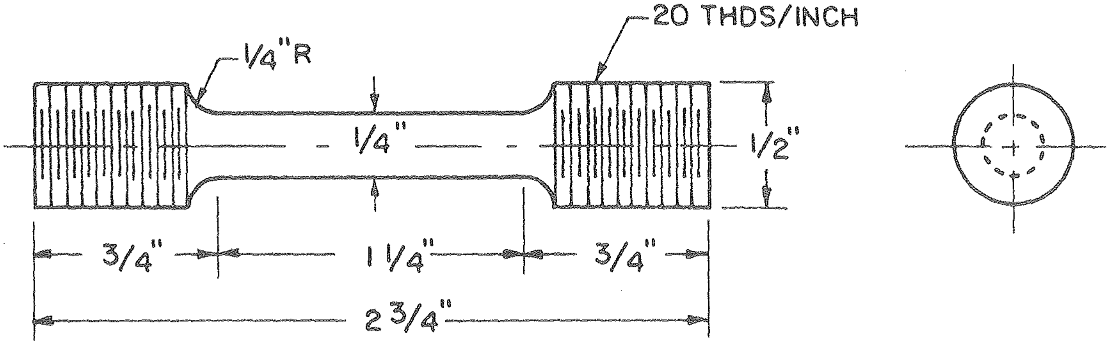

(b) ROUND TENSILE SPECIMEN

XBL 735-6189

Fig. 4.

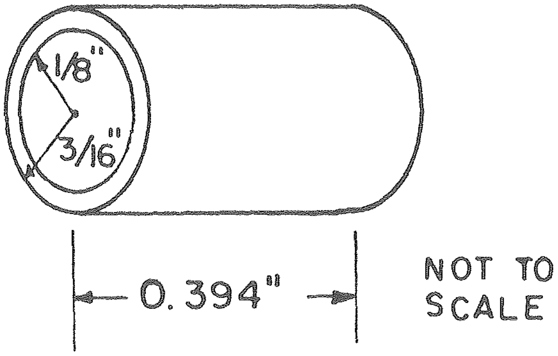

XBL 7512-9273

Fig. 4(c)

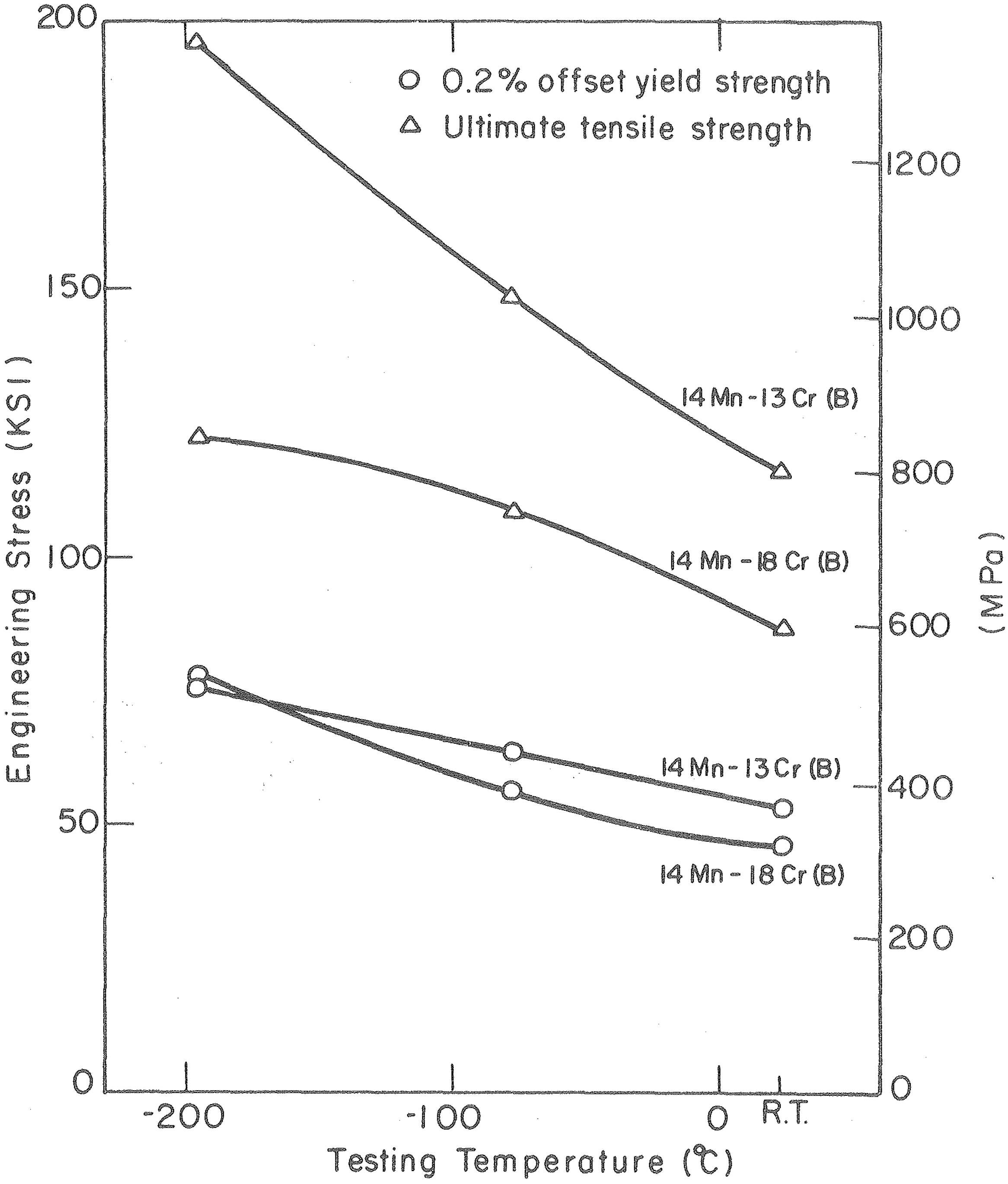

XBL 769-7505

Fig. 5.

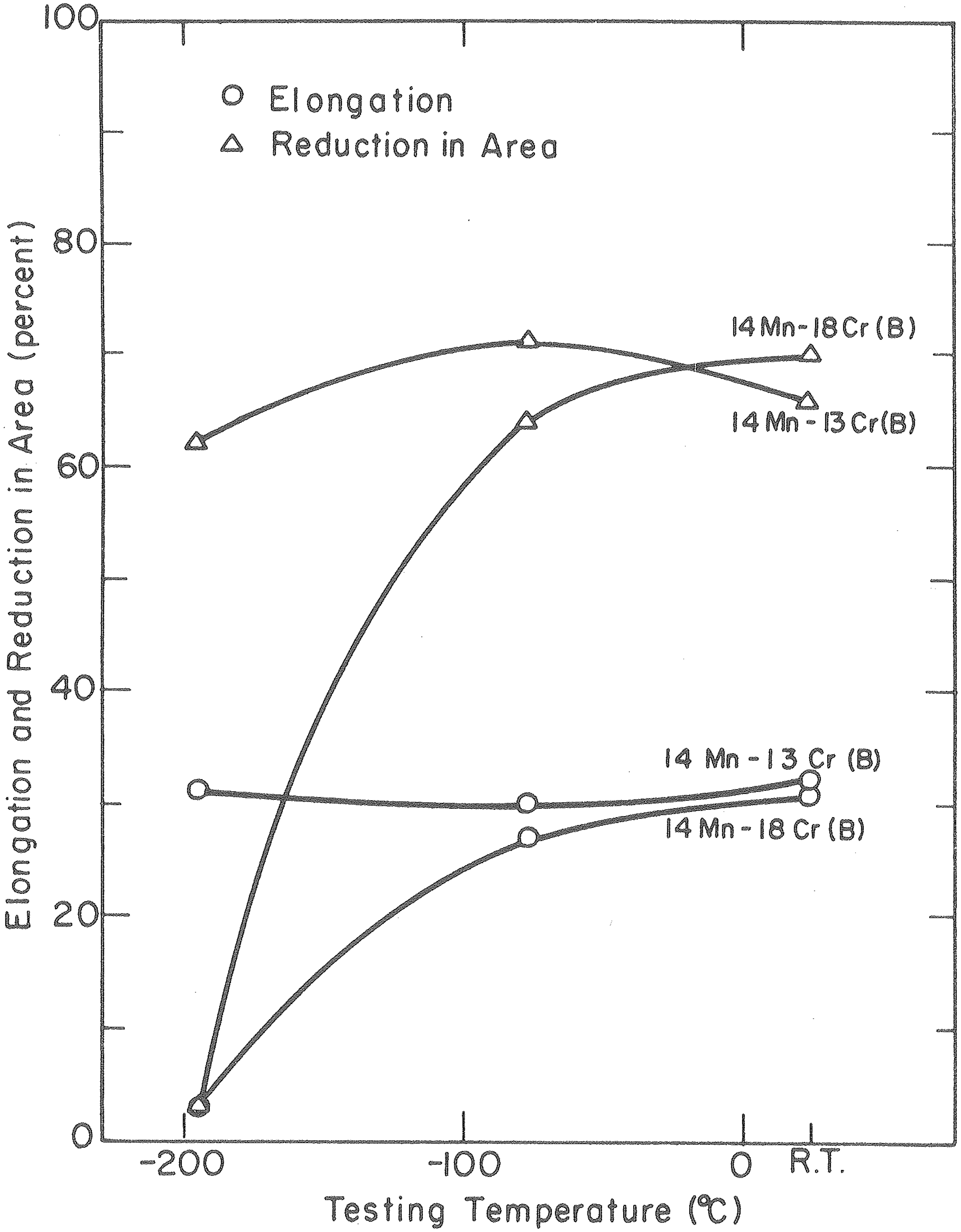

XBL 769-7504

Fig. 6.

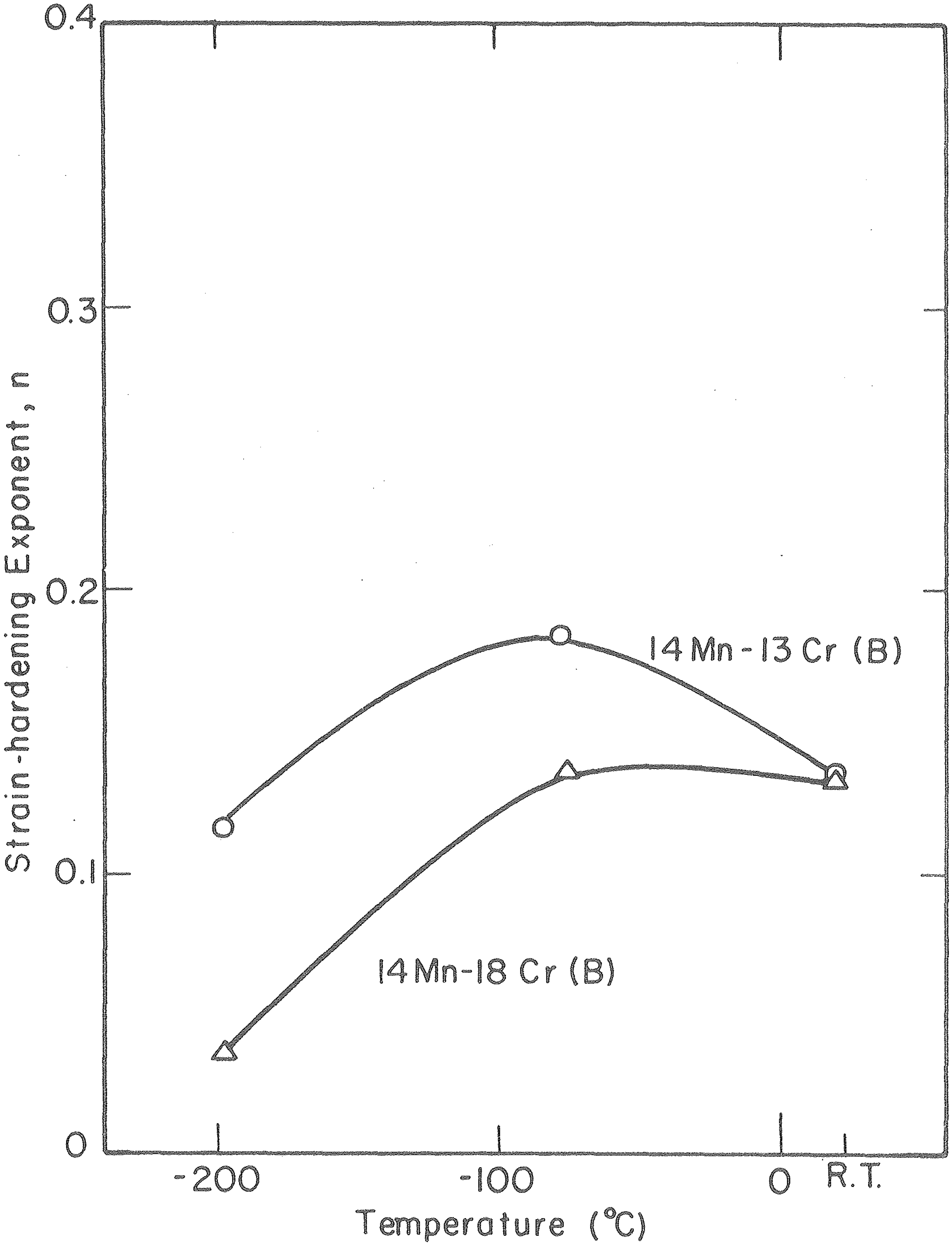

XBL 769-7577

Fig. 7.

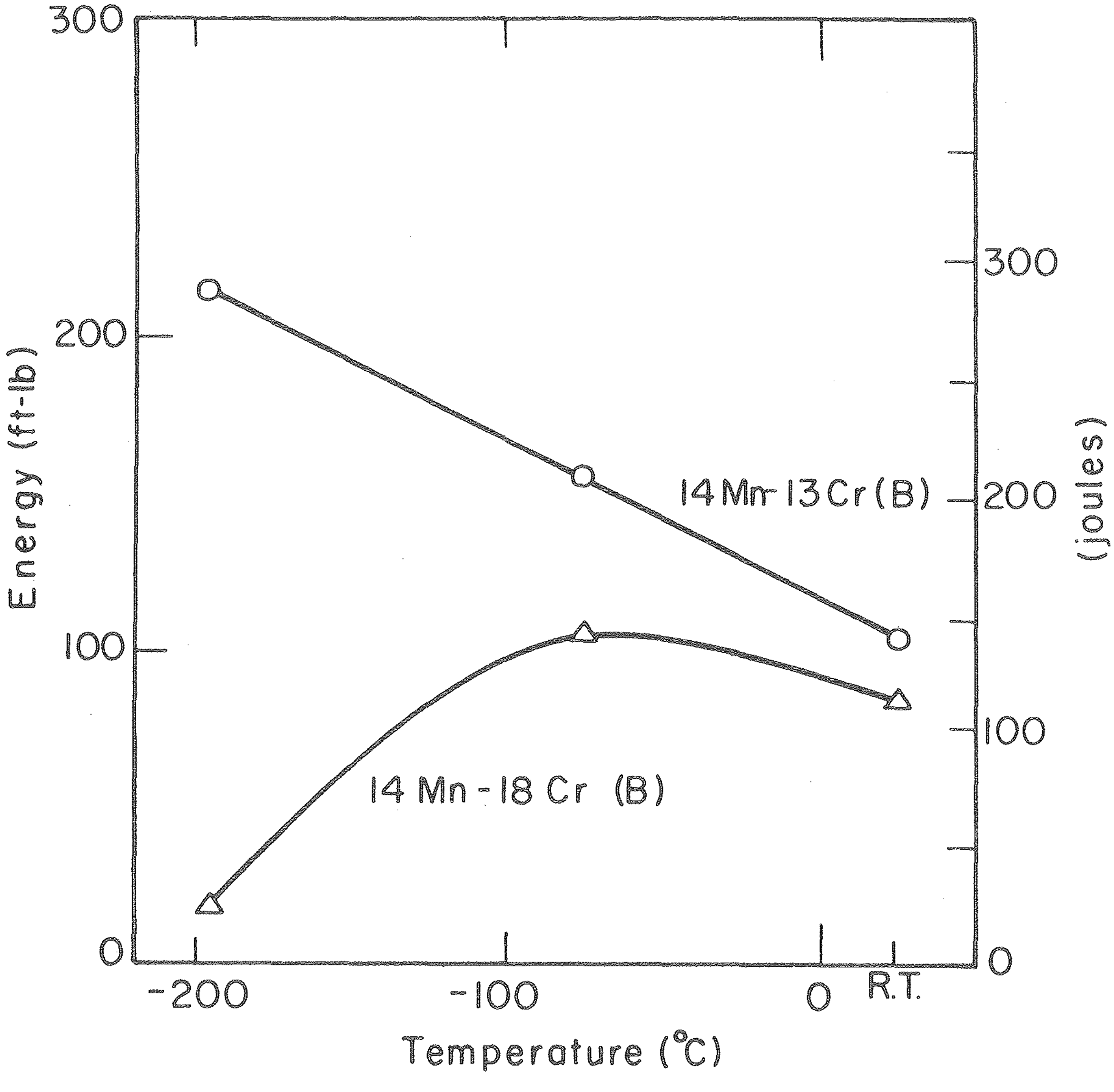

XBL 769-7578

Fig. 8.

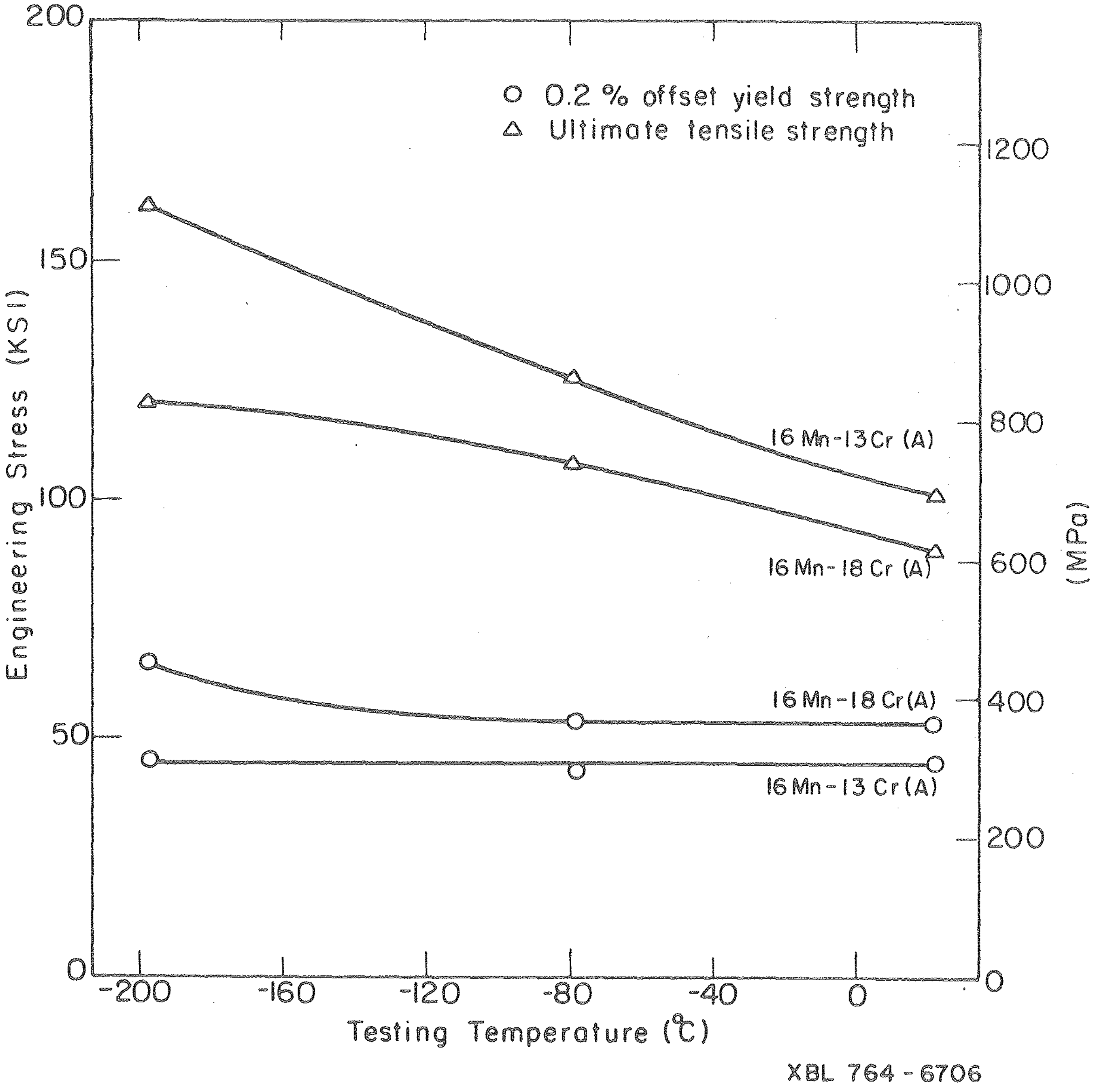
○ 0.2 % offset yield strength
△ Ultimate tensile strength
16 Mn-13 Cr (A)
16 Mn-18 Cr (A)
16 Mn-18 Cr(A)
16 Mn-13 Cr(A)
Engineering Stress (KSI)
(MPa)
Testing Temperature (°C)
200
150
100
50
0
1200
1000
800
600
400
200
0
-200
-160
-120
-80
-40
0
XBL 764-6706

Fig. 9.

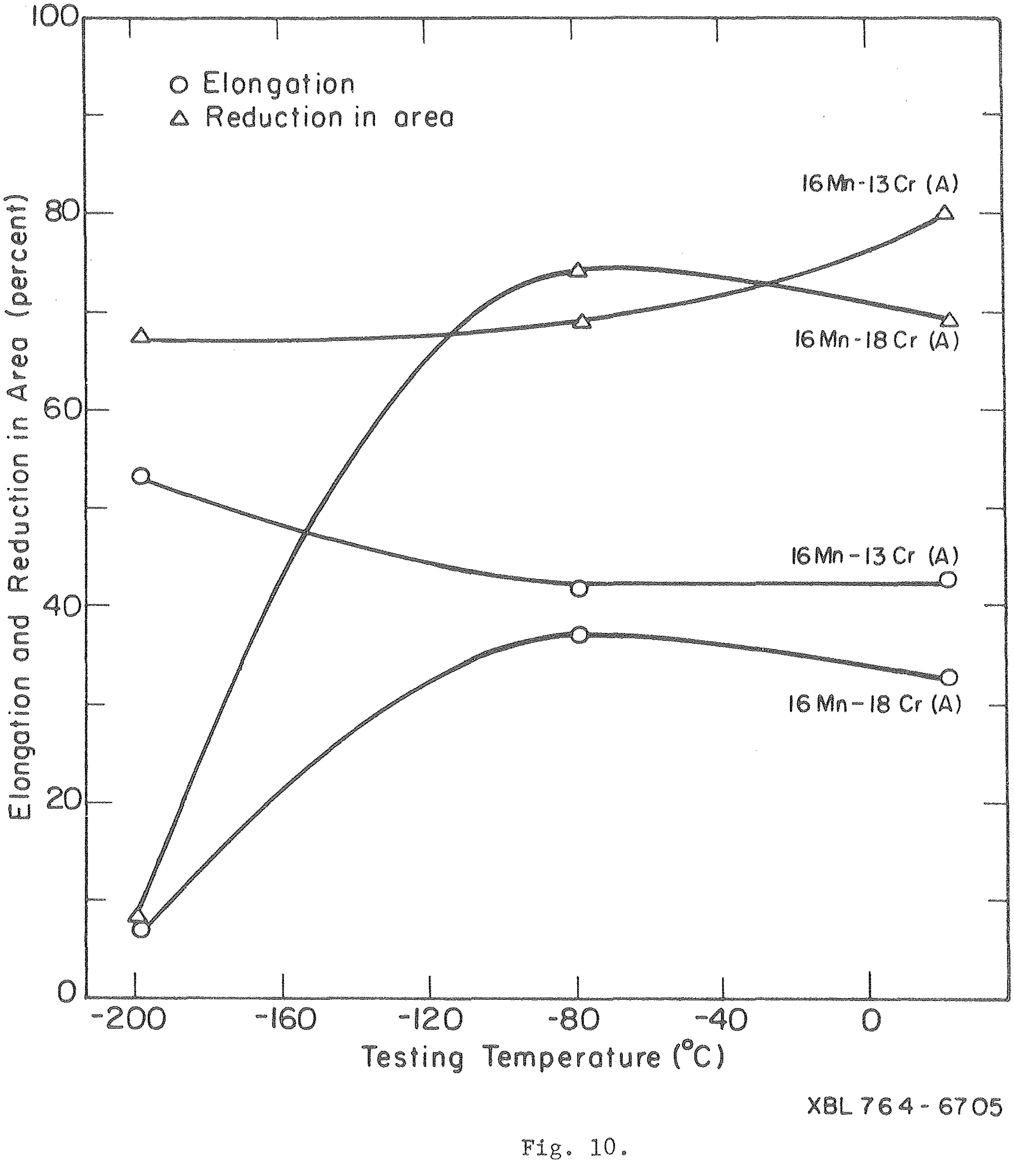

XBL 764-6705

Fig. 10.

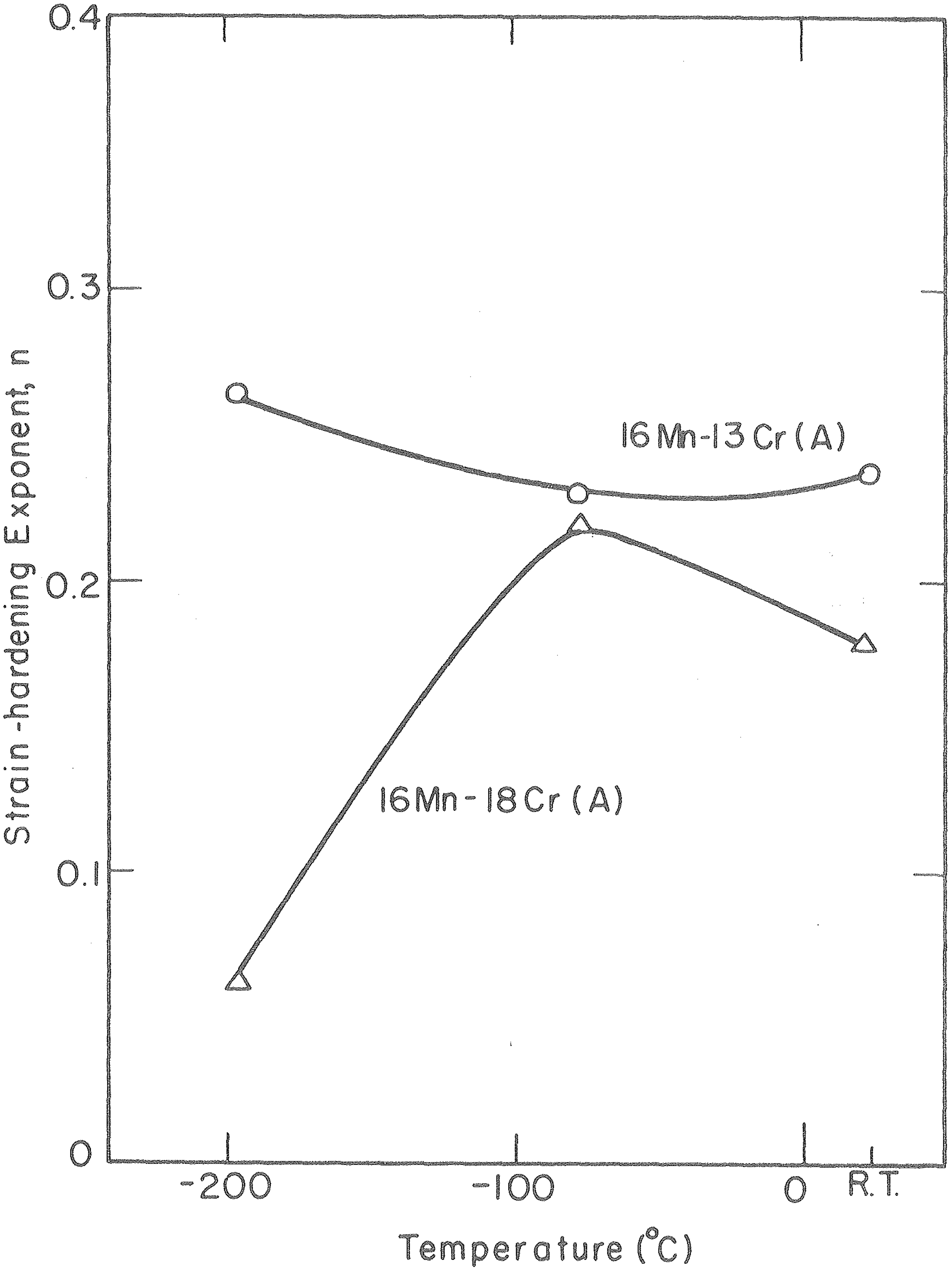

XBL769-7579

Fig. 11.

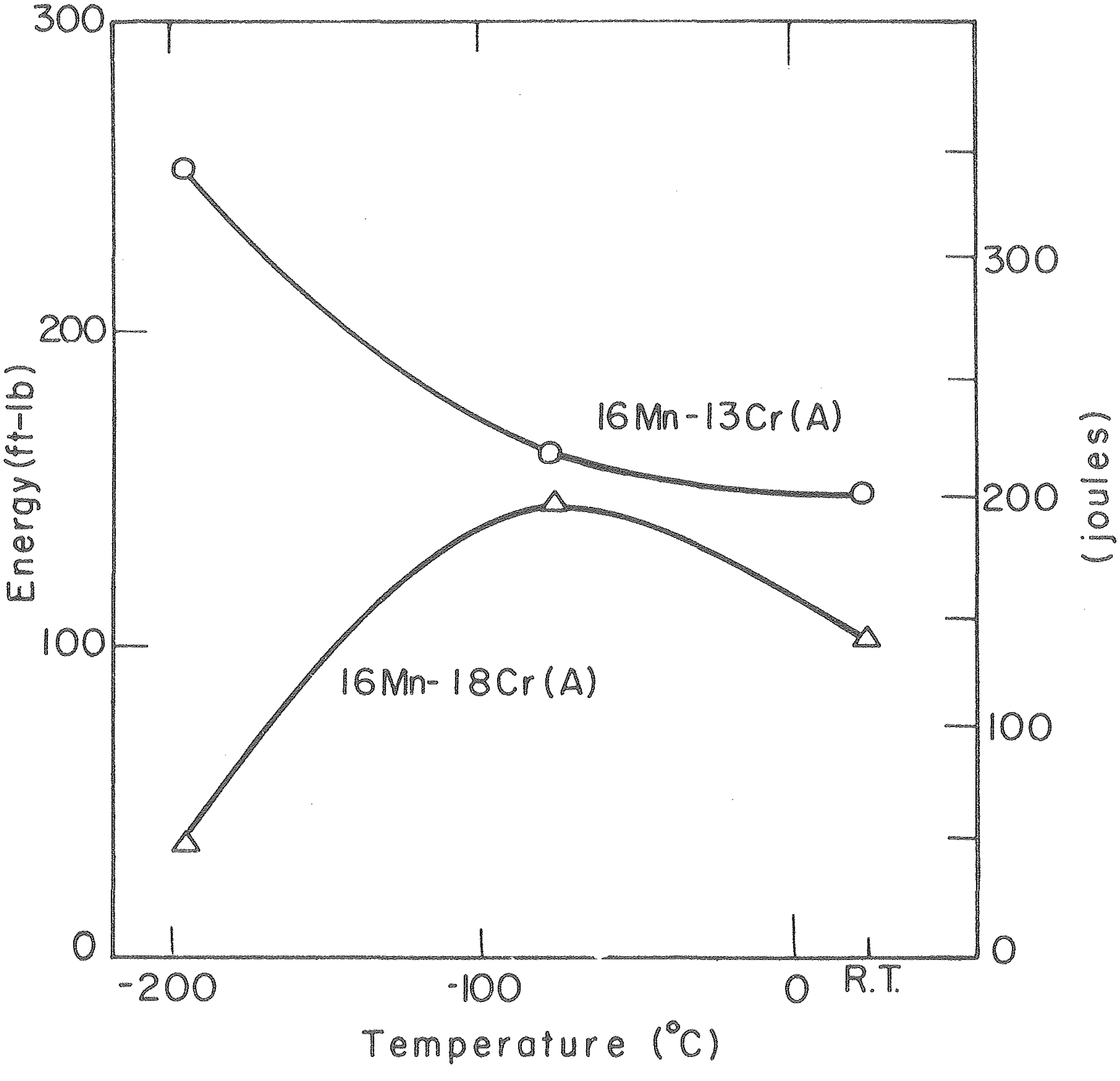

XBL 769-7580

Fig. 12.

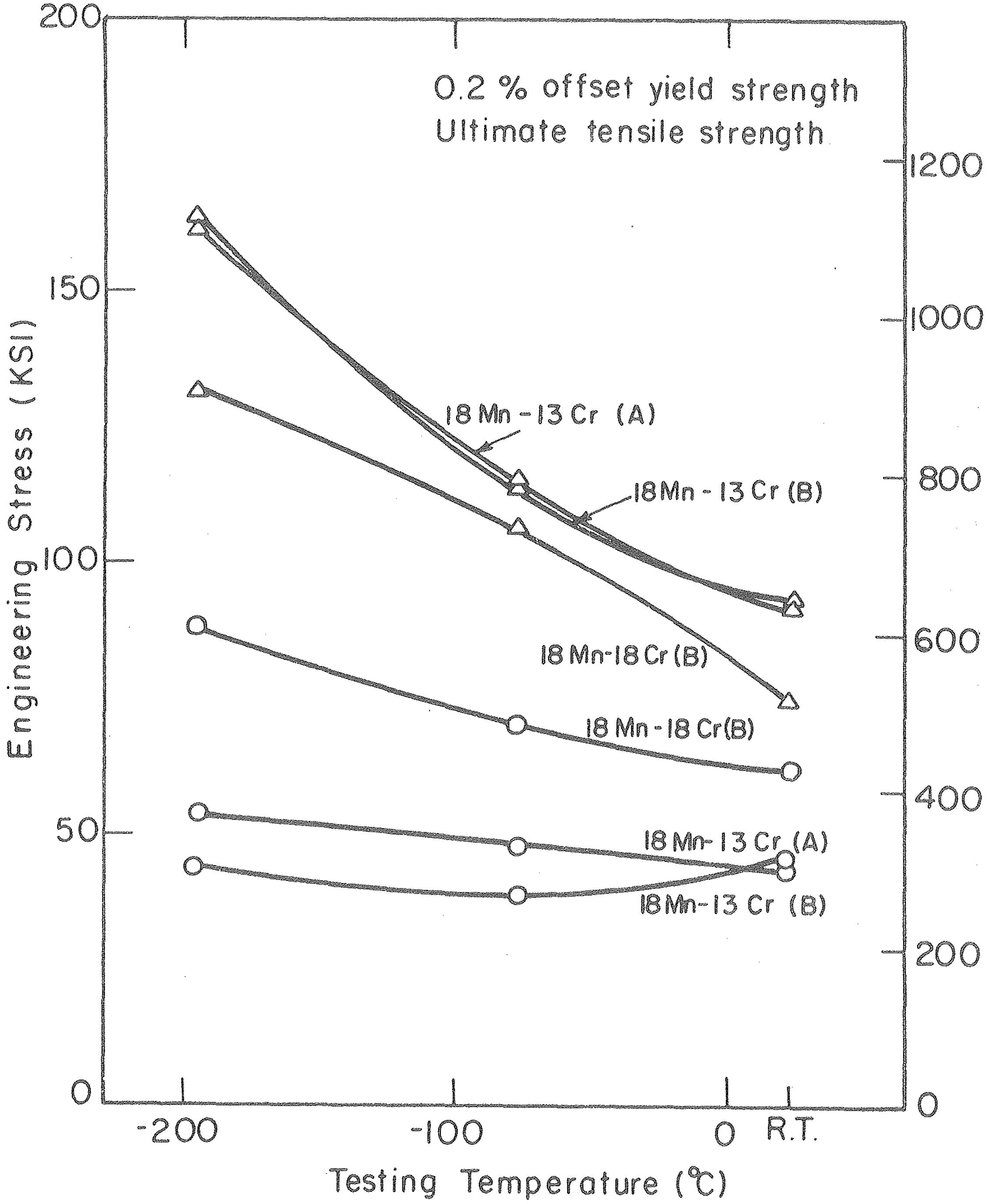

XBL 869-7503

Fig. 13.

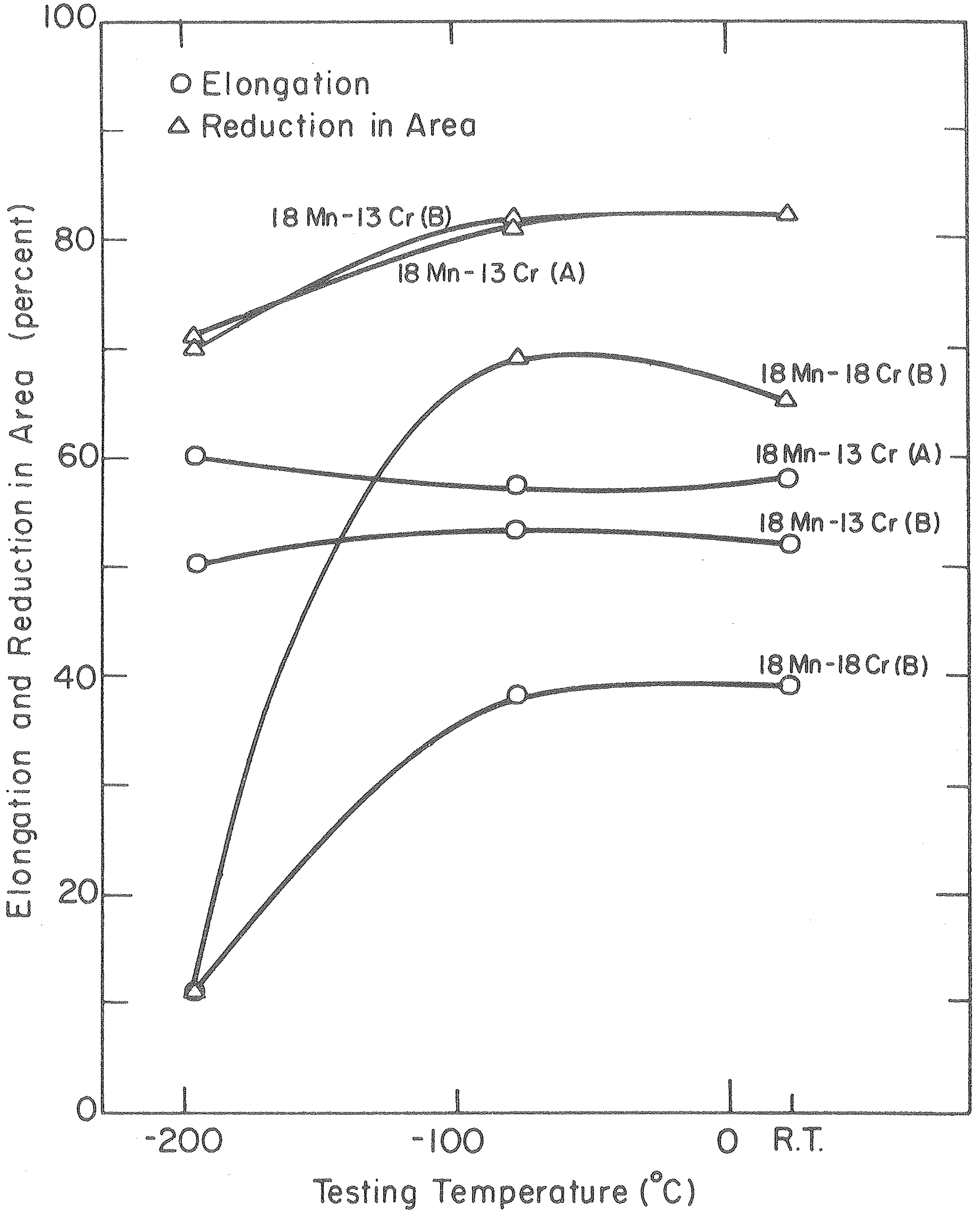

XBL 769-7502

Fig. 14.

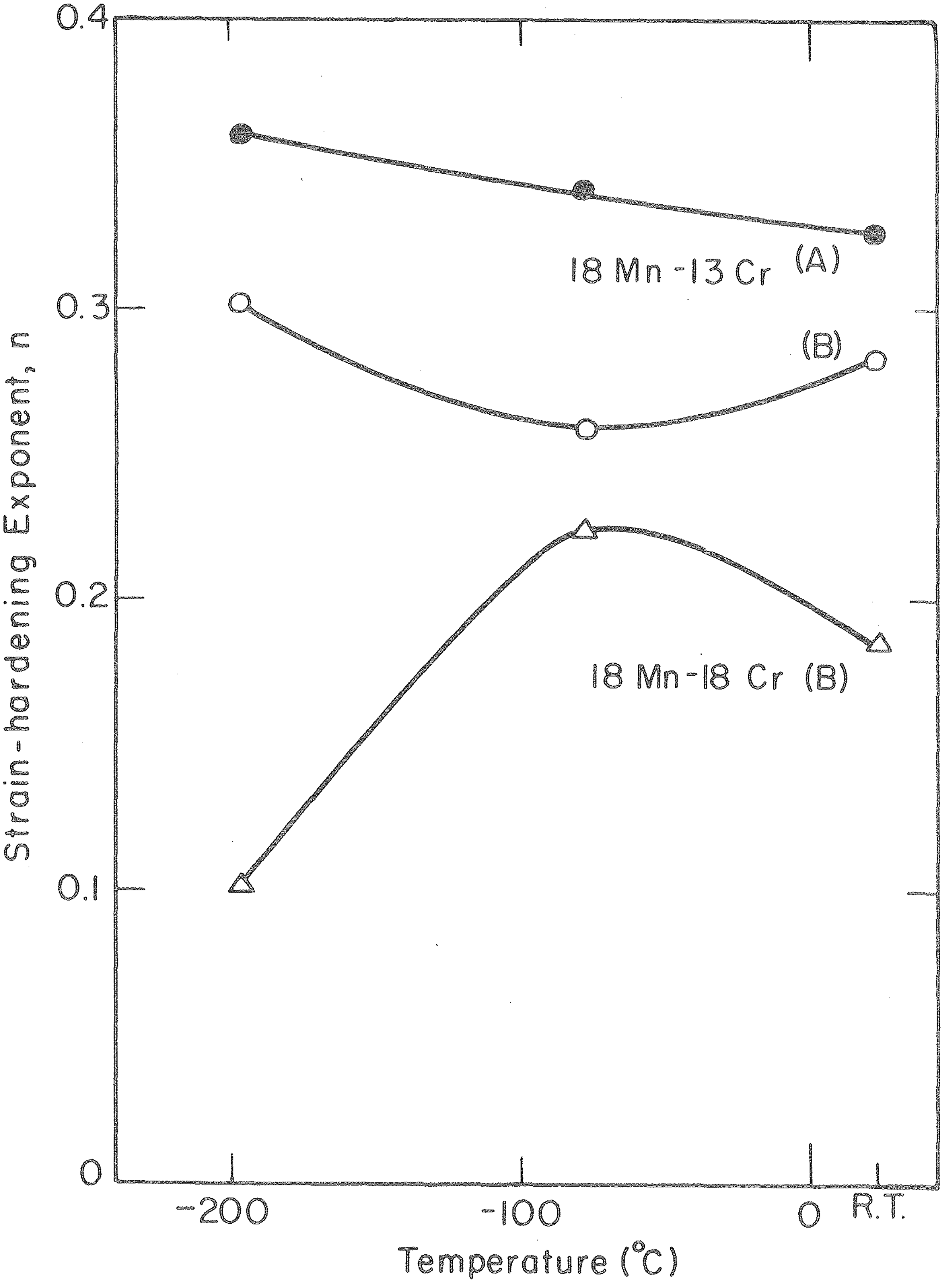

XBL 769-7575

Fig. 15.

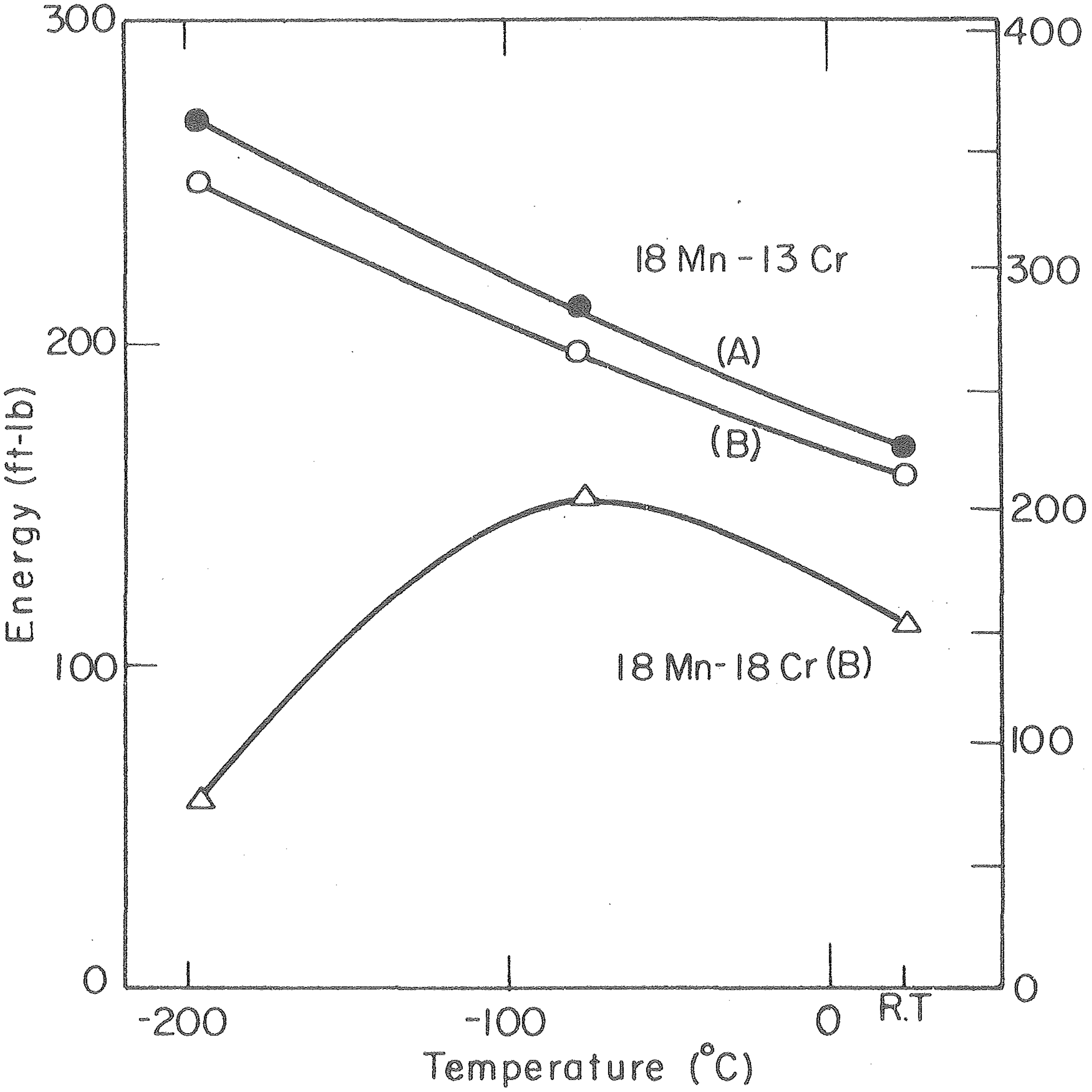

XBL 769-7576

Fig. 16.

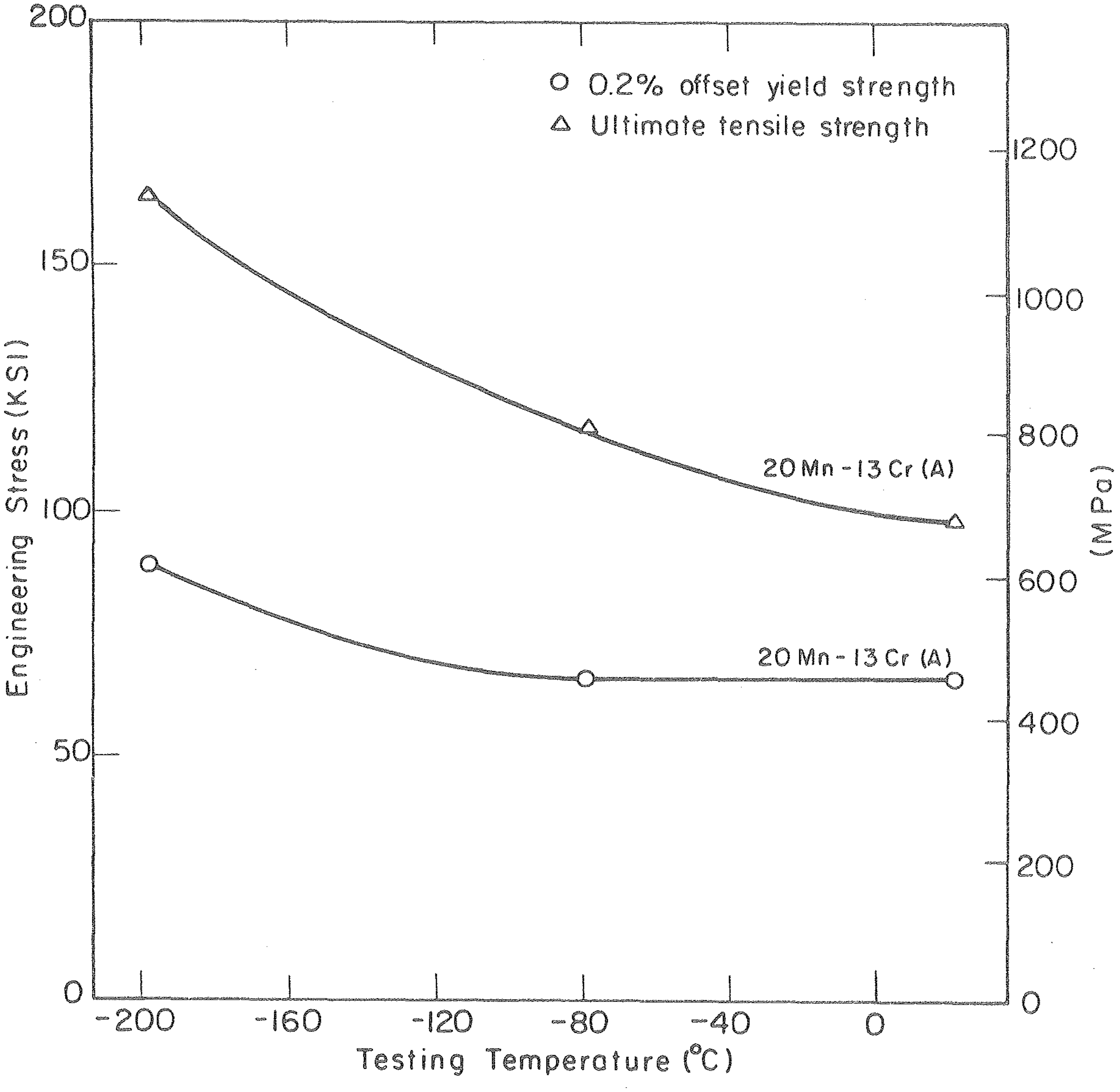

XBL 764-6708

Fig. 17.

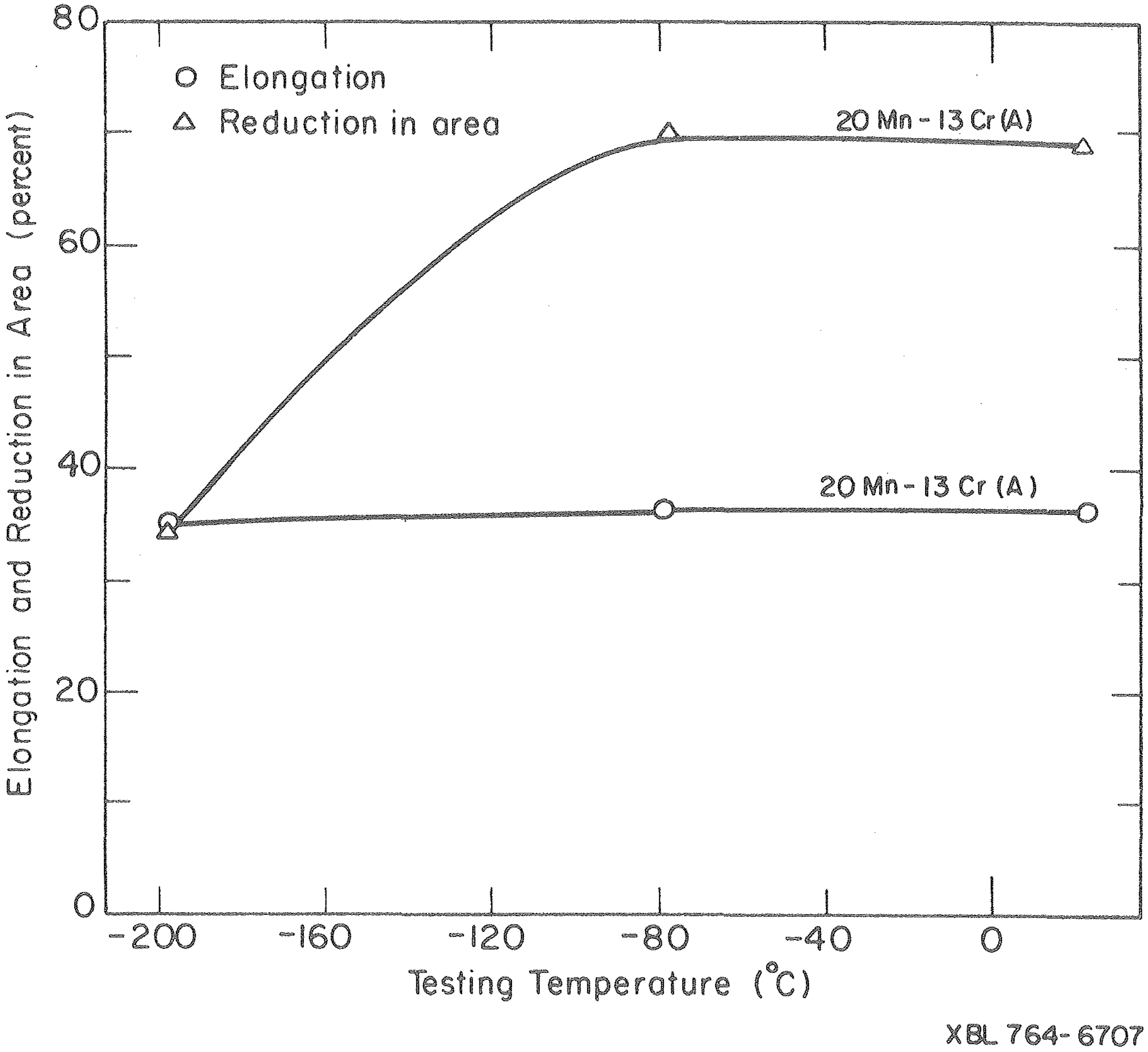
○ Elongation
△ Reduction in area
20 Mn - 13 Cr (A)
20 Mn - 13 Cr (A)
Elongation and Reduction in Area (percent)
Testing Temperature (°C)
0
20
40
60
80
-200
-160
-120
-80
-40
0
XBL 764-6707

Fig. 18.

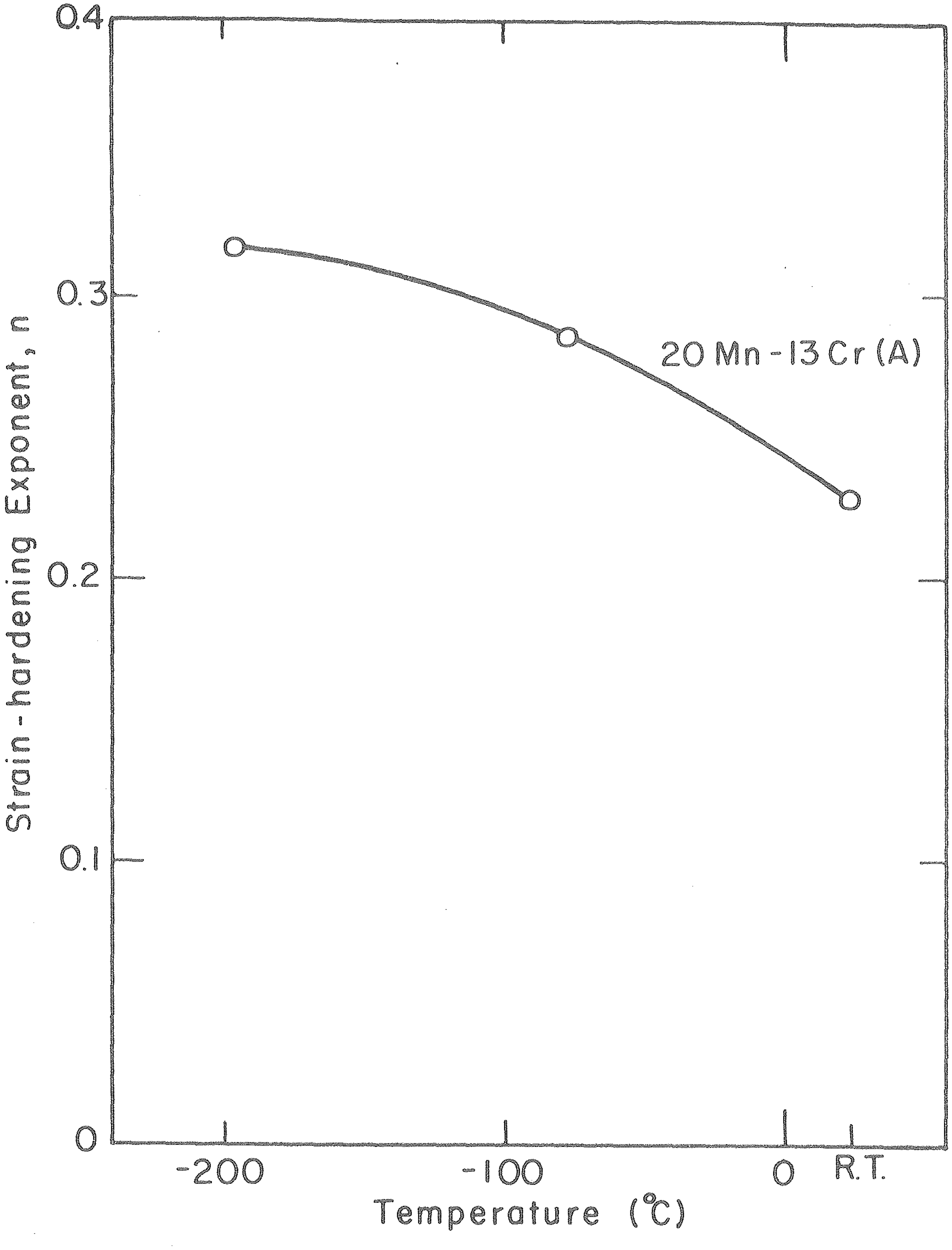

XBL 769-7573

Fig. 19.

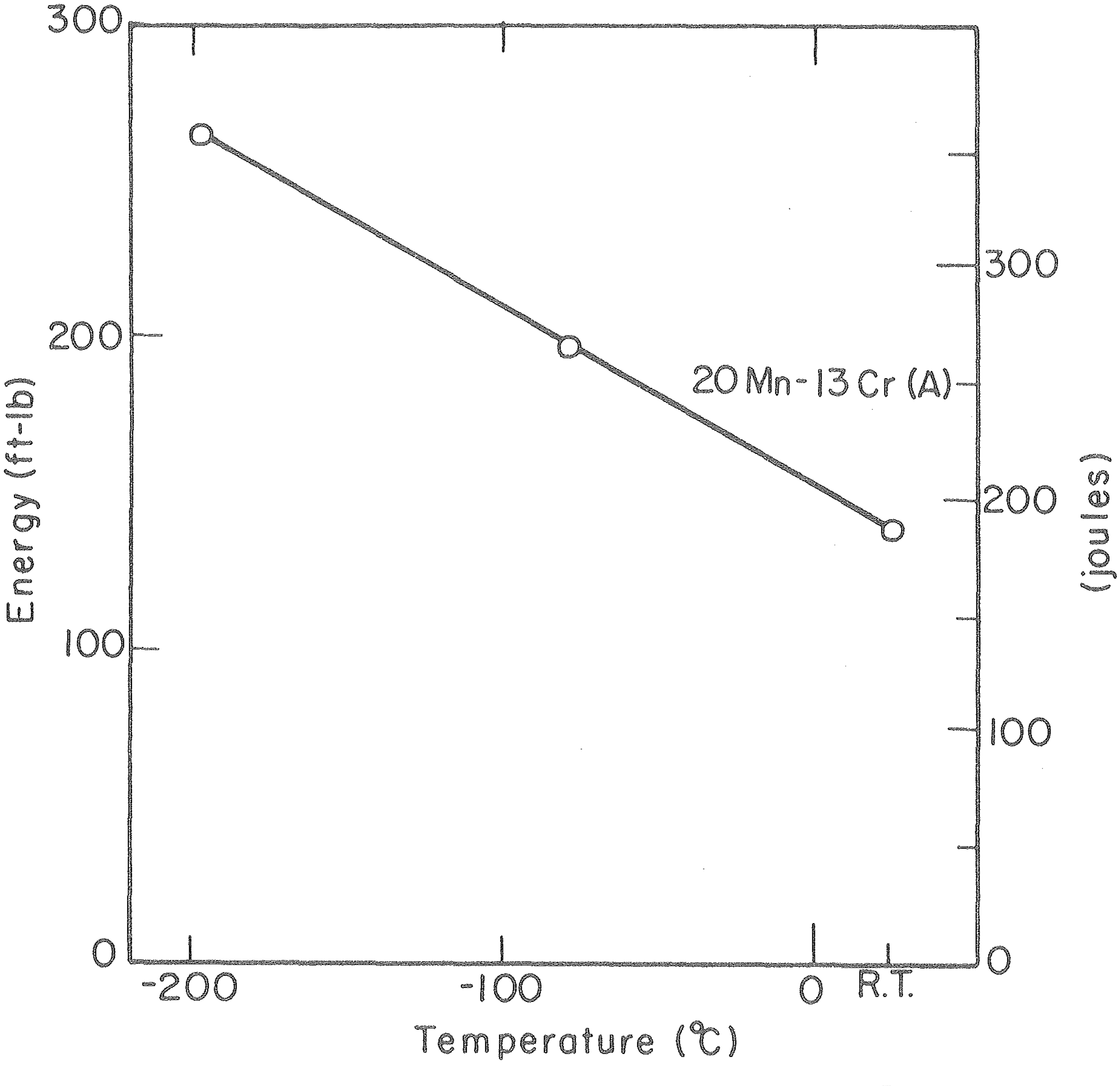

XBL 769-7574

Fig. 20.

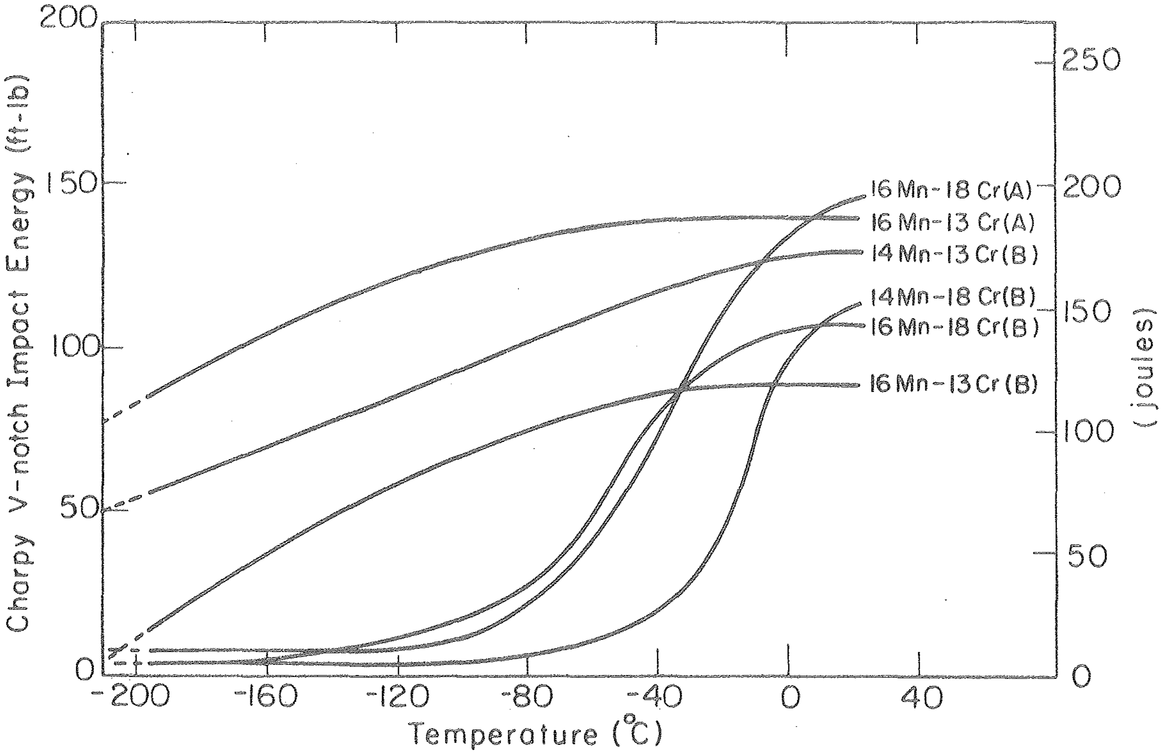

XBL 764-6693

Fig. 21.

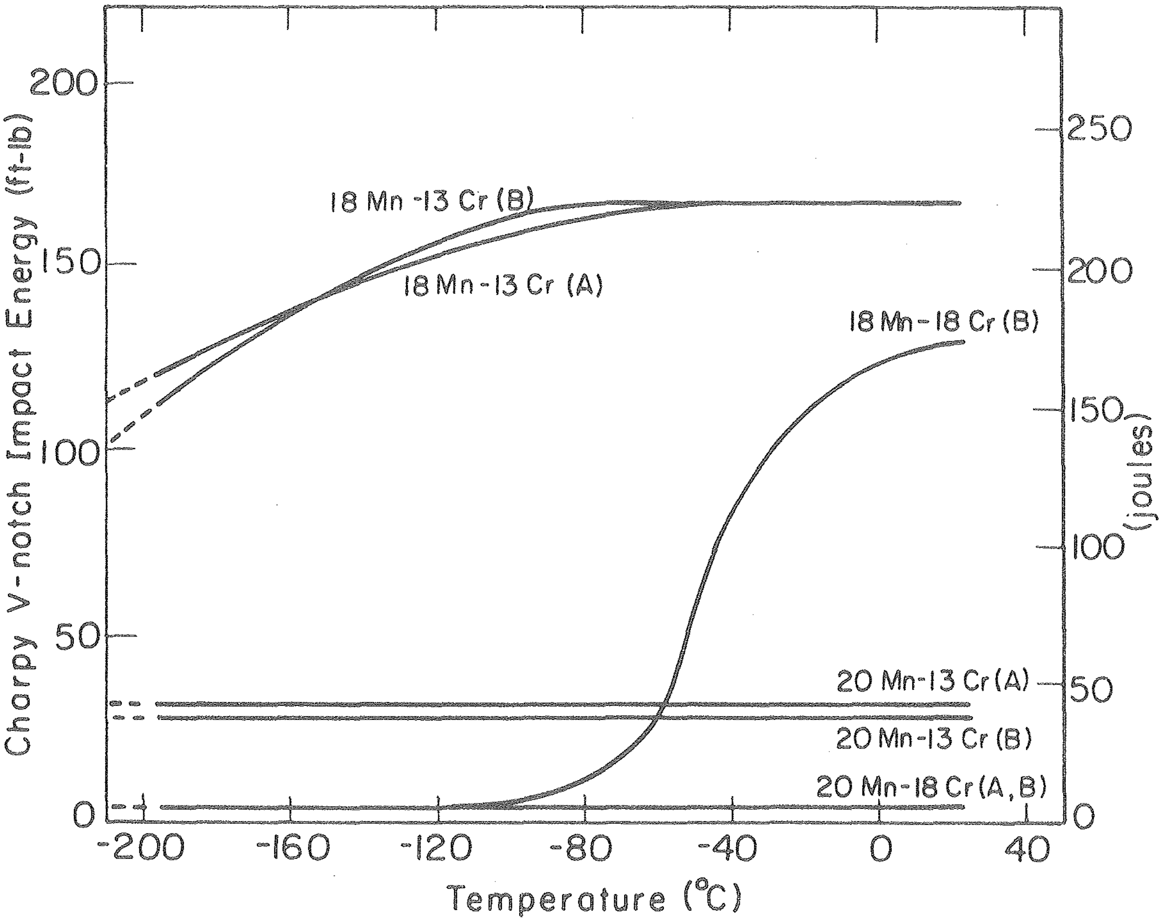

XBL 764-6694

Fig. 22.

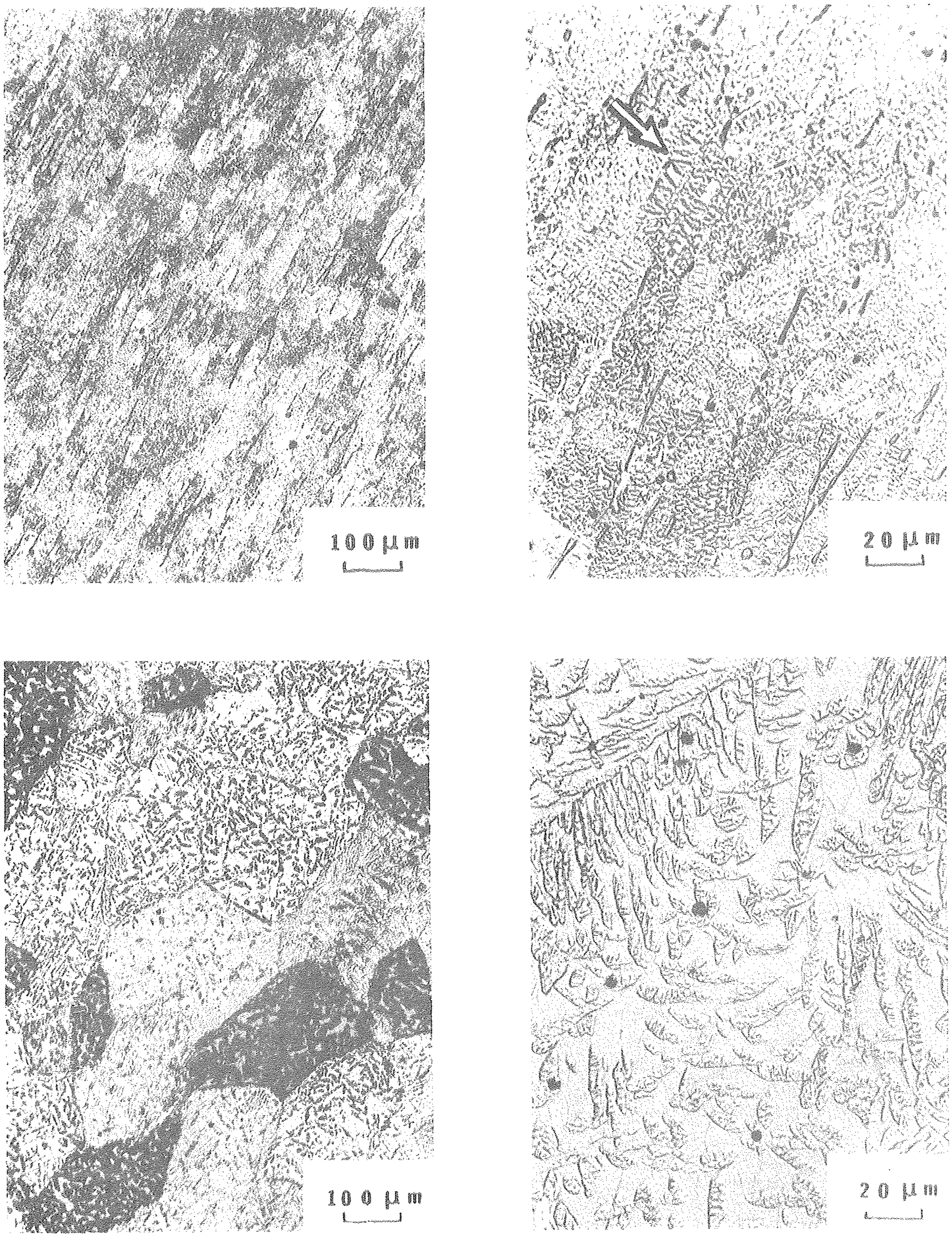

CBB 768-7772

Fig. 23.

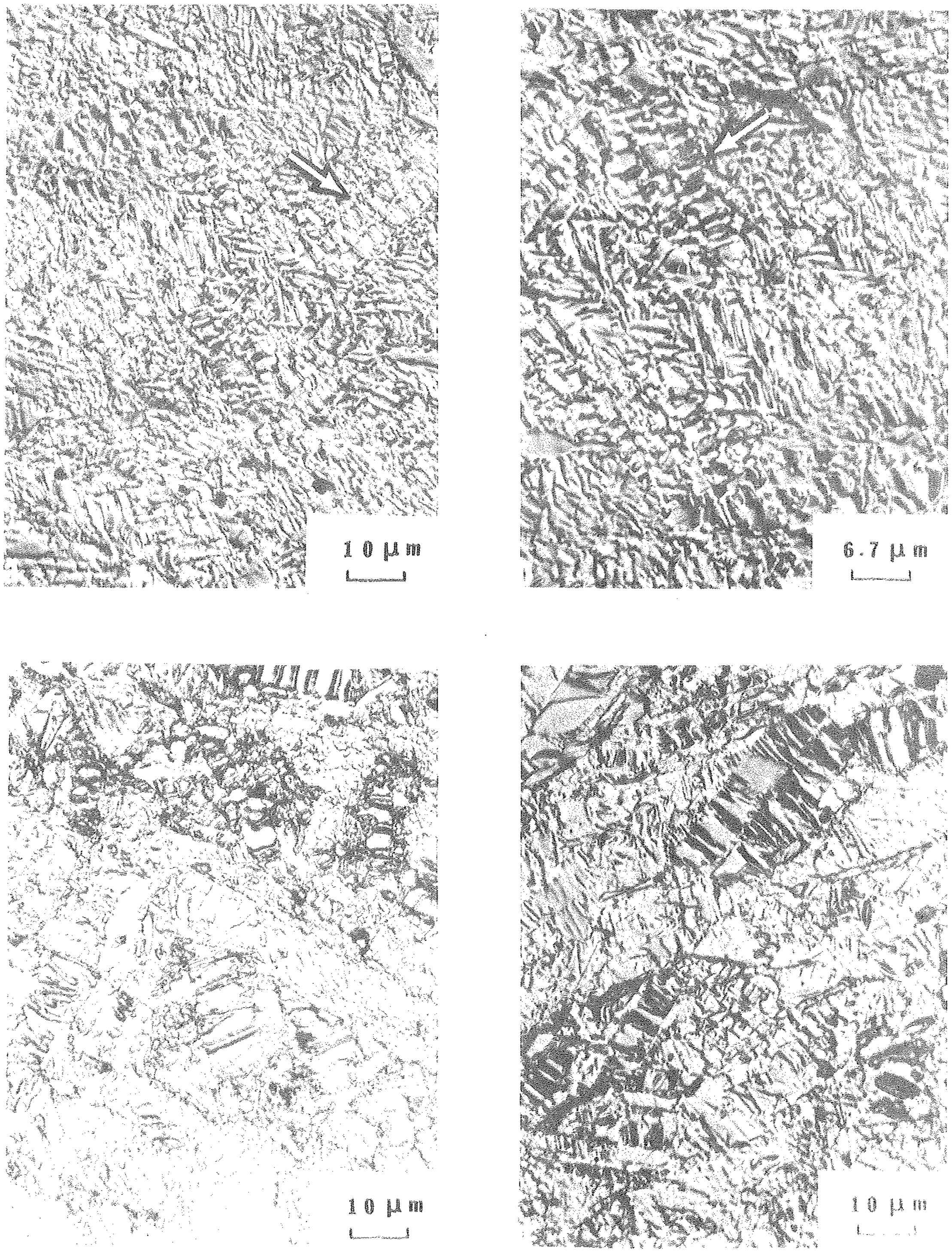

XBB 758-7774

Fig. 24.

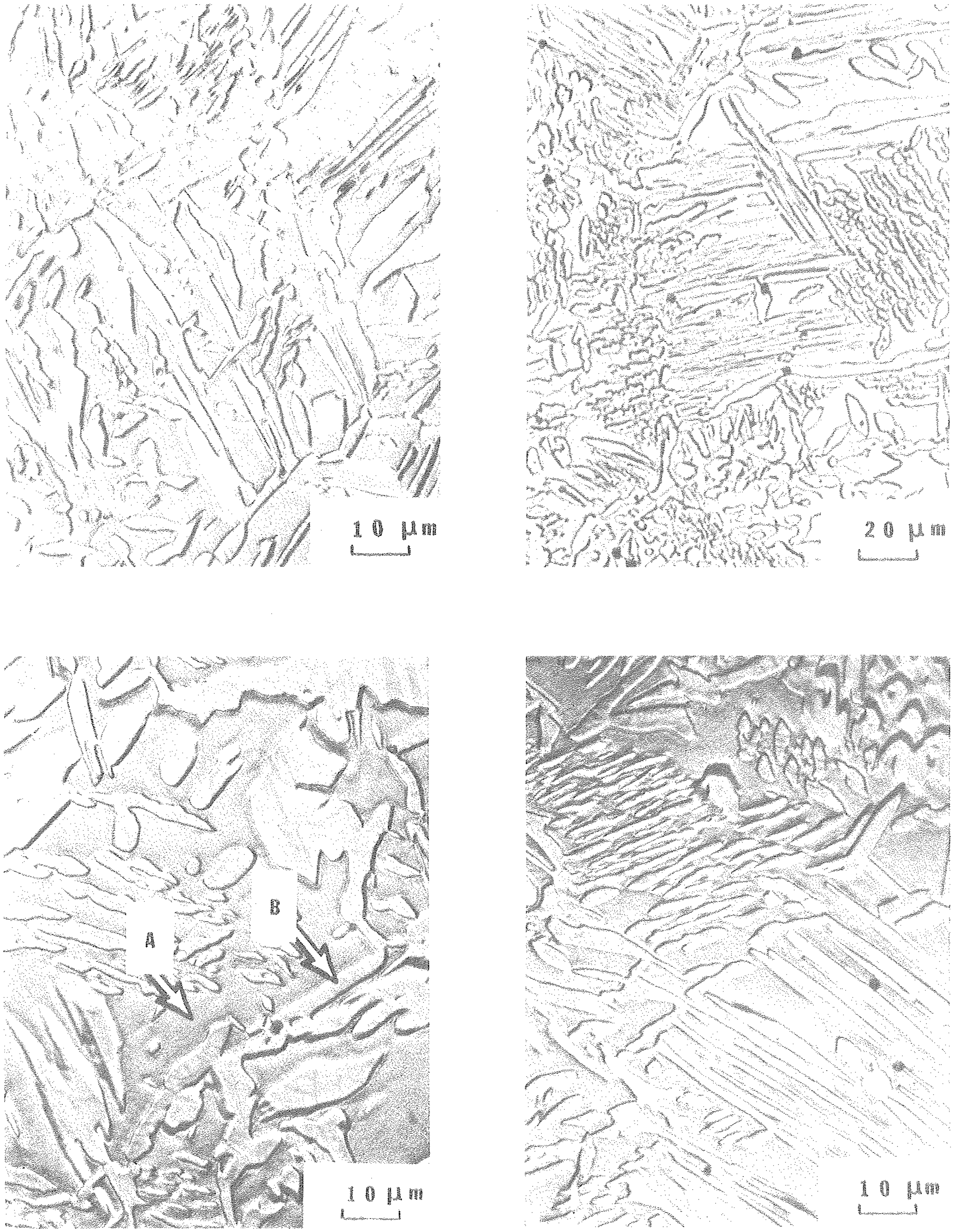

XBB 768-7771

Fig. 25.

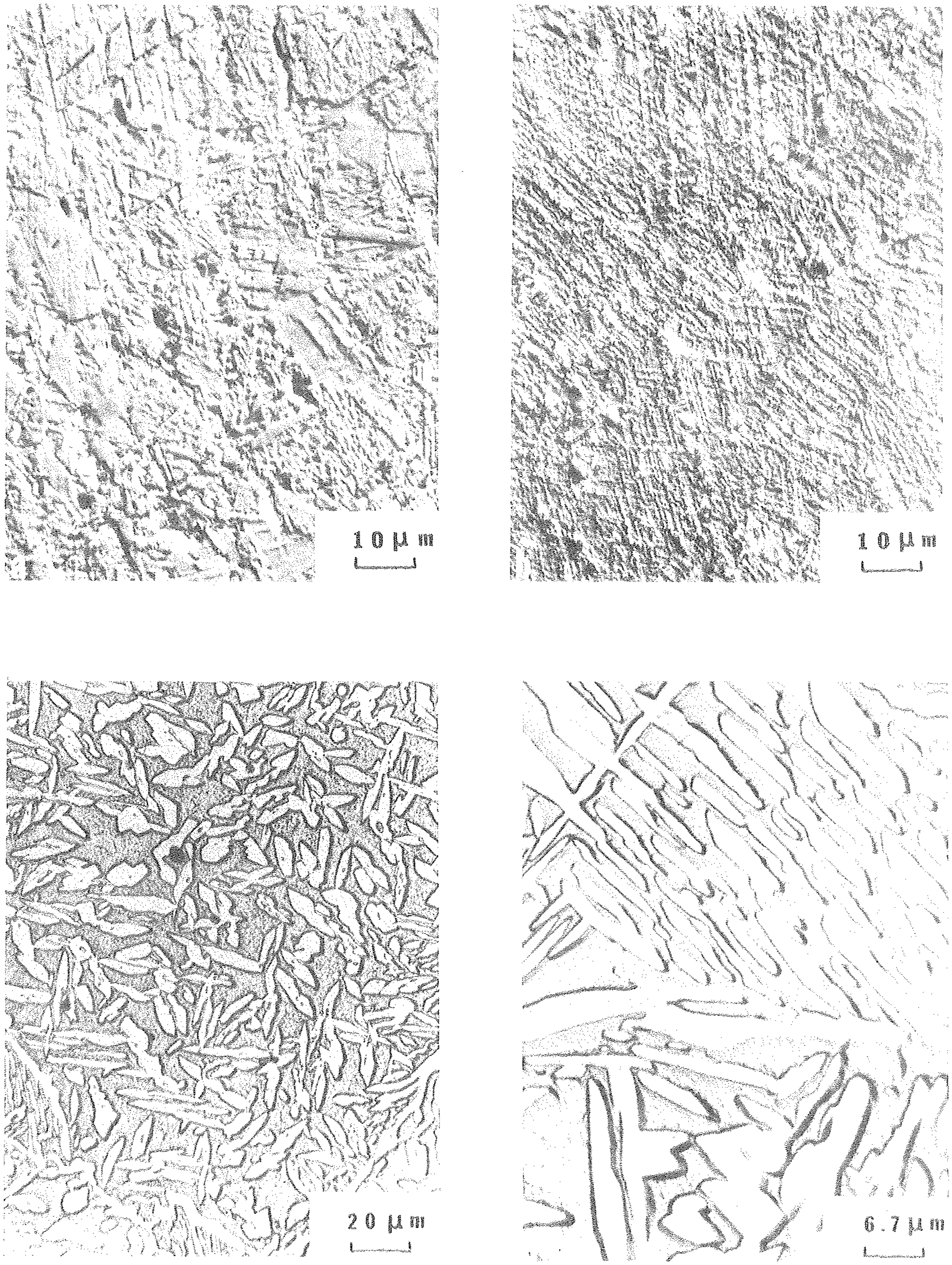

XBB 768-7769

Fig. 26.

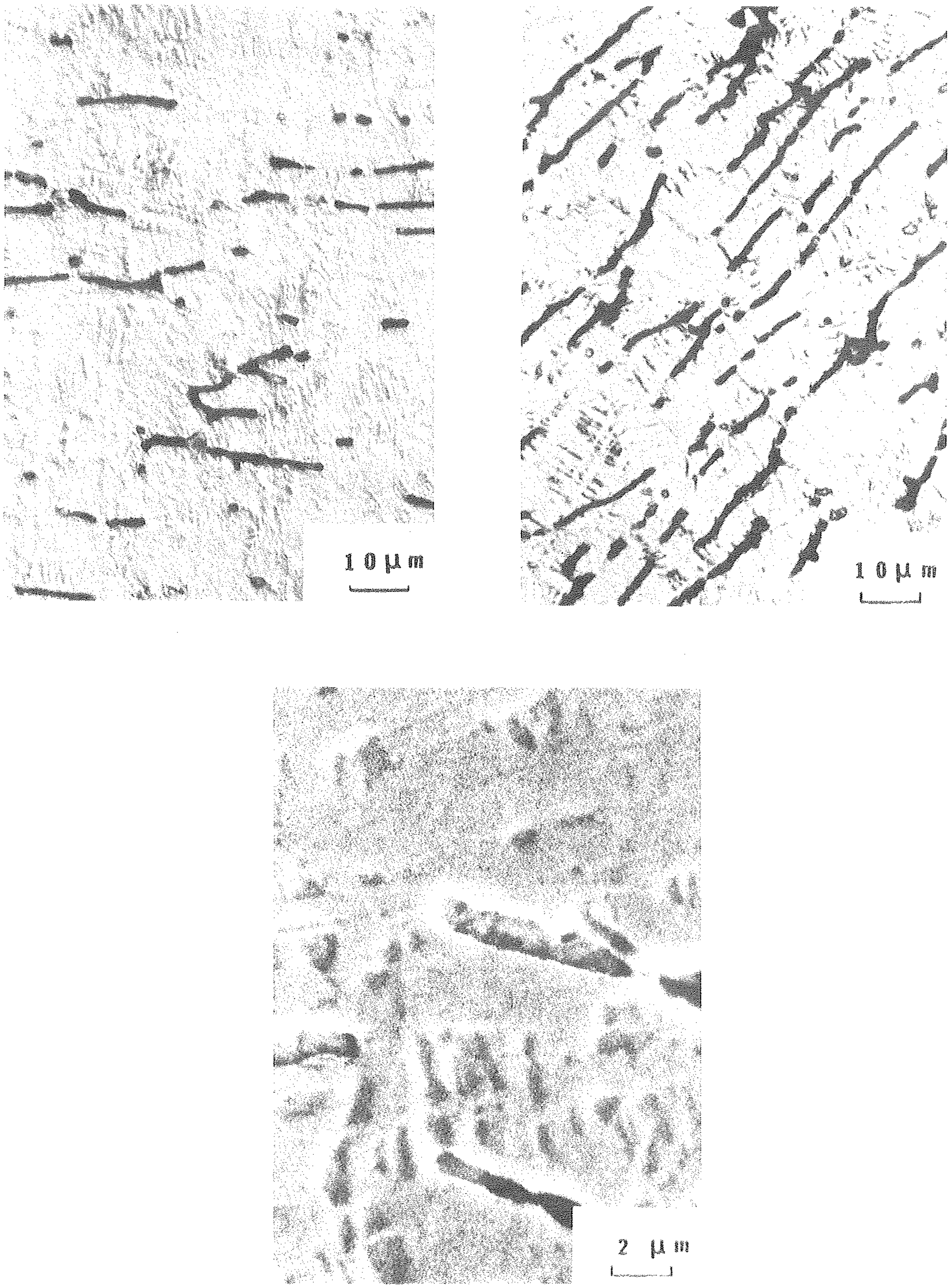

XBB 768-7760

Fig. 27.

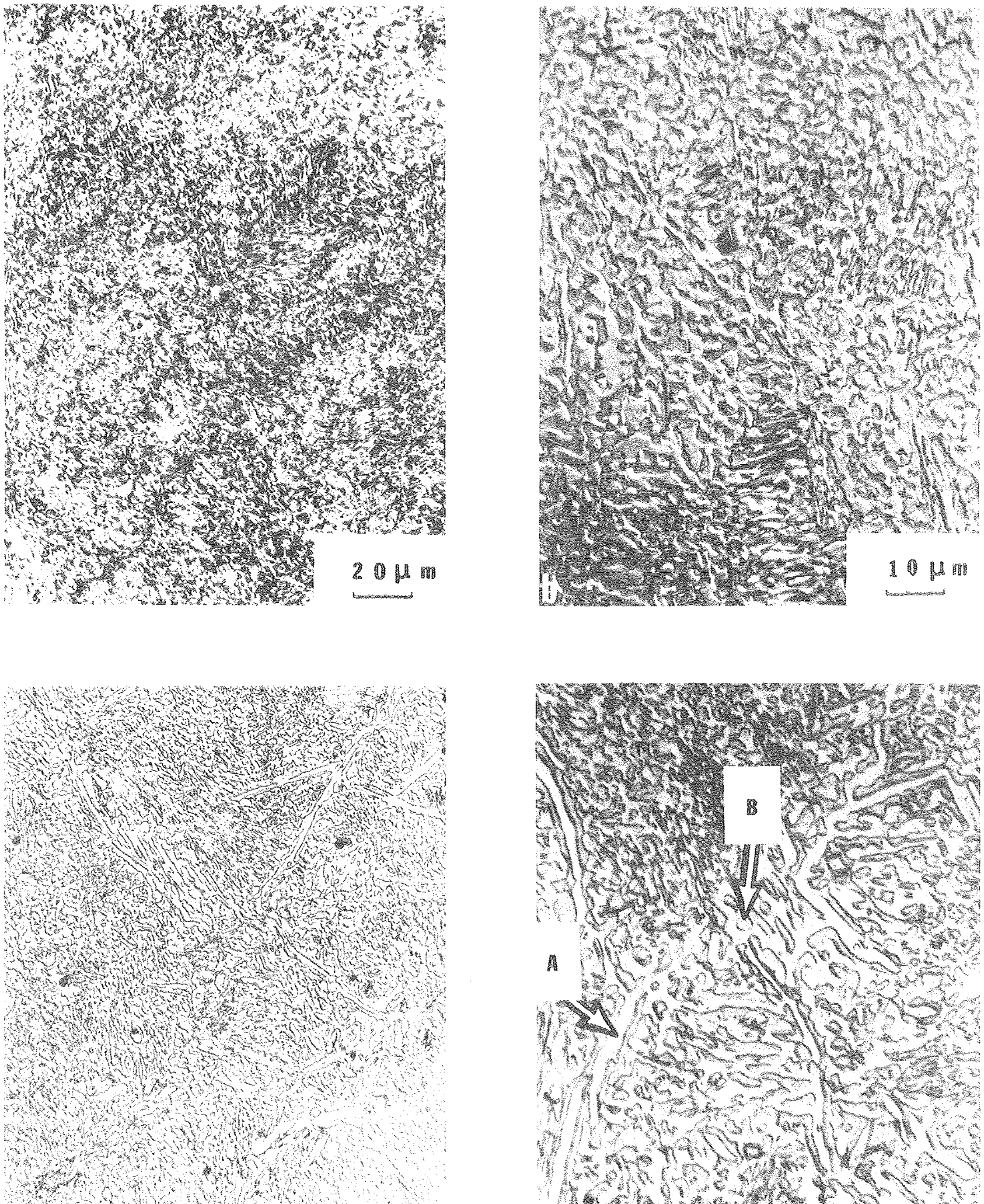

XBB 768-7773

Fig. 28.

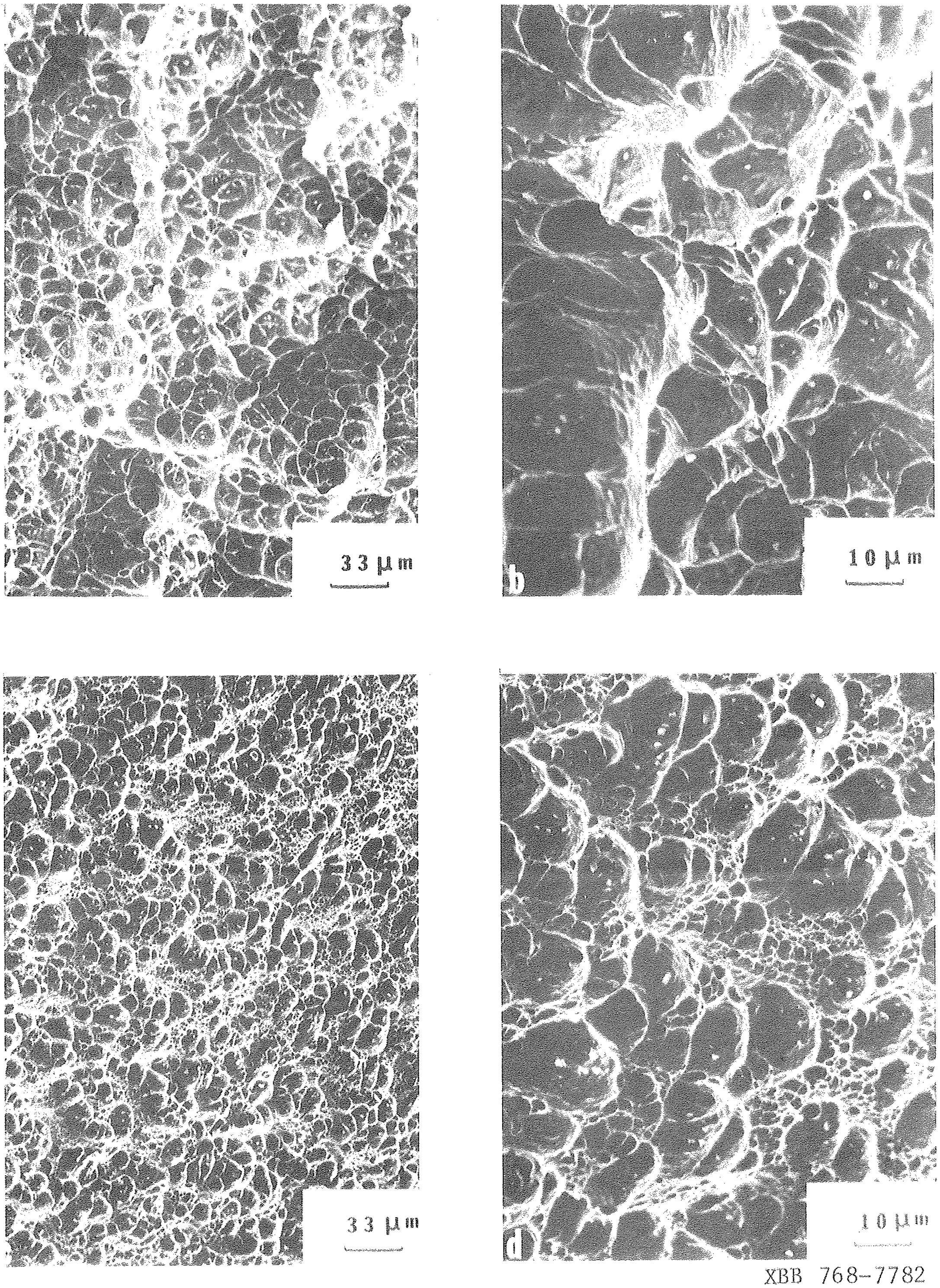

XBB 768-7782

Fig. 29.

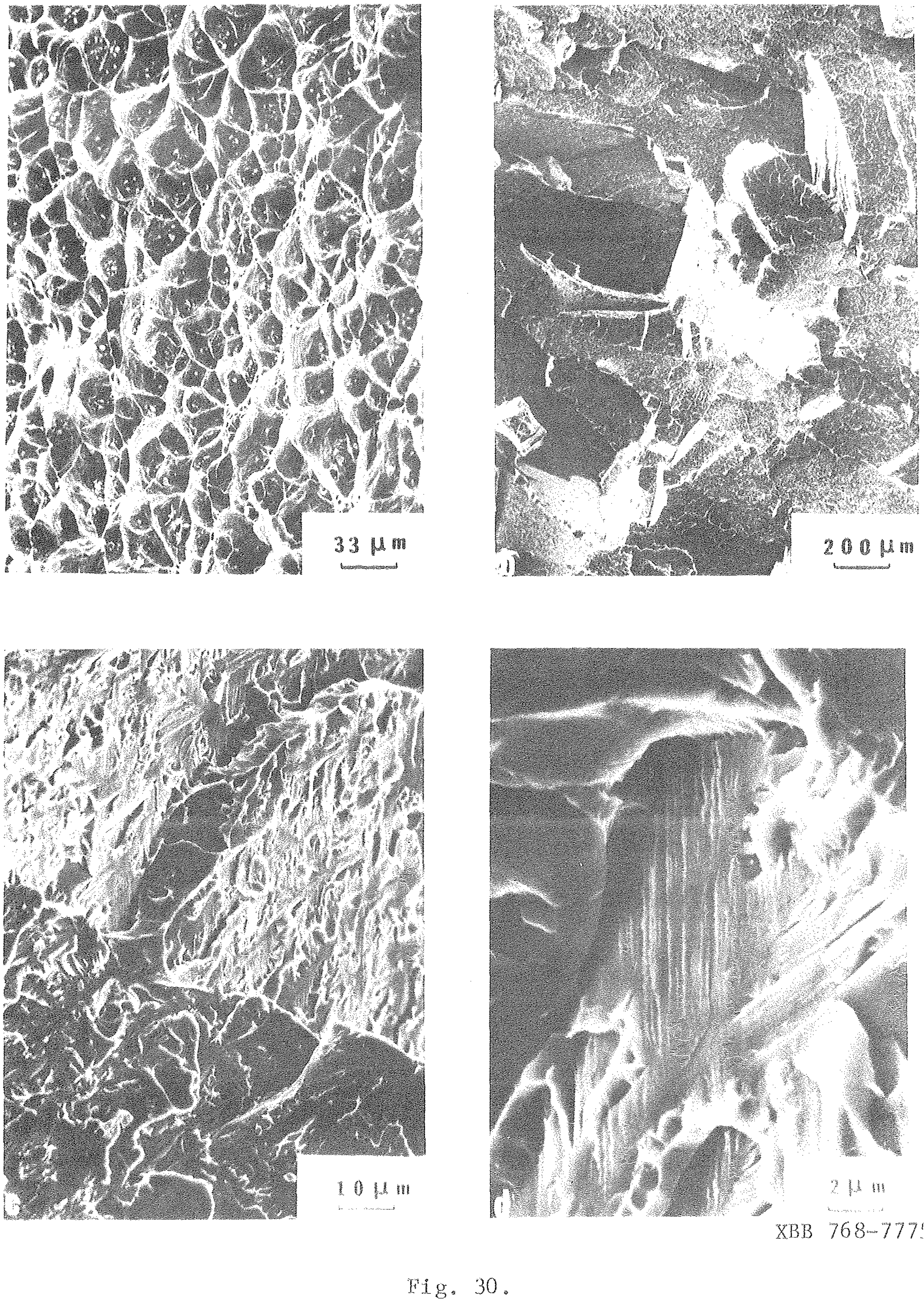

XBB 768-7775

Fig. 30.

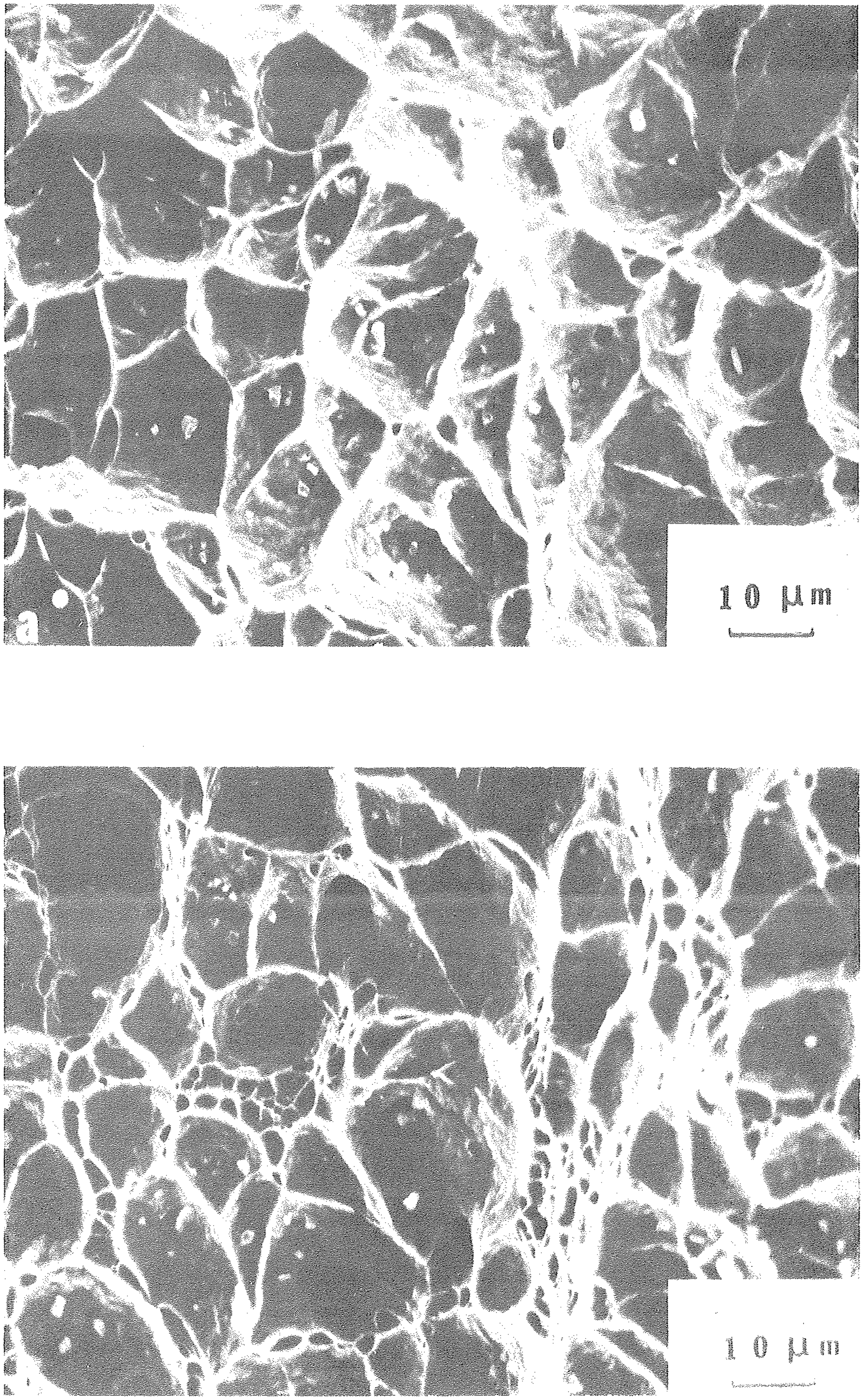

CBB 768-7754

Fig. 31.

CBB 768-7757

Fig. 32.

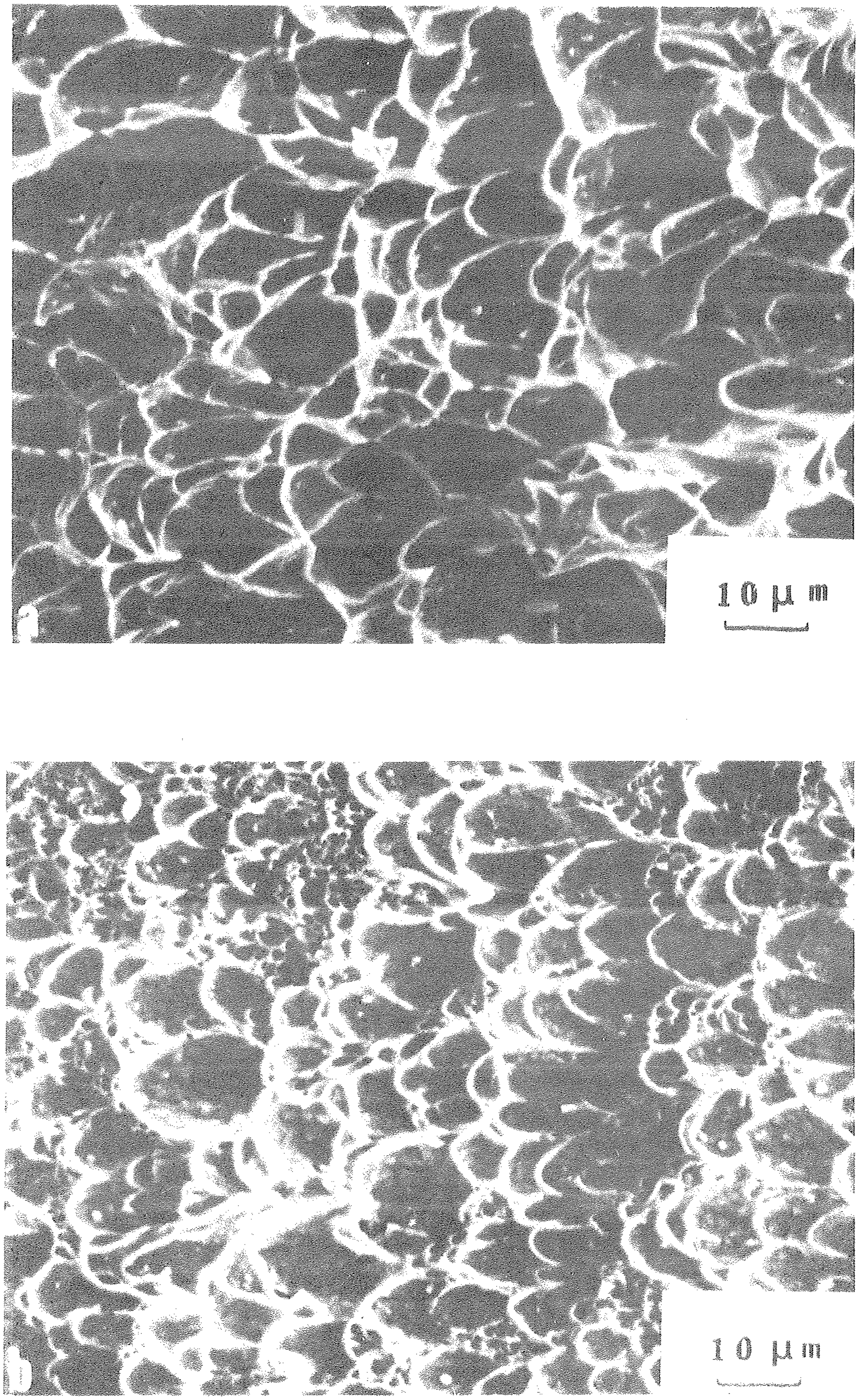

XBB 768-7751

Fig. 33.

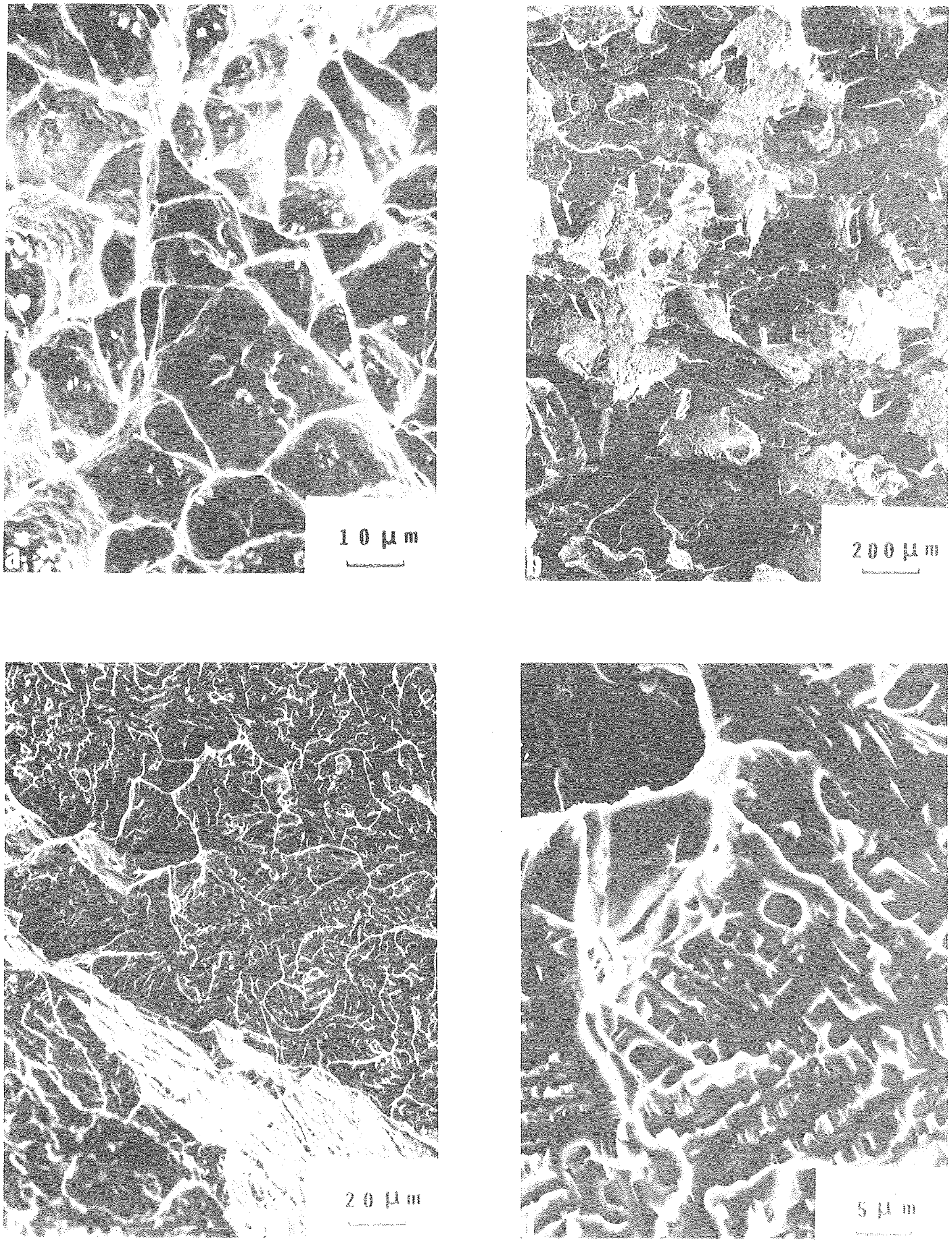

XBB 768-7777

Fig. 34.

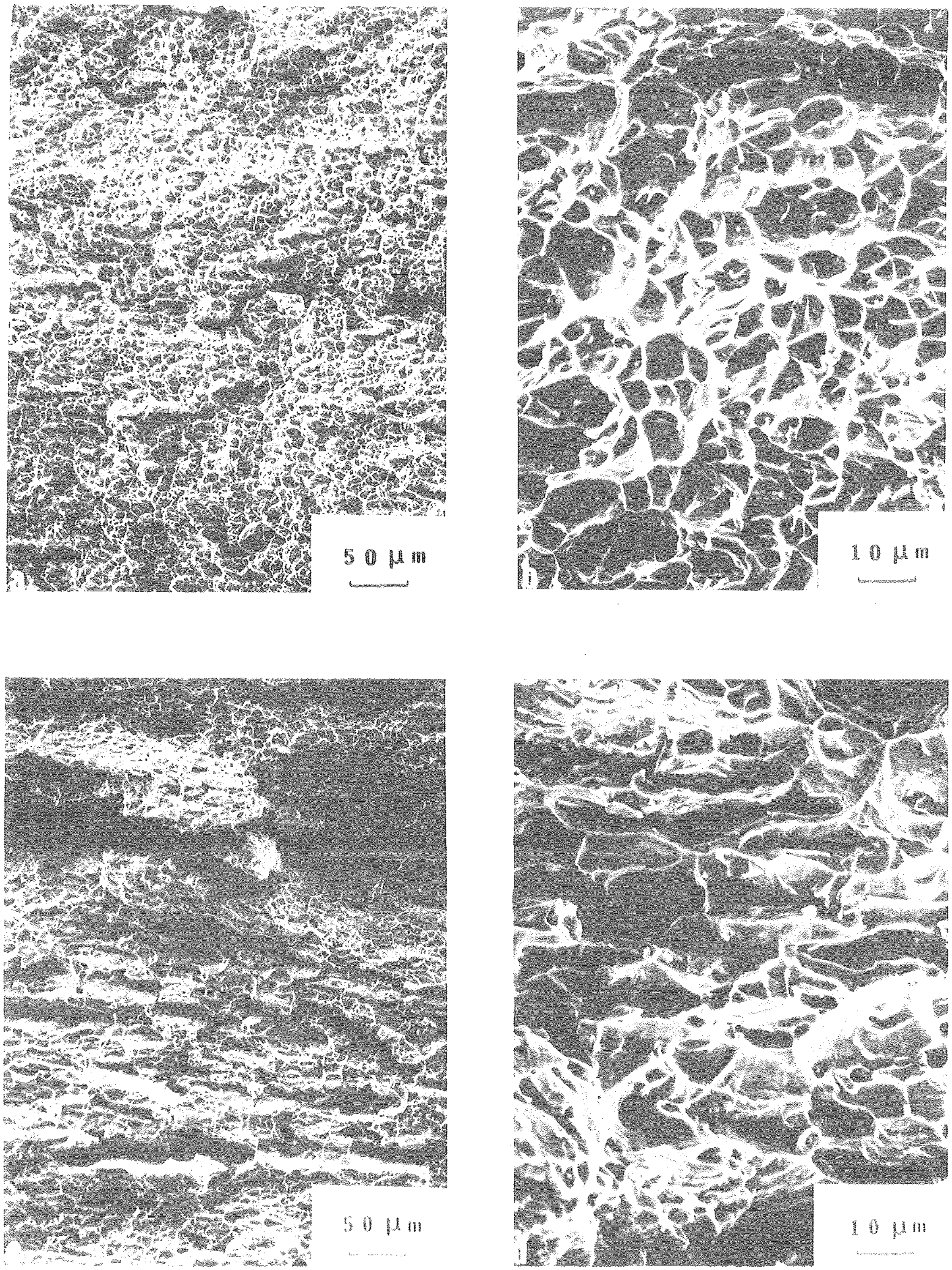

XBB 768-7776

Fig. 35.

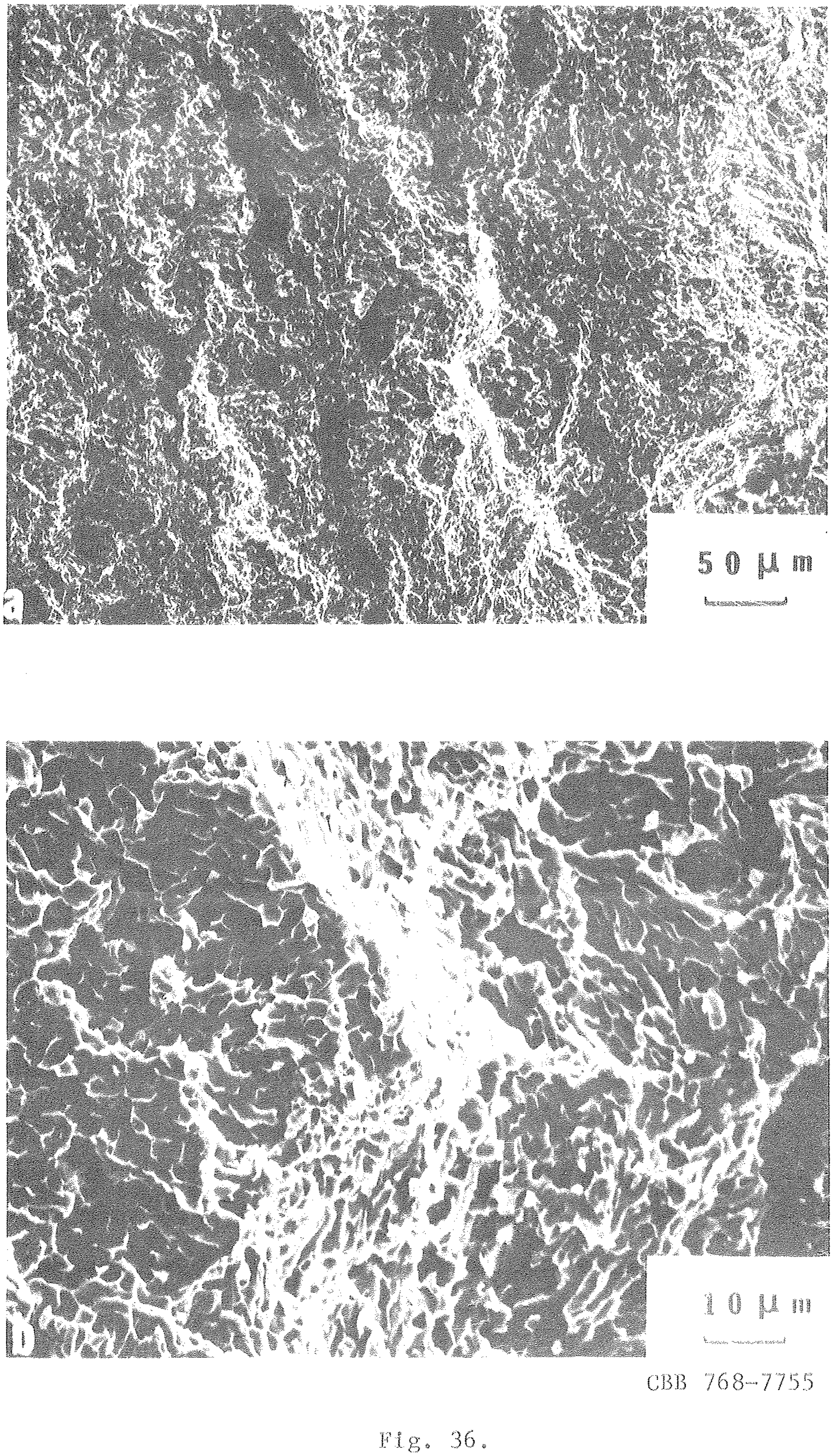

CBB 768-7755

Fig. 36.

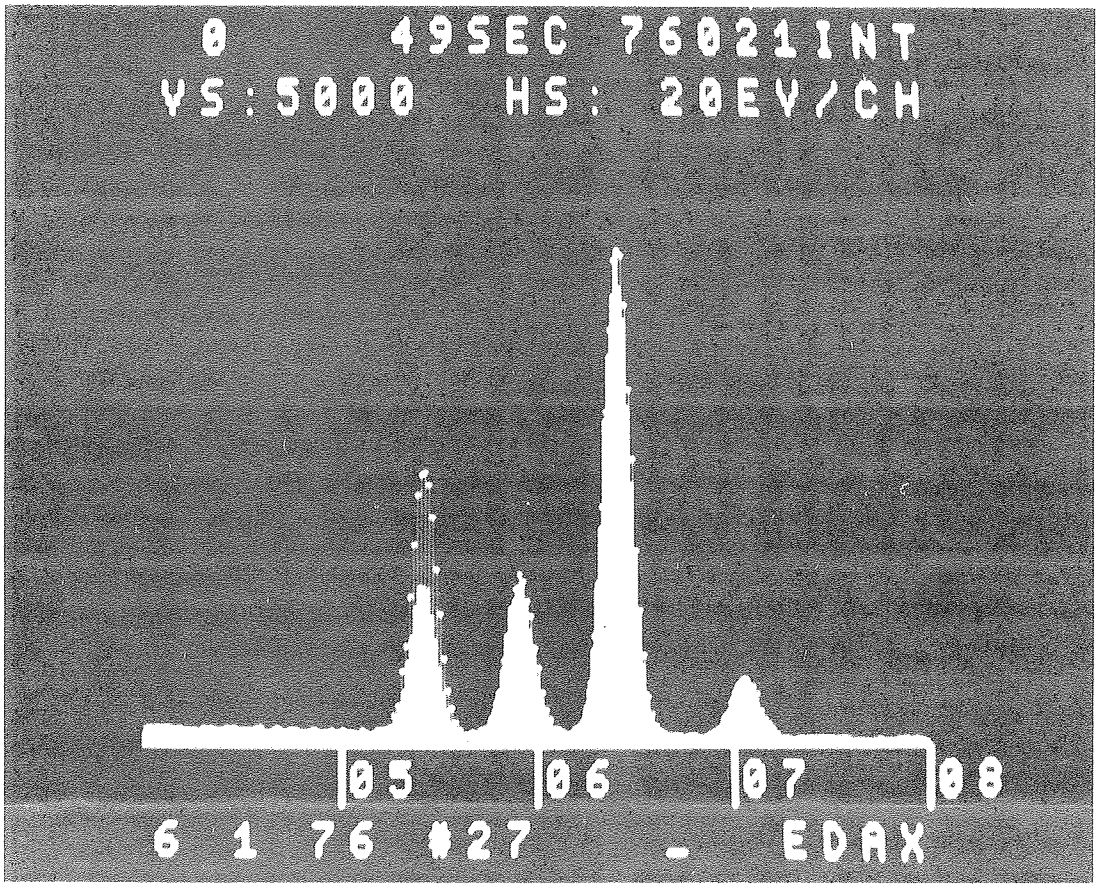

XBB 768-7747

Fig. 37.

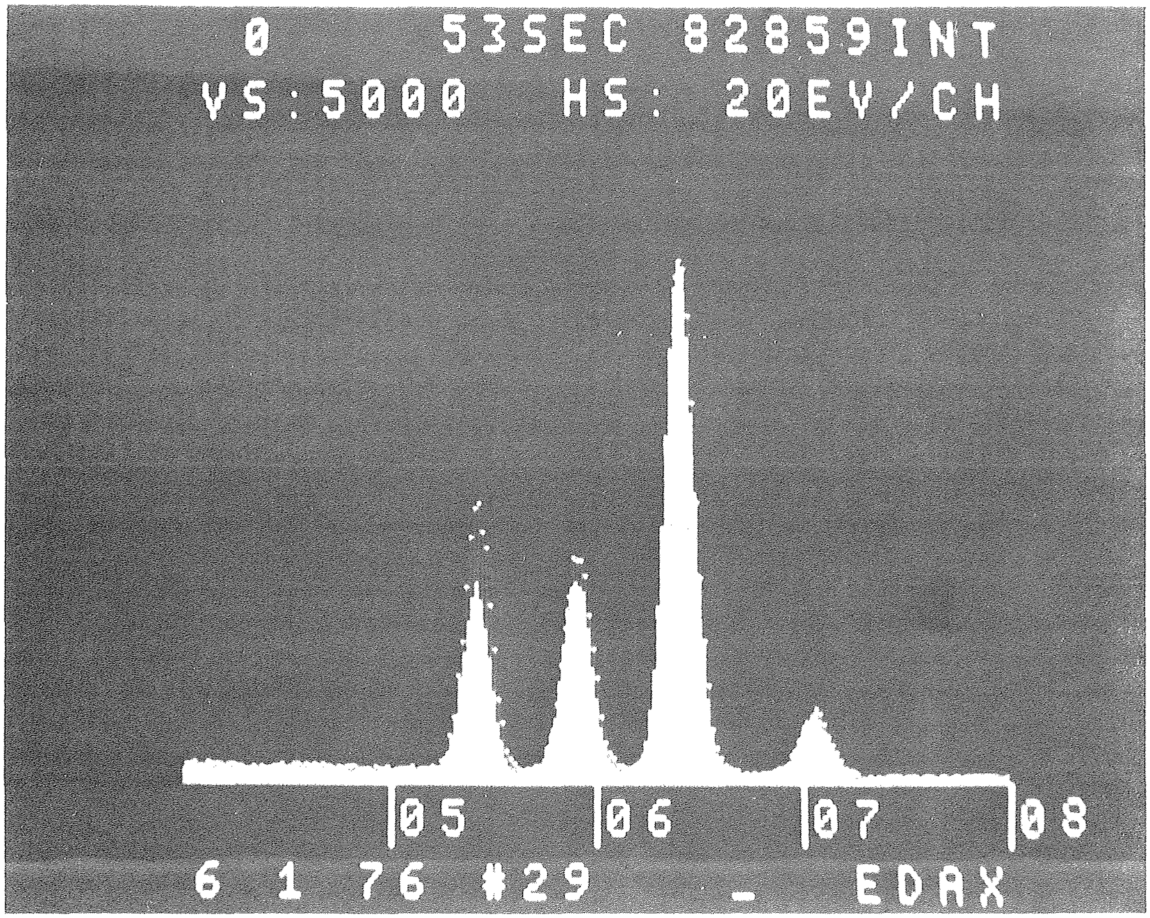

XBB 768-7746

Fig. 38.

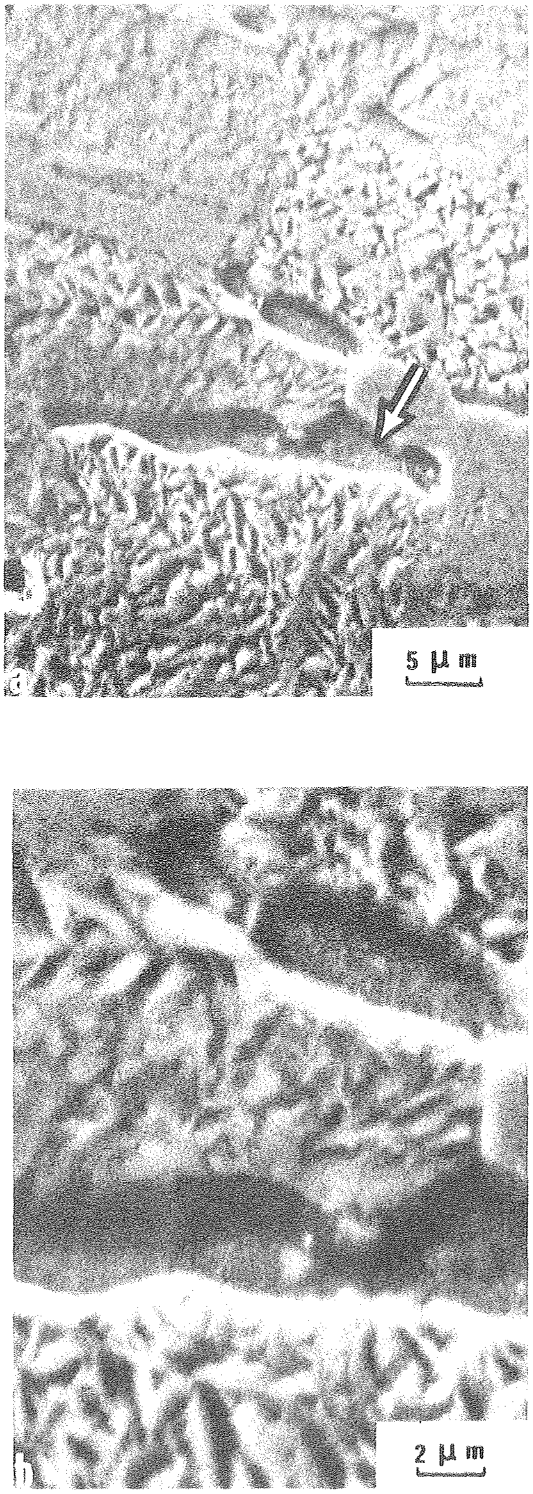

XBB 769-8377

Fig. 39.

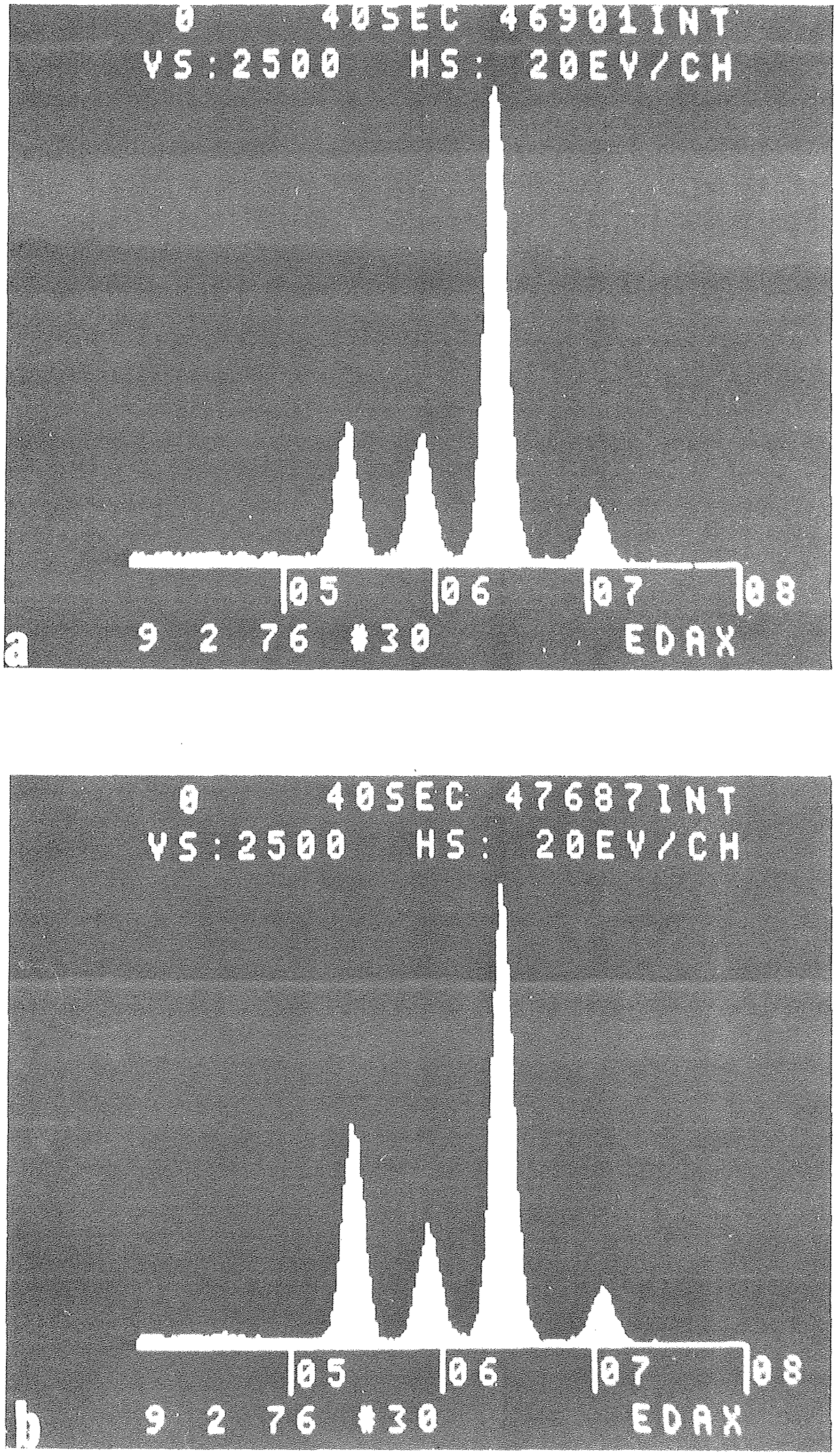

XBB 769-8379

Fig. 40.

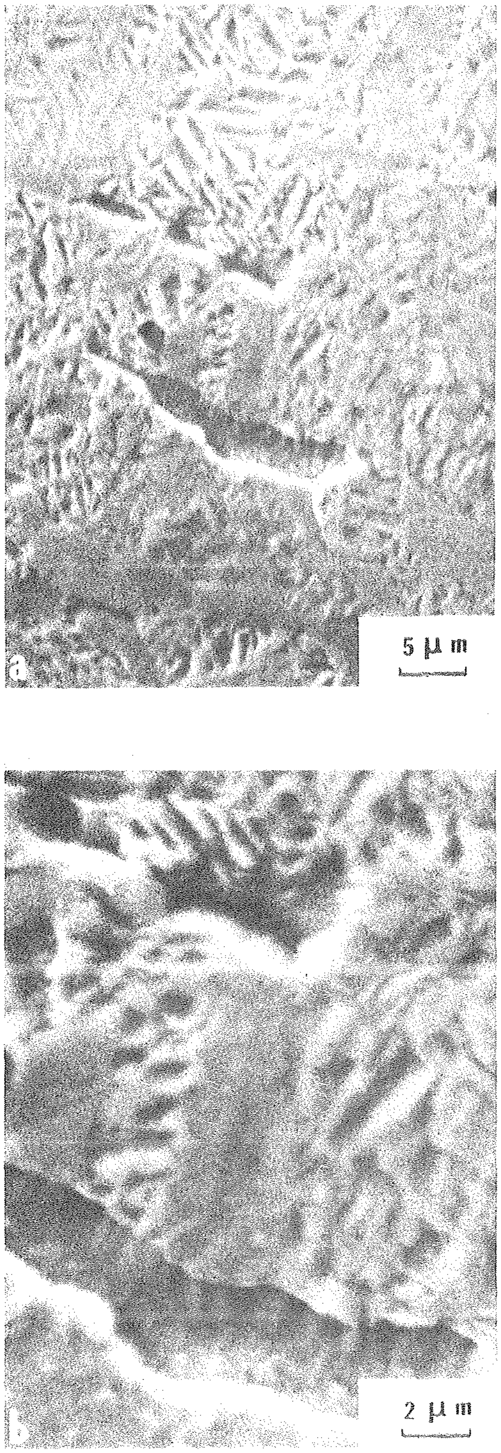

XBB 769-8376

Fig. 41.

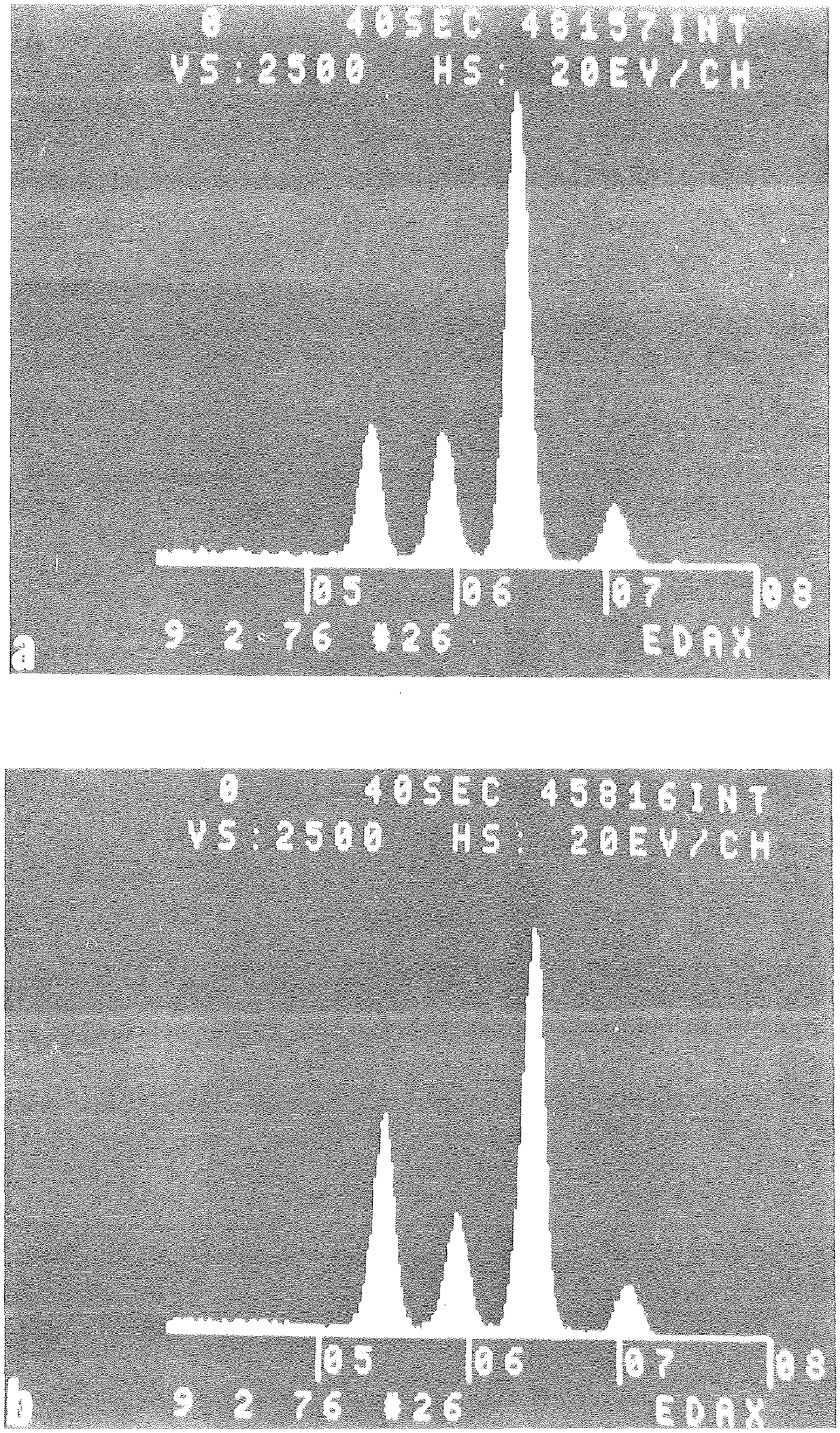

XBB 769-8380

Fig. 42.

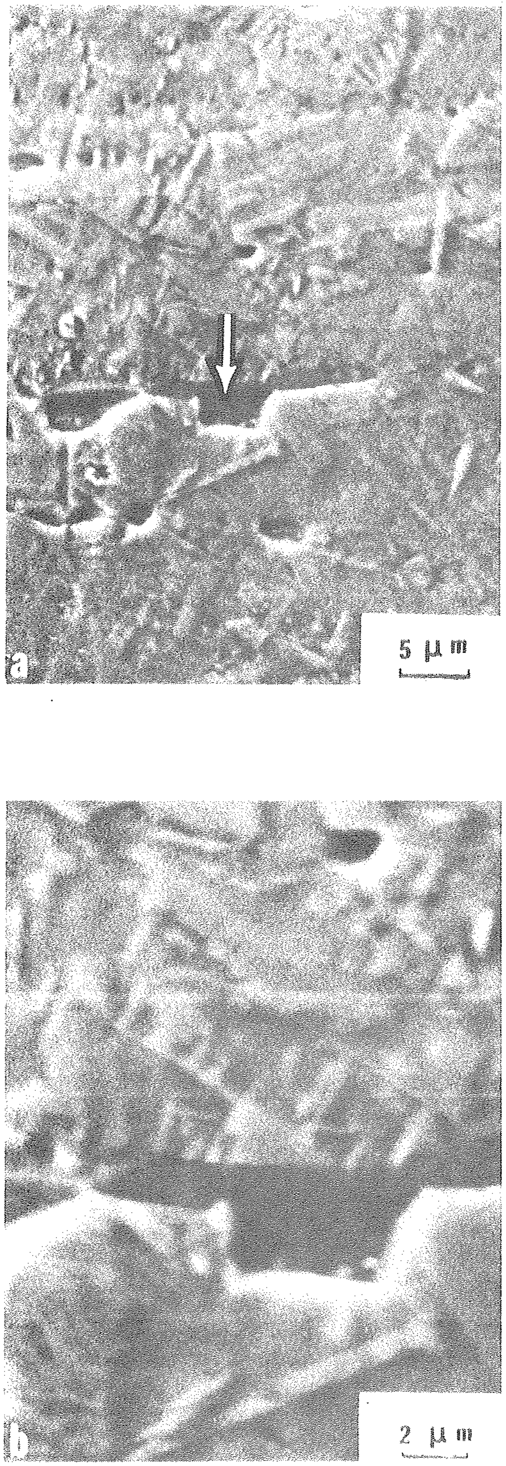

XBB 769-8375

Fig. 43.

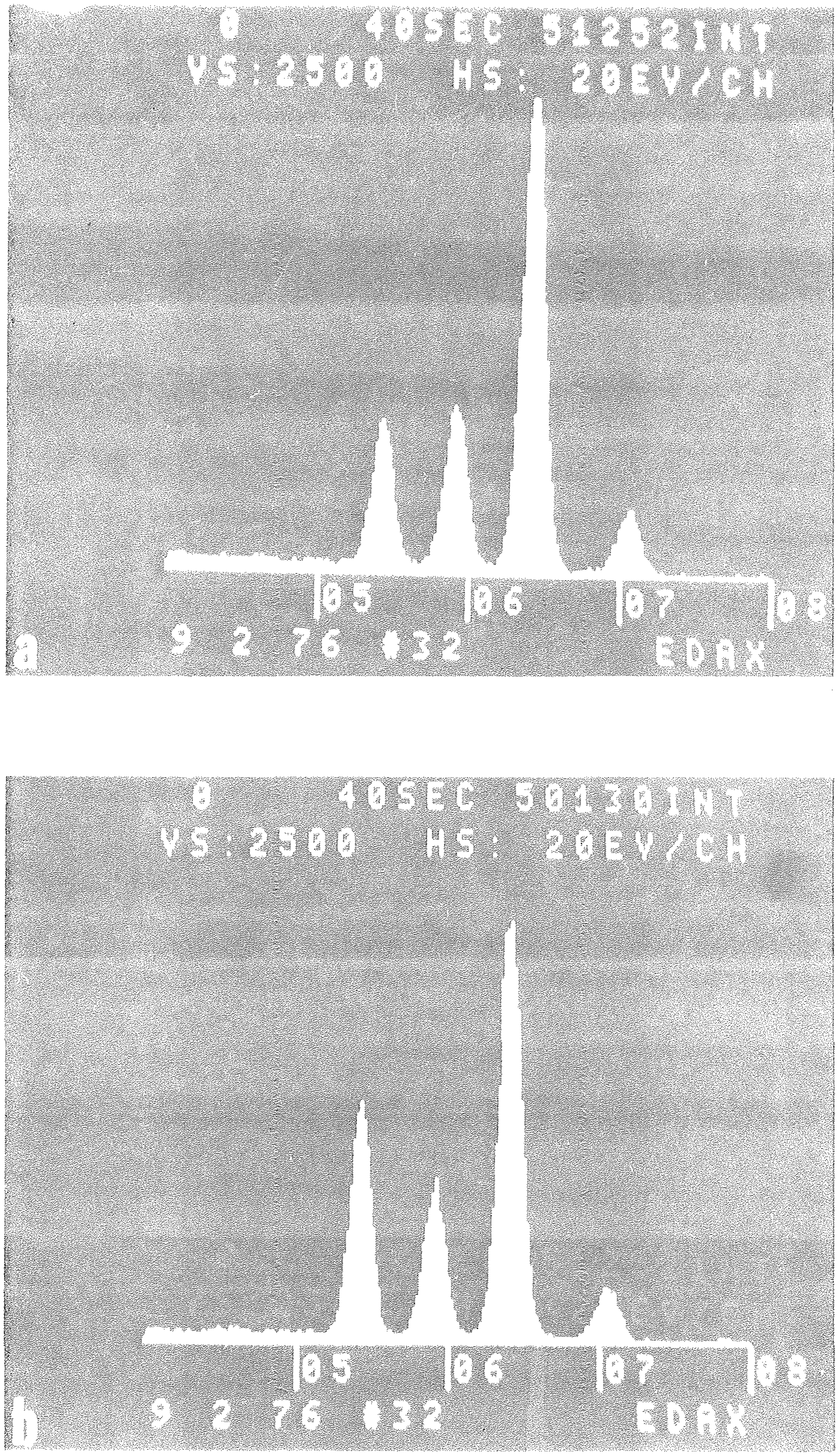

XBB 769-8378

Fig. 44.

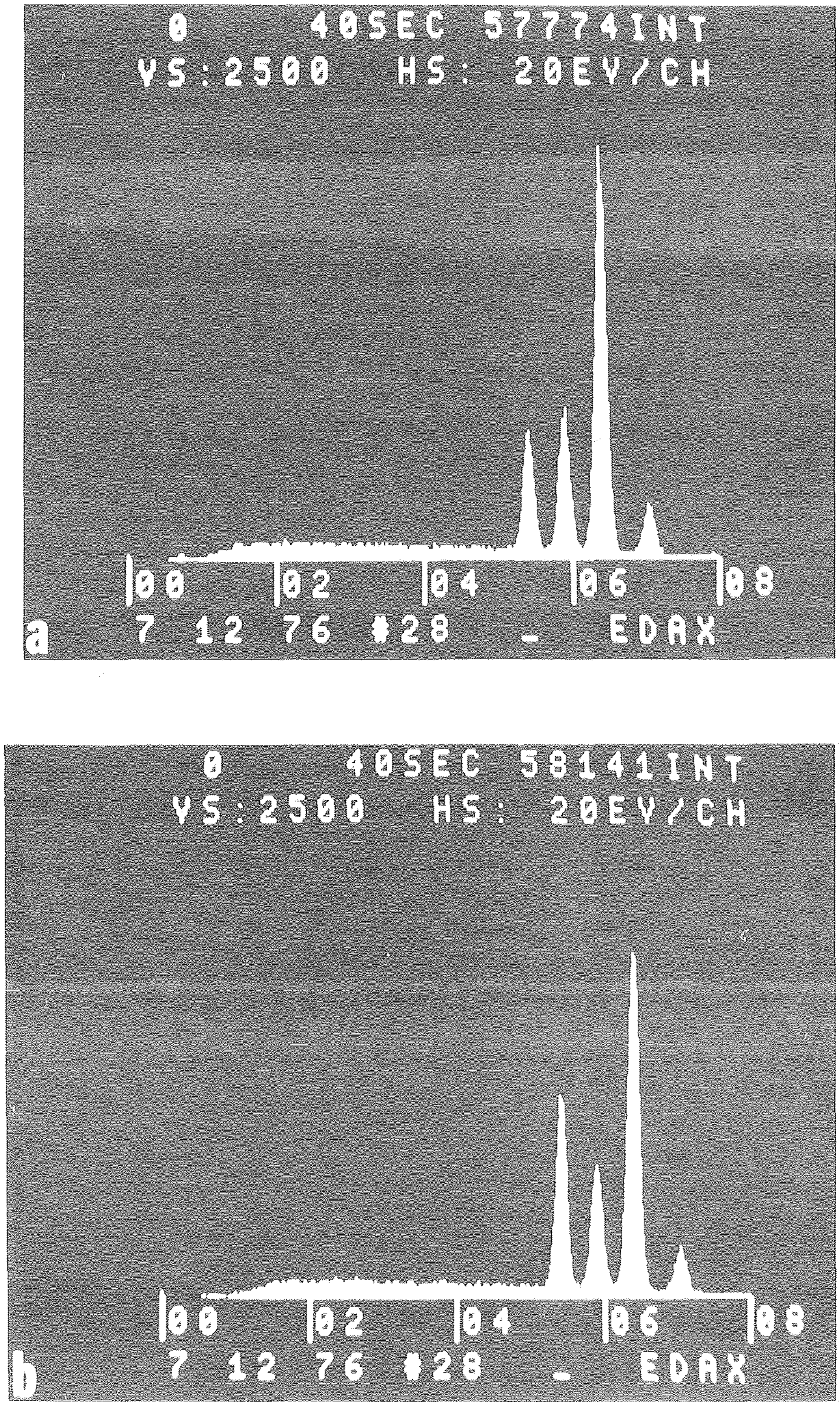

CBB 768-7753

Fig. 45.

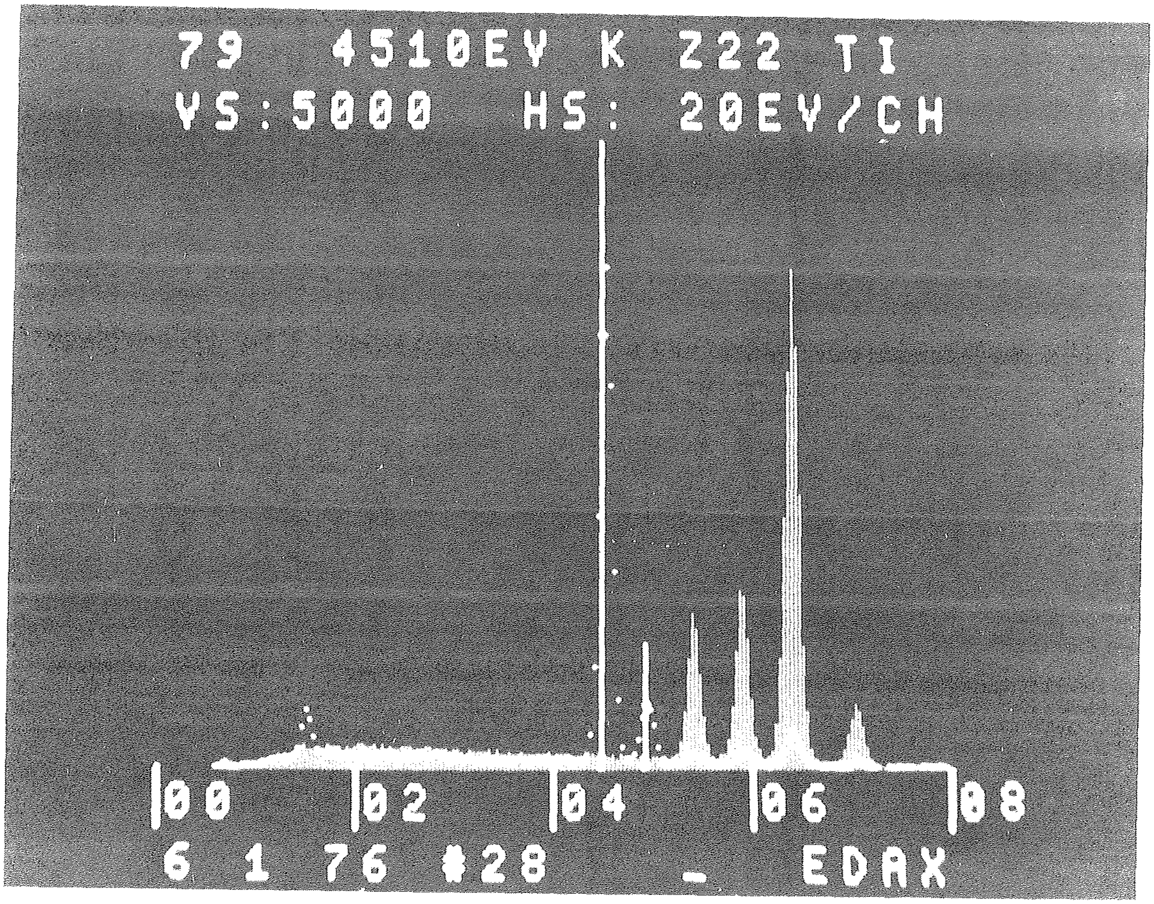

XBB 768-7748

Fig. 46.

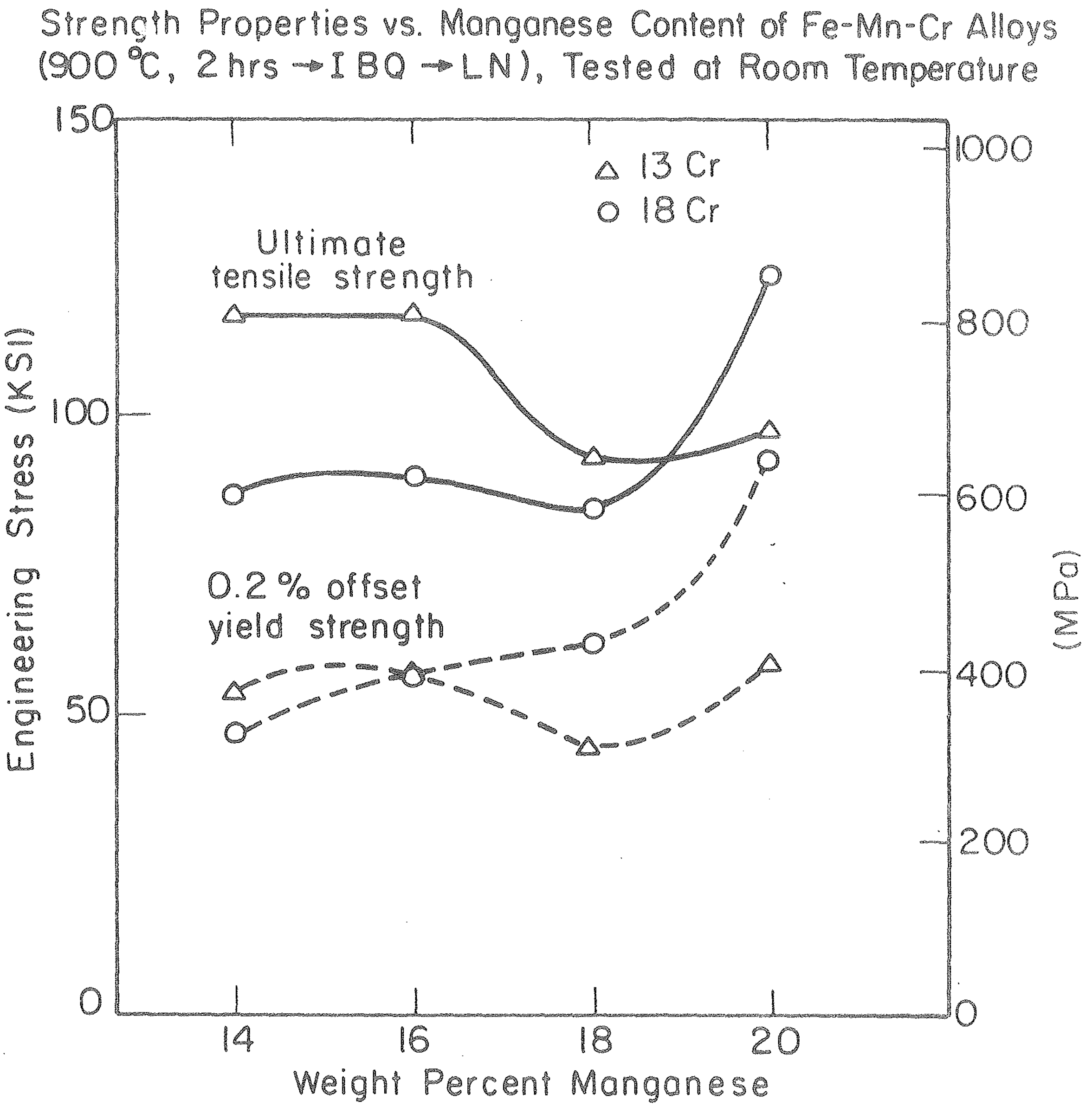

XBL764-6685

Fig. 47.

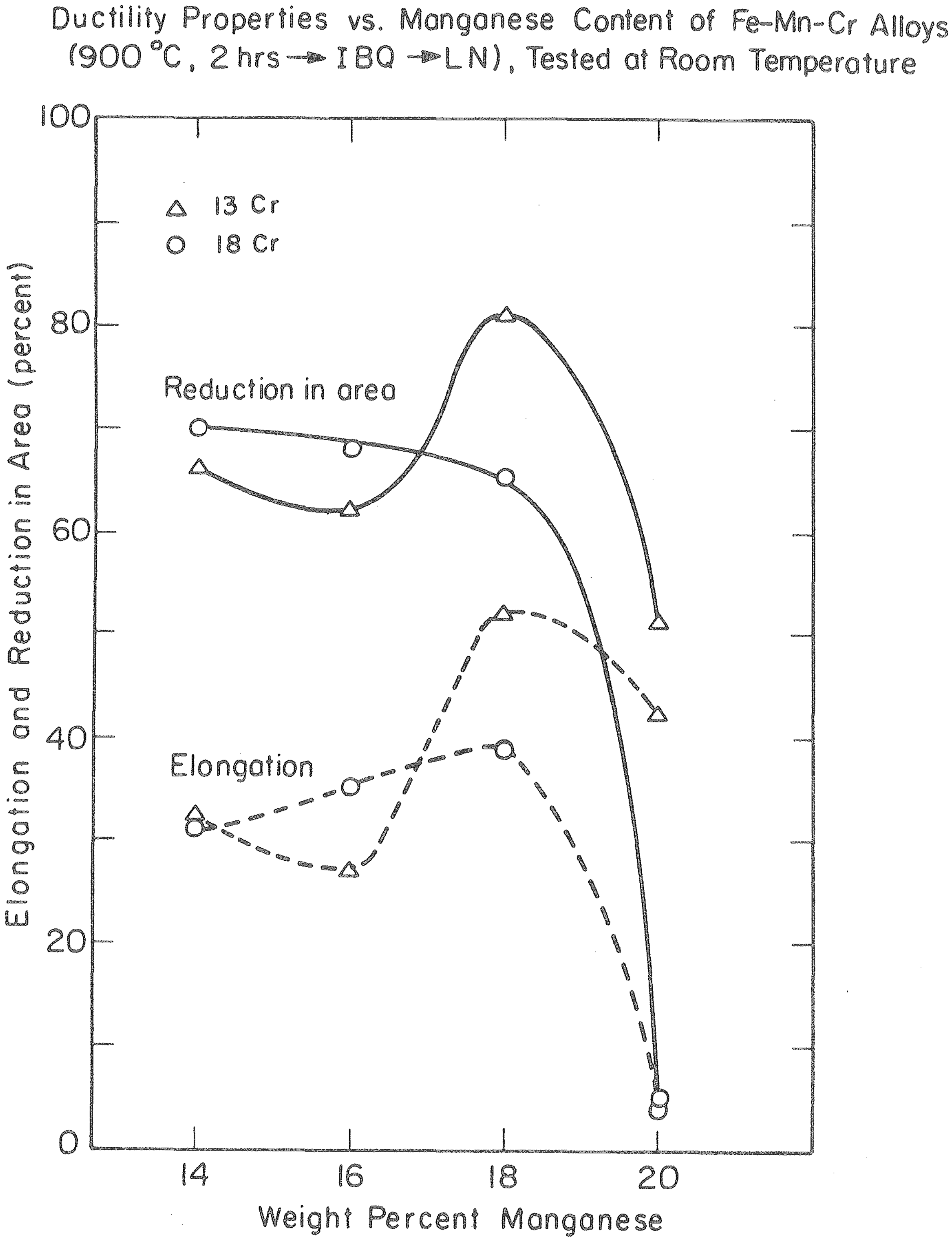

XBL 764-6684

Fig. 48.

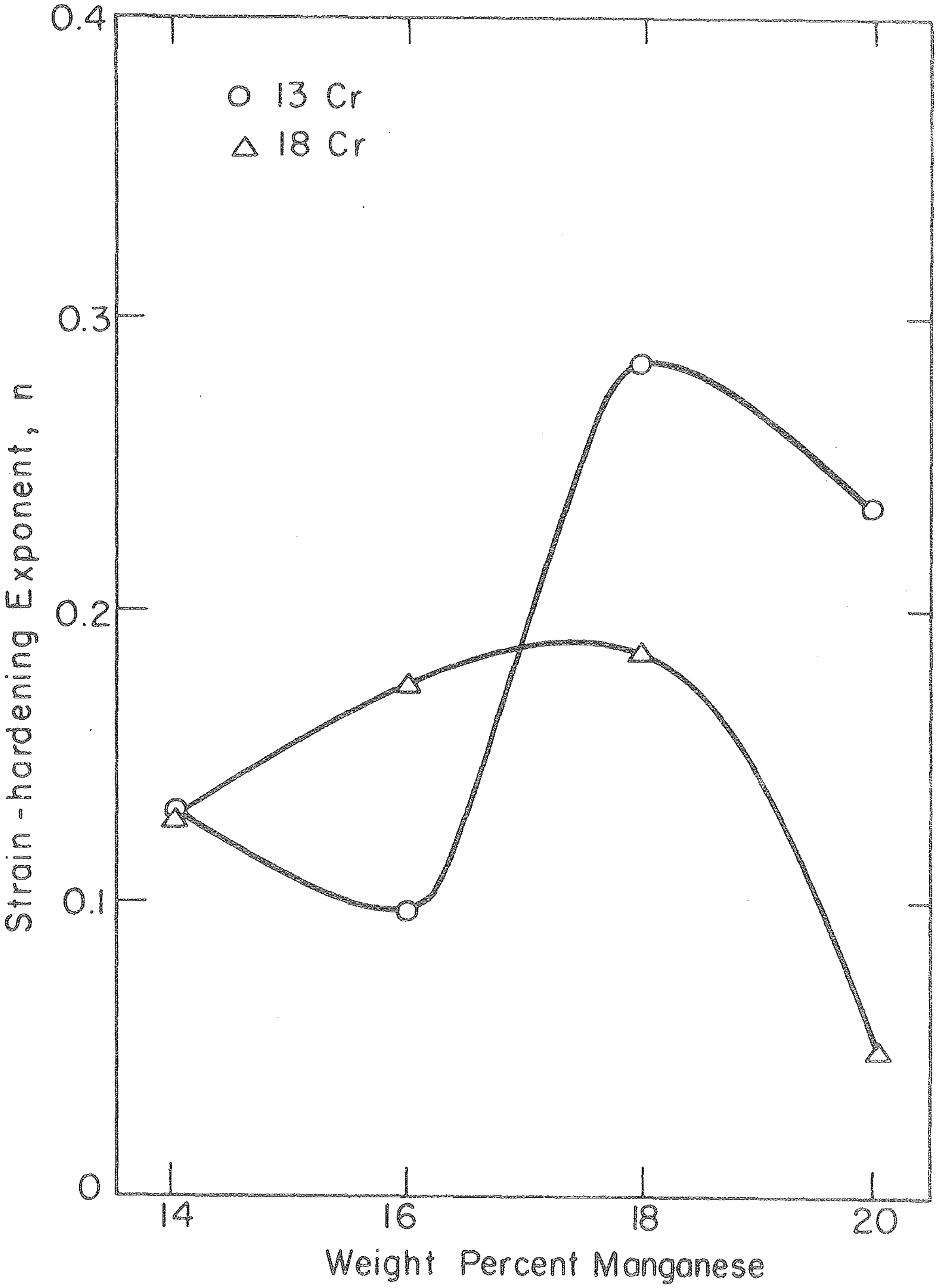

Strain-hardening Exponent vs. Manganese Content for Fe-Mn-Cr Alloys (900°C, 2 hrs → IBQ → LN), Tested at Room Temperature

XBL 769-7569

Fig. 49.

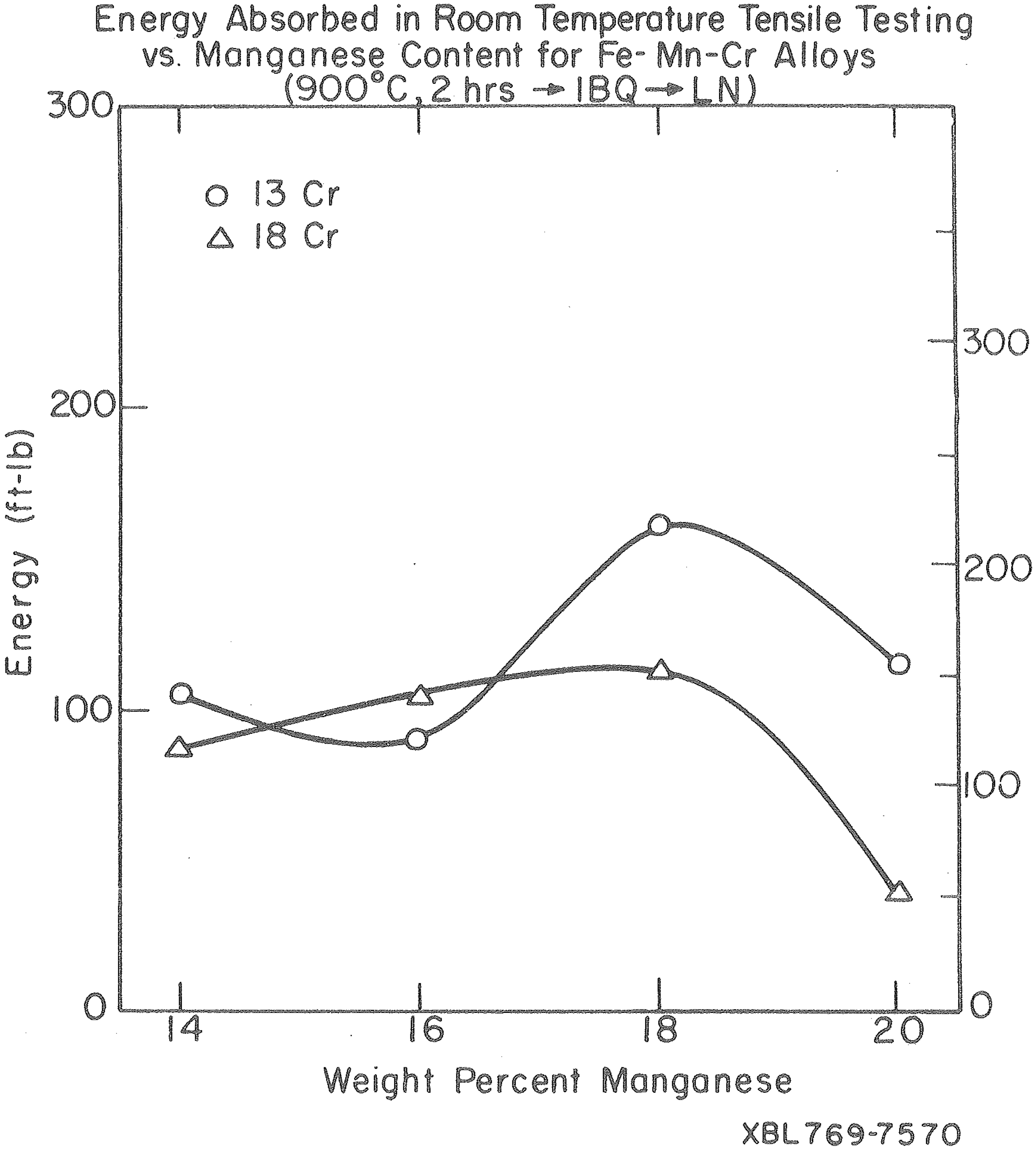
Energy Absorbed in Room Temperature Tensile Testing
vs. Manganese Content for Fe-Mn-Cr Alloys
(900°C, 2 hrs → IBQ → LN)
○ 13 Cr
△ 18 Cr
Energy (ft-lb)
(joules)
Weight Percent Manganese
0
100
200
300
14
16
18
20
XBL769-7570

Fig. 50.

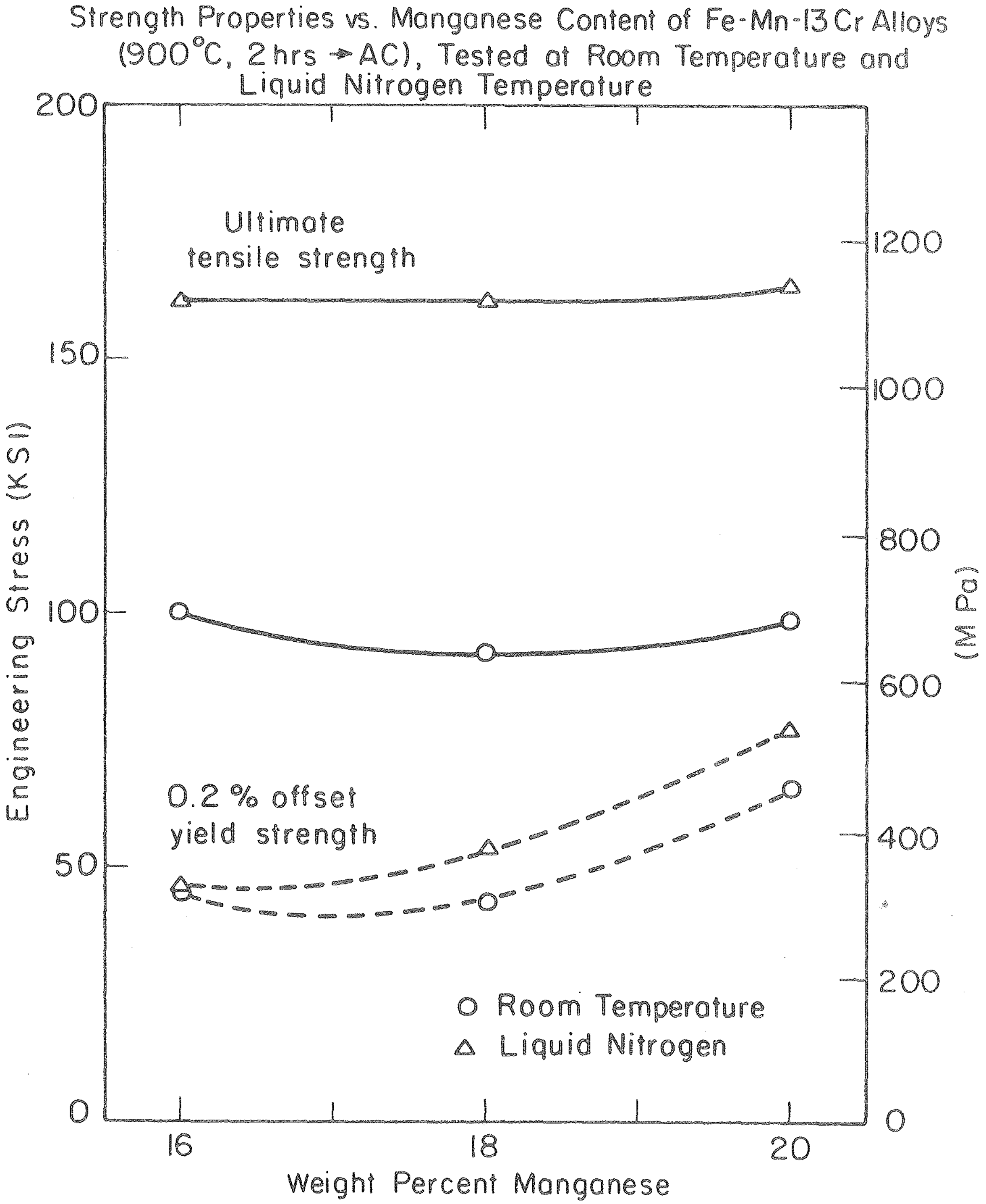

XBL 764-6689

Fig. 51.

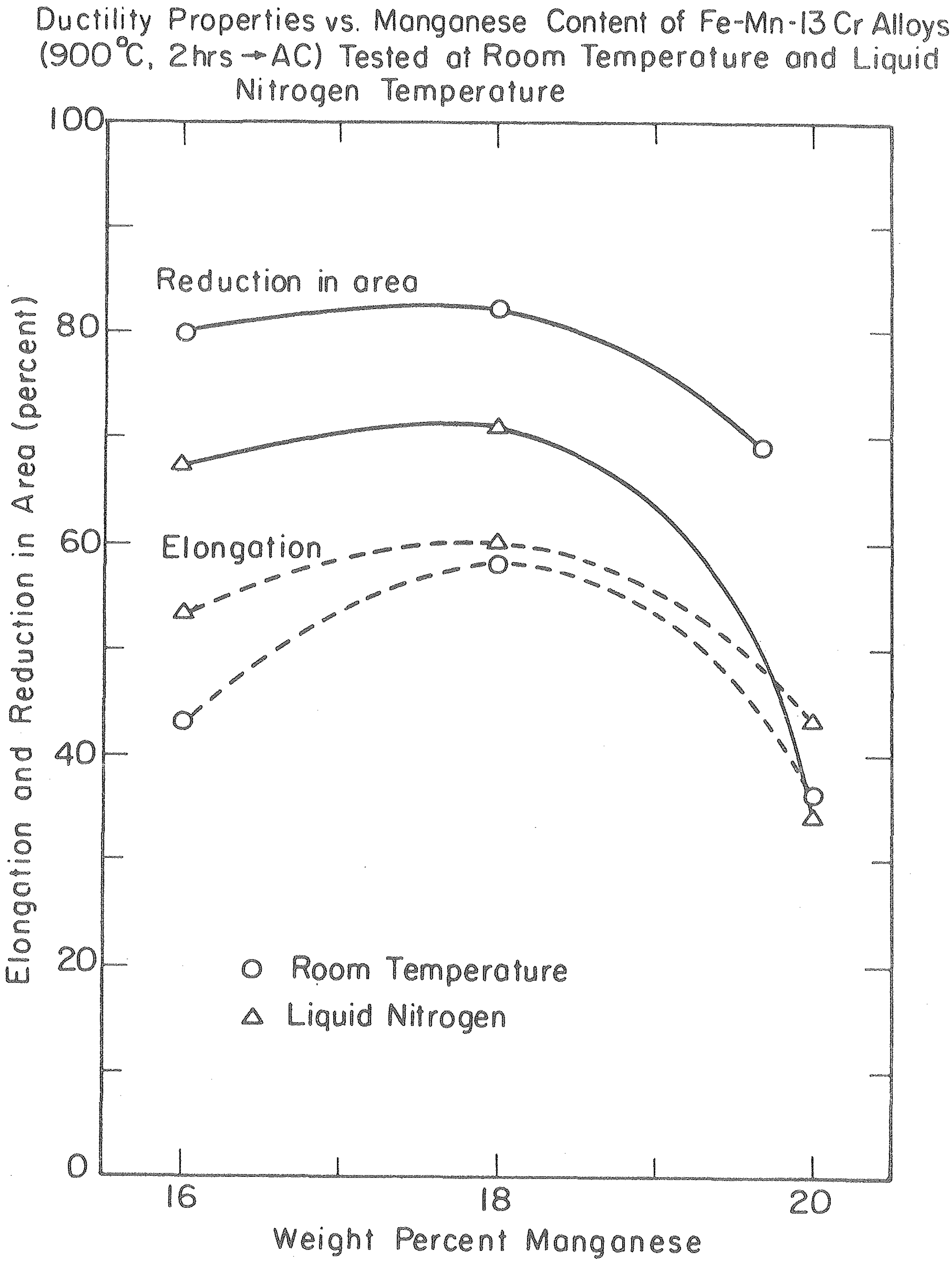

XBL 764-6688

Fig. 52.

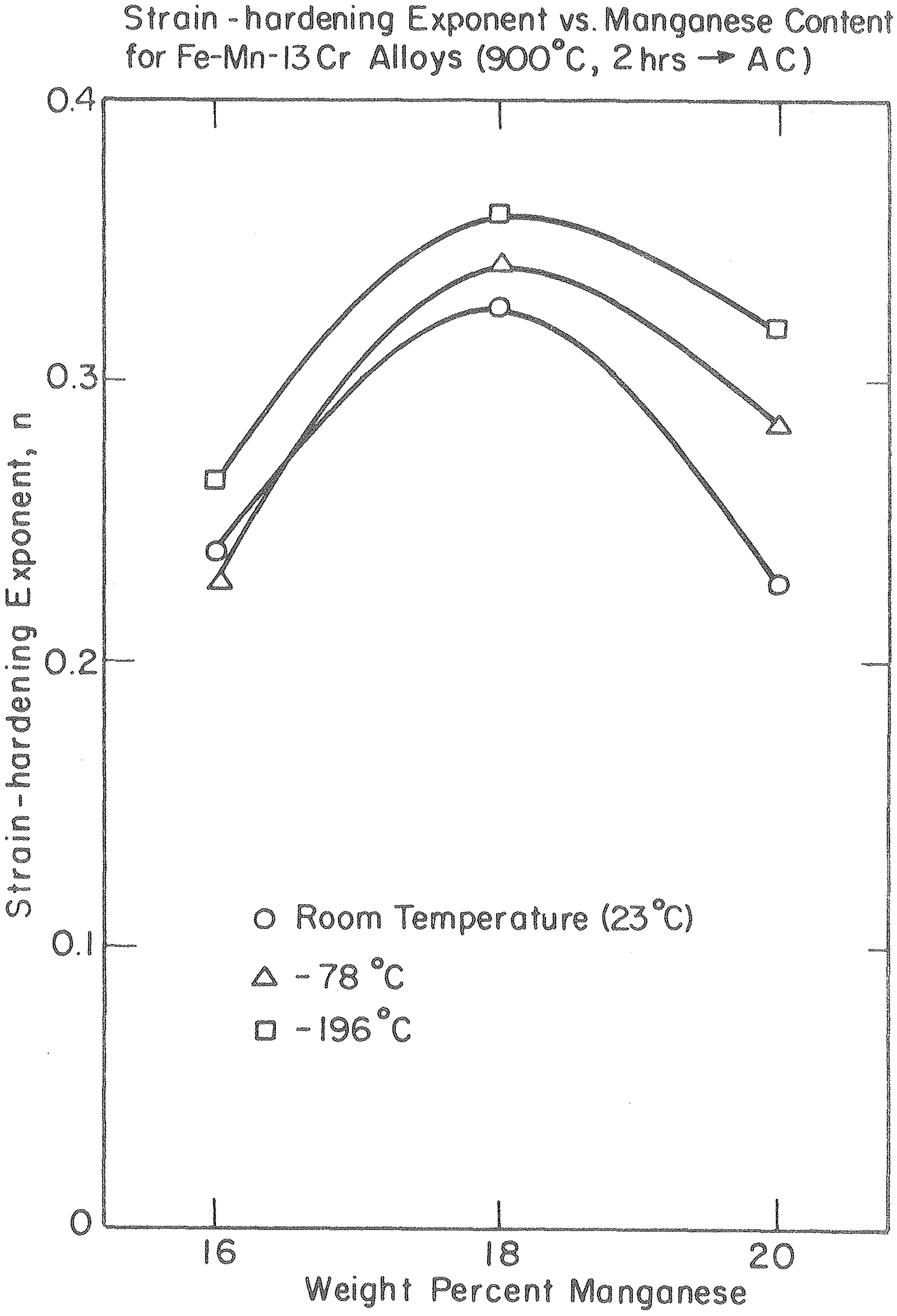

XBL769-7571

Fig. 53.

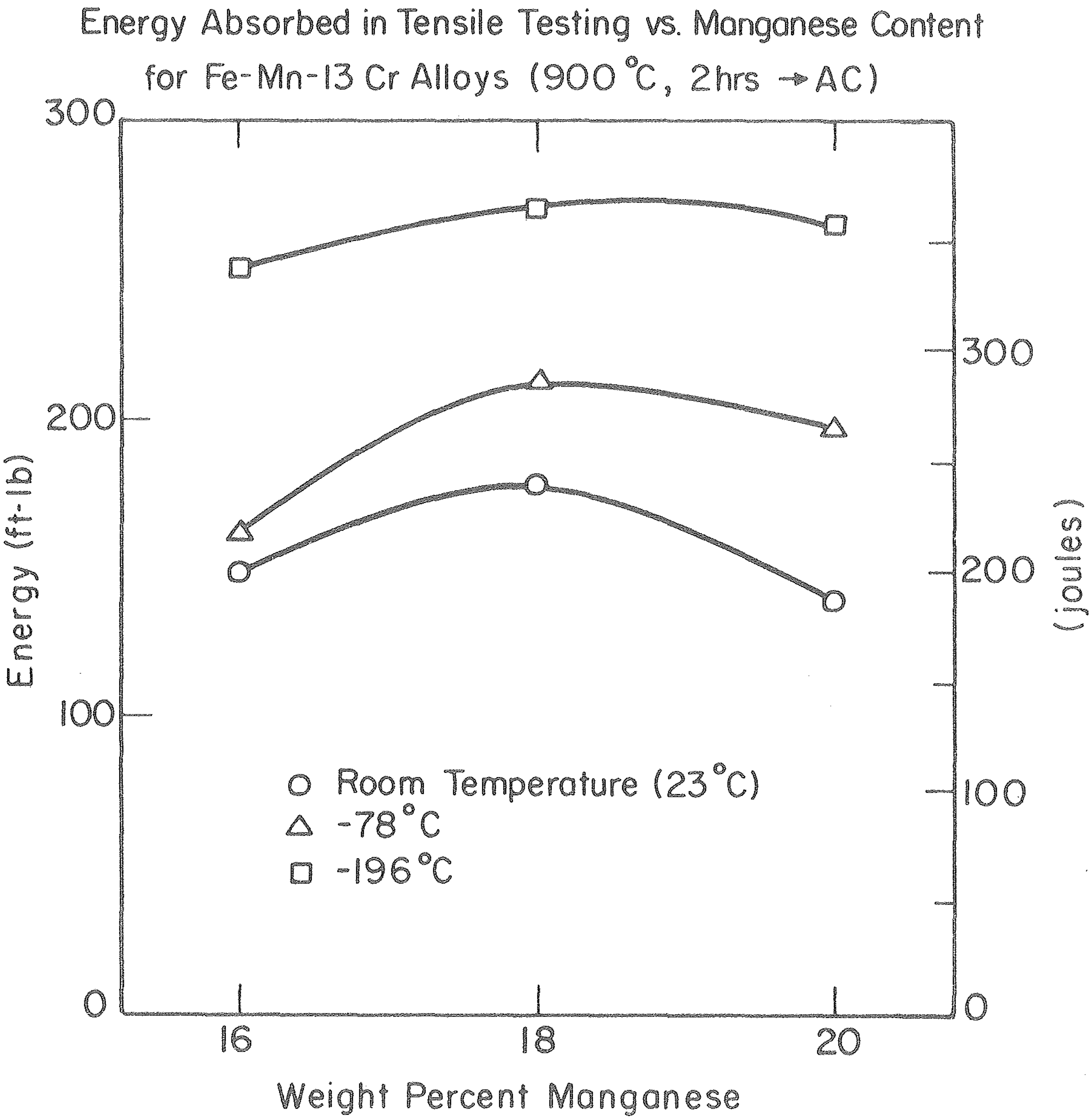

XBL 769-7572

Fig. 54.

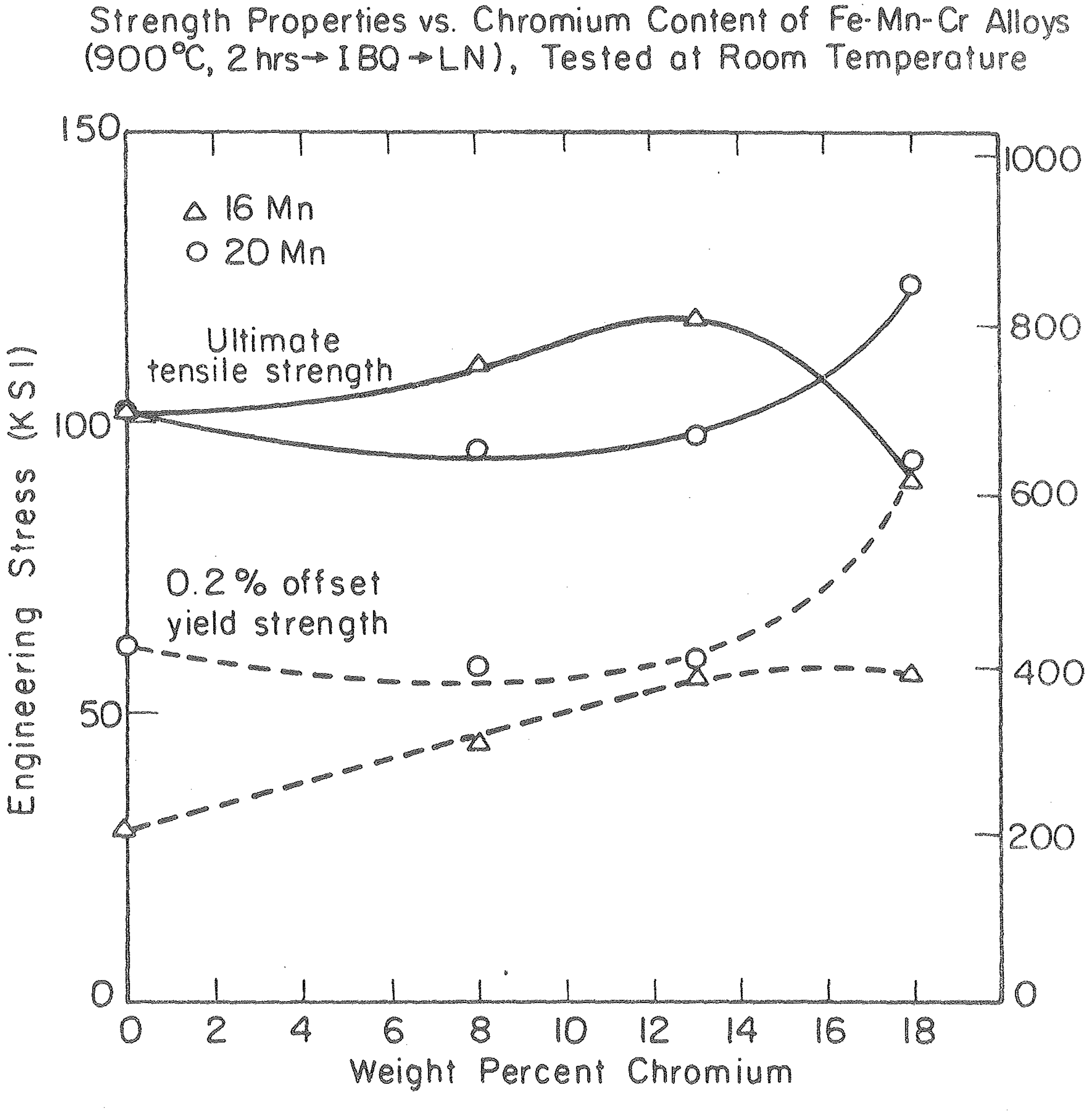

XBL 764-6687

Fig. 55.

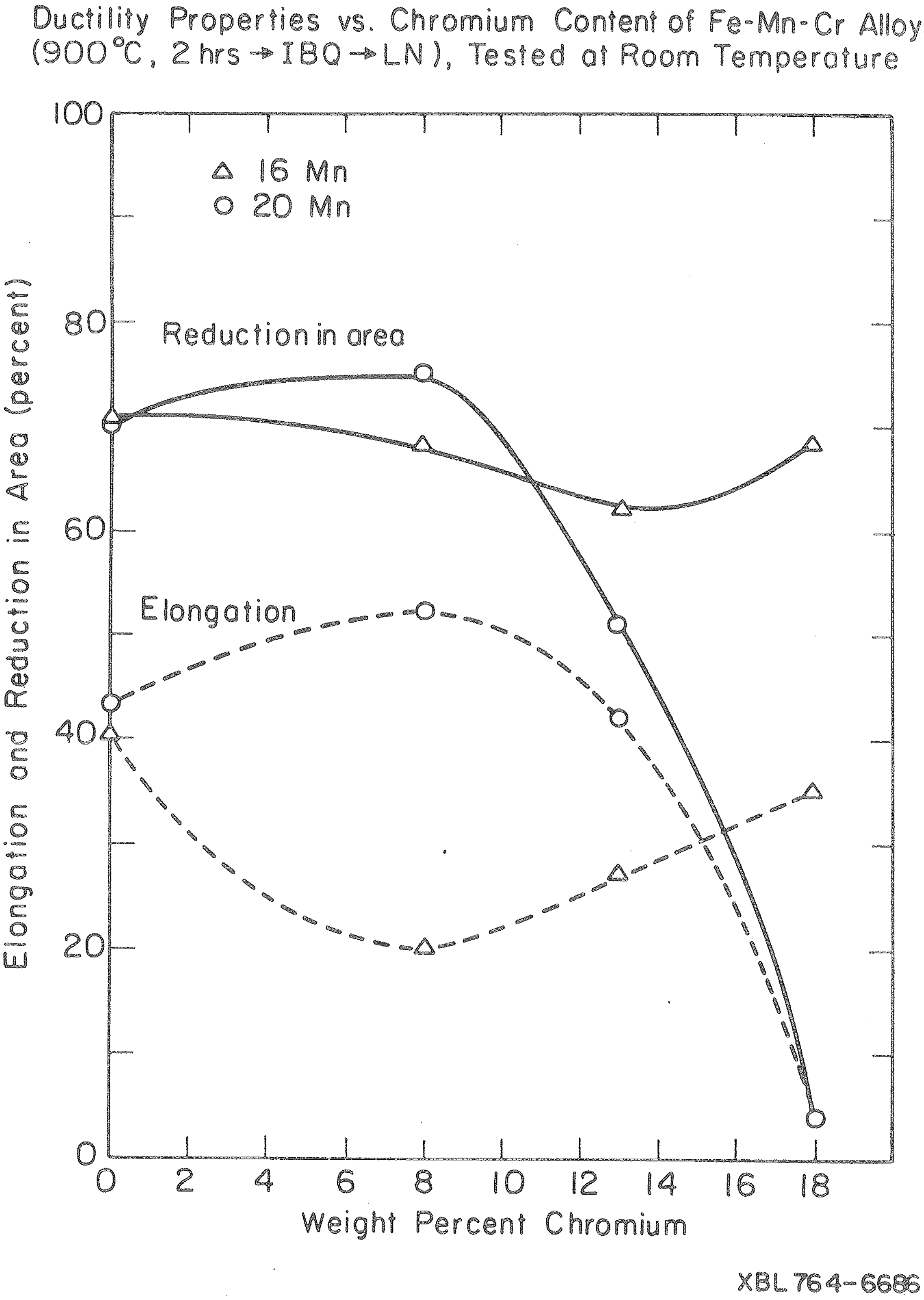
Ductility Properties vs. Chromium Content of Fe-Mn-Cr Alloys
(900°C, 2 hrs → IBQ → LN), Tested at Room Temperature
△ 16 Mn
○ 20 Mn
Reduction in area
Elongation
Elongation and Reduction in Area (percent)
0
20
40
60
80
100
0
2
4
6
8
10
12
14
16
18
Weight Percent Chromium
XBL 764-6686

Fig. 56.

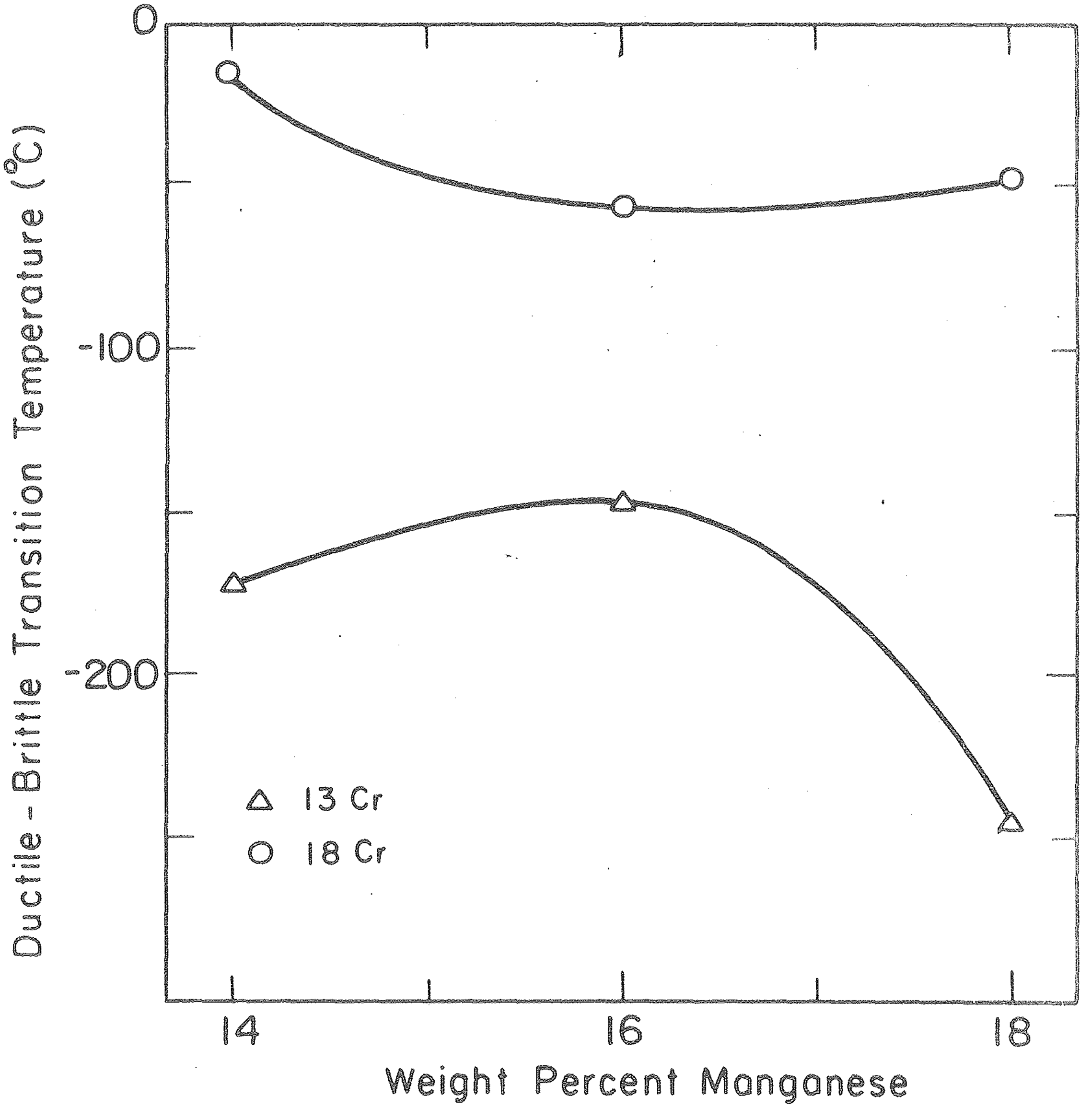

XBL764-6700

Fig. 57.

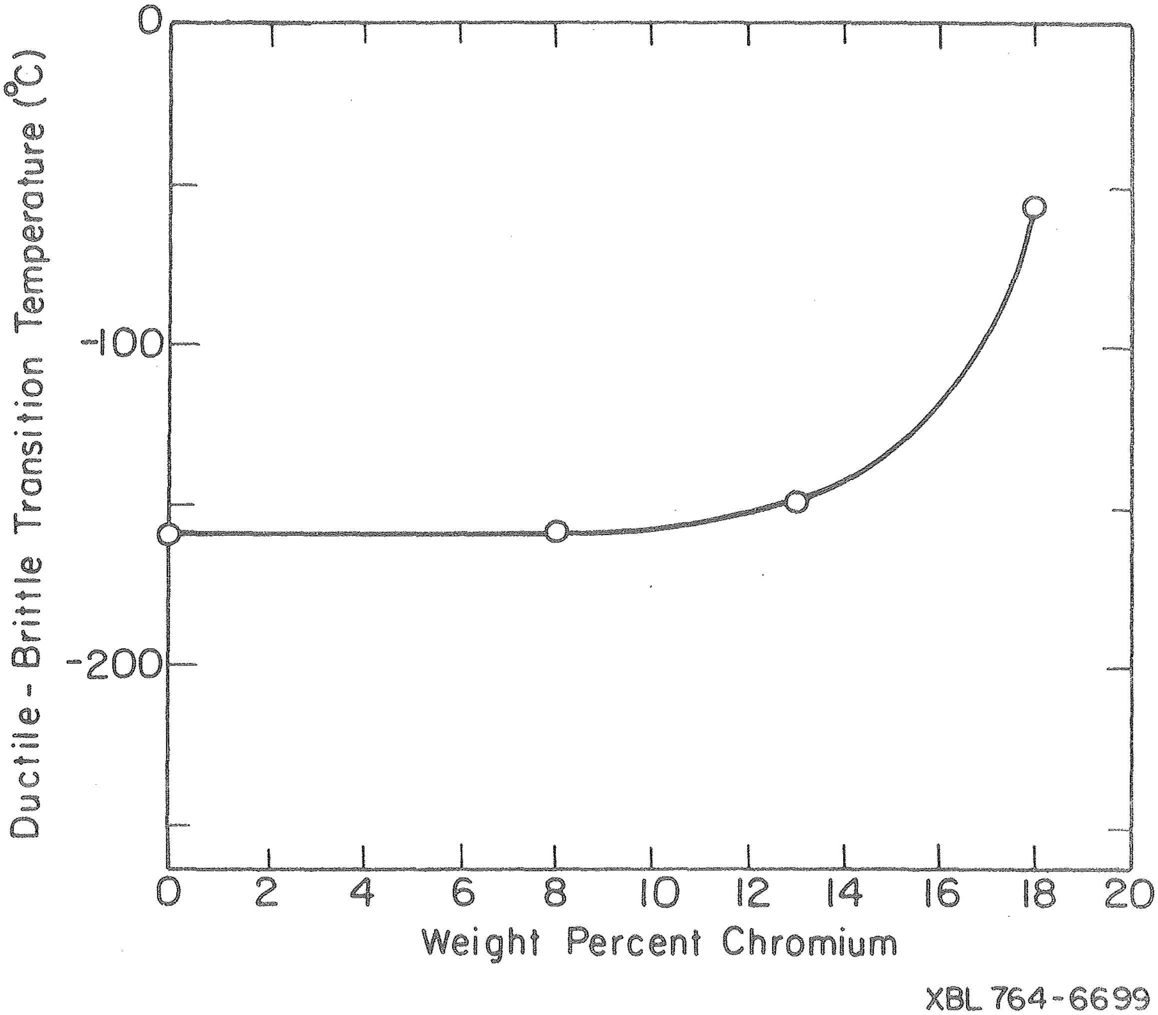
0
-100
-200
Ductile - Brittle Transition Temperature (°C)
0
2
4
6
8
10
12
14
16
18
20
Weight Percent Chromium
XBL 764-6699

Fig. 58.

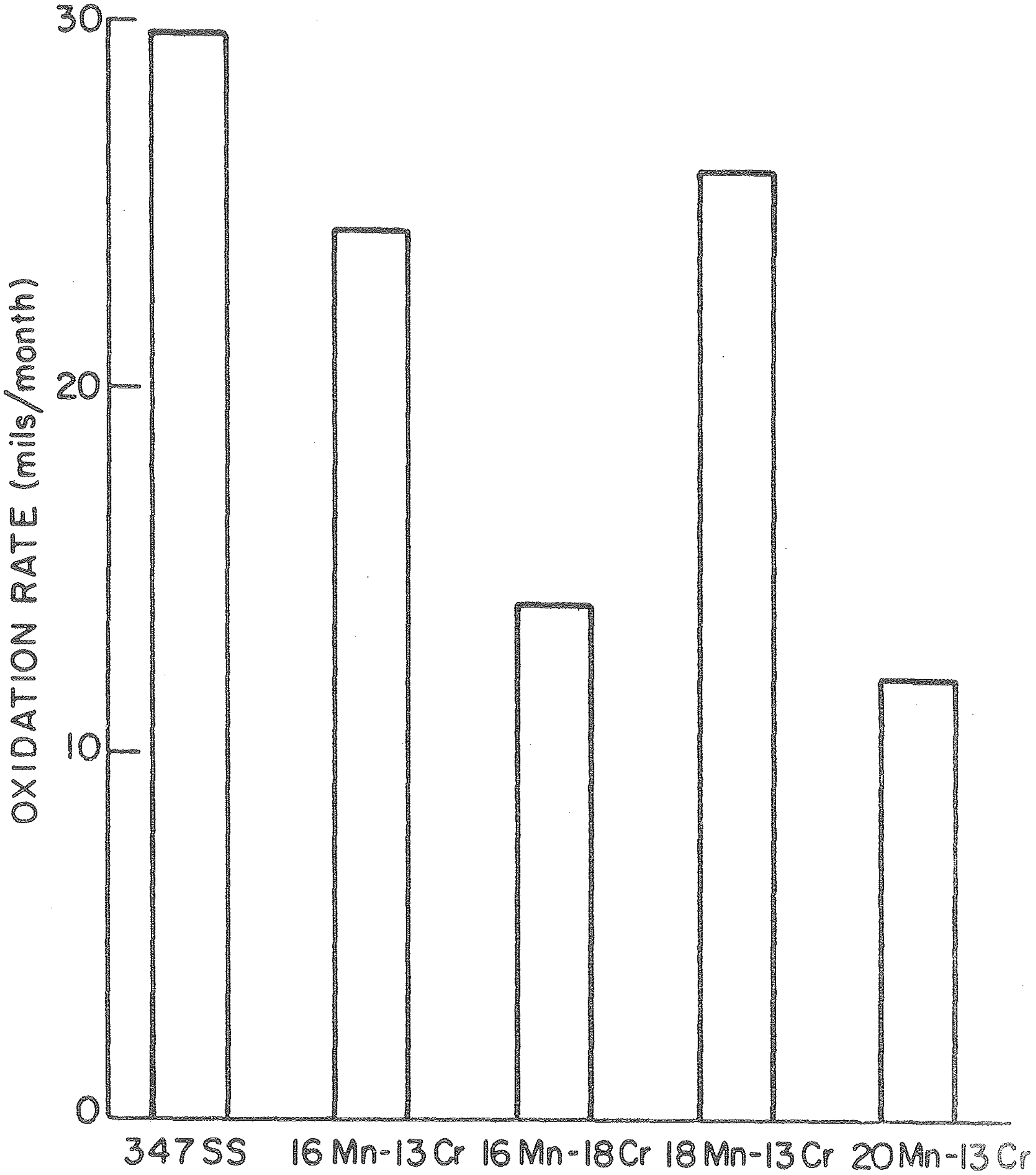

XBL 7611-7734

Fig. 59.

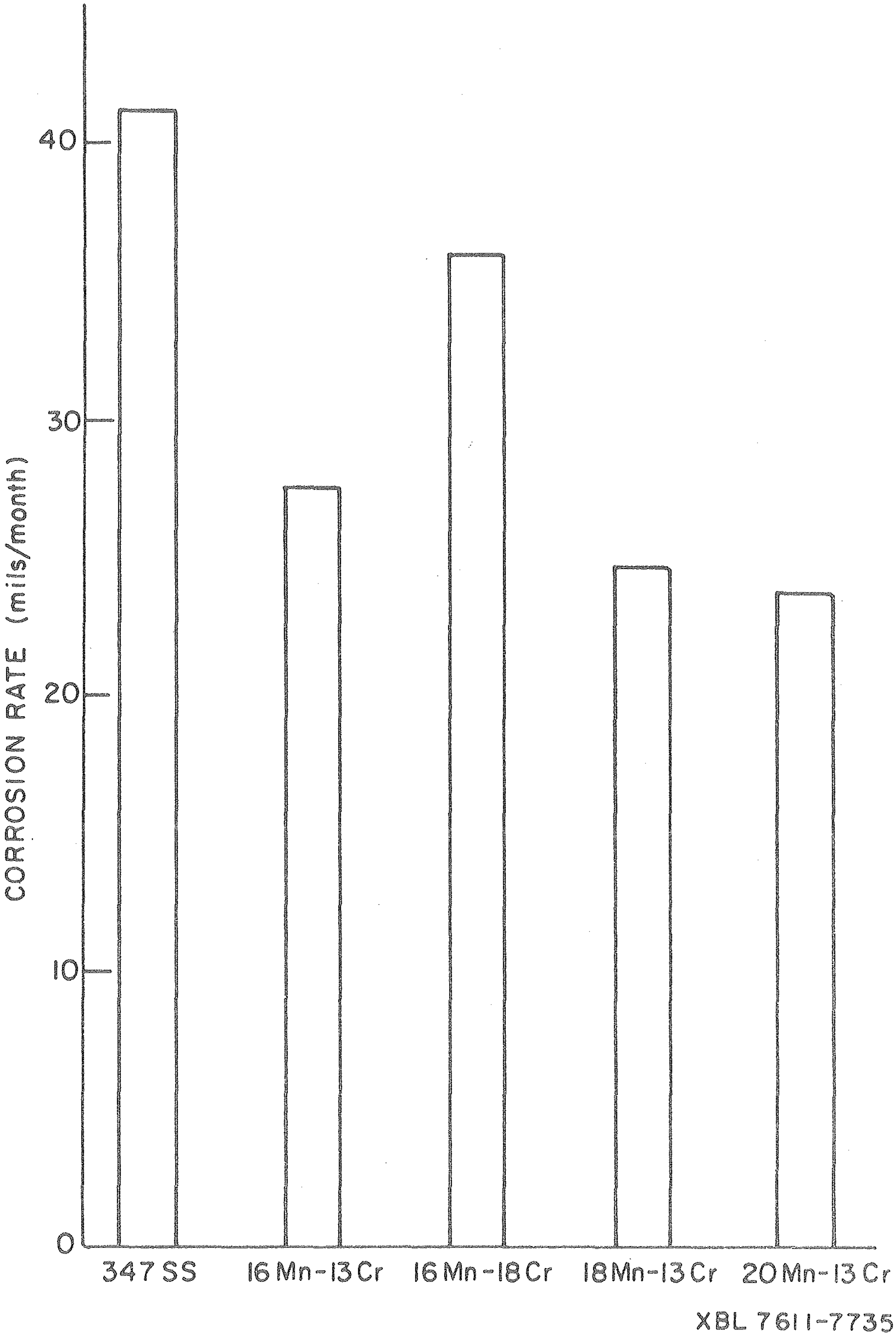
CORROSION RATE (mils/month)
40
30
20
10
0
347 SS
16 Mn-13 Cr
16 Mn-18 Cr
18 Mn-13 Cr
20 Mn-13 Cr
XBL 7611-7735

Fig. 60.

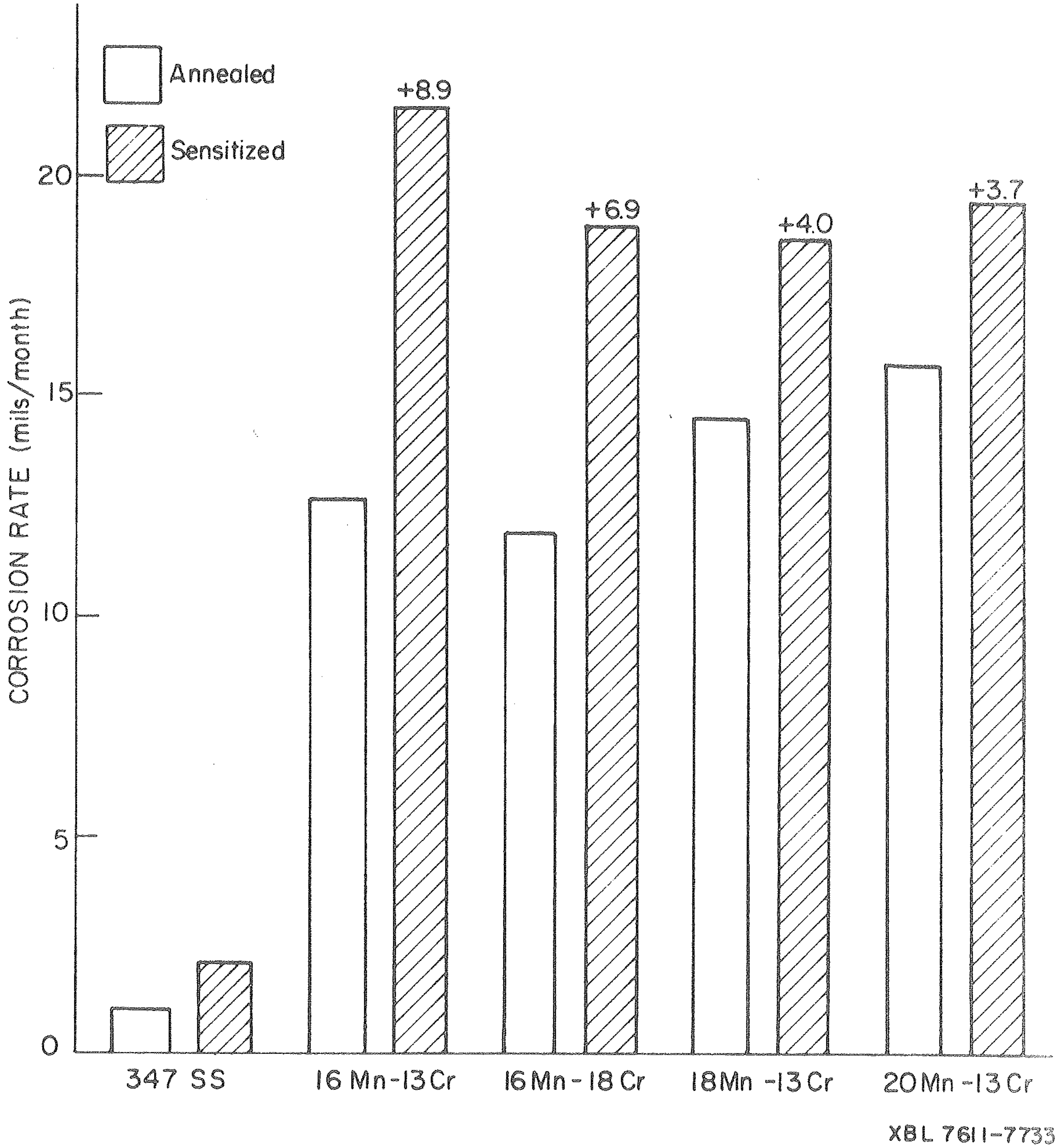
Annealed
Sensitized
CORROSION RATE (mils/month)
0
5
10
15
20
+8.9
+6.9
+4.0
+3.7
347 SS
16 Mn-13 Cr
16 Mn - 18 Cr
18Mn -13 Cr
20 Mn -13 Cr
XBL 7611-7733

Fig. 61.

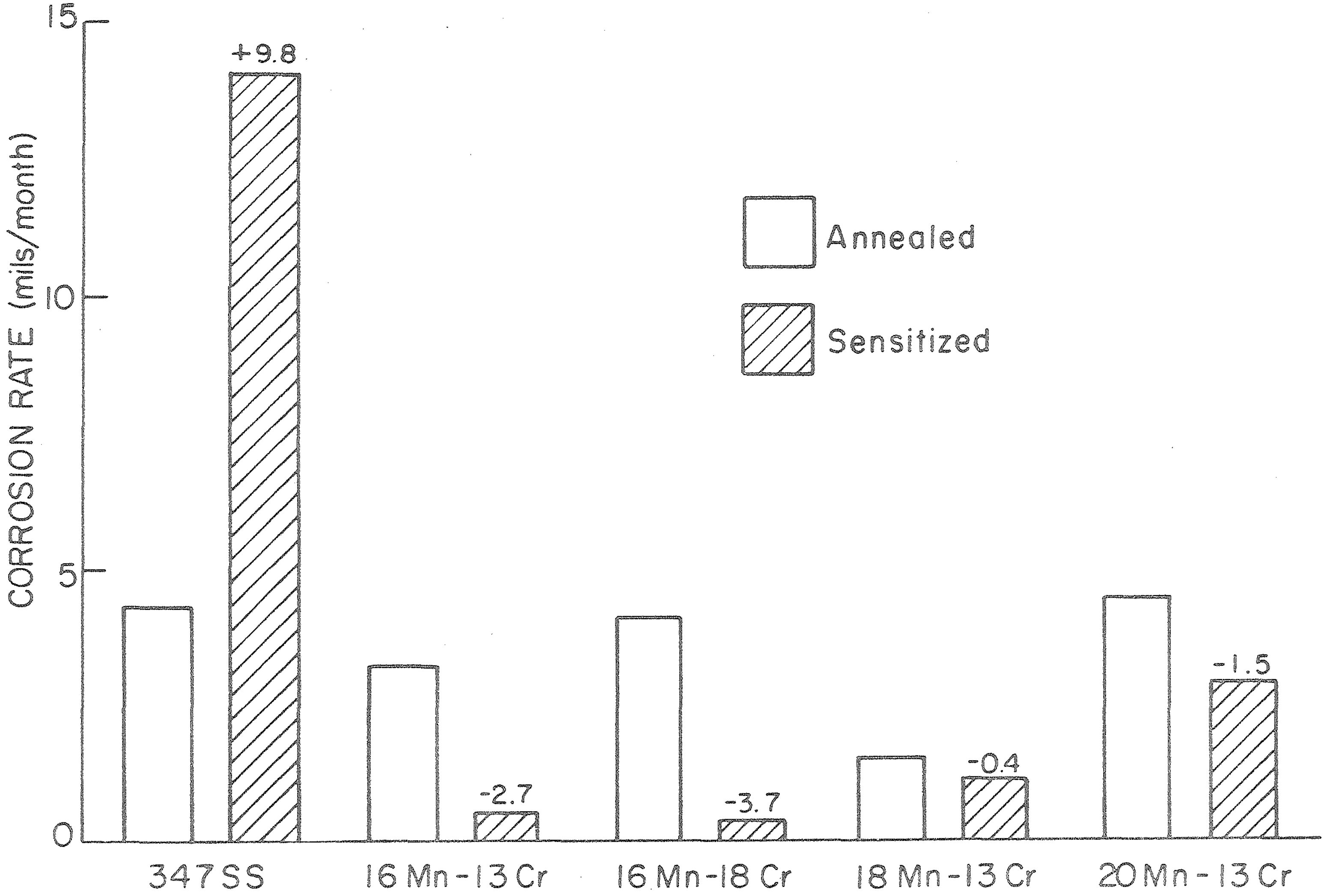

Fig. 62.

XBL 7611-7732